Study of Turbulence and Drag Reduction for Flow Over Backswimmer Textured Surface

Khaled Takrouri

A thesis submitted in partial fulfilment of the requirements of Liverpool
John Moores University for the degree of Doctor of Philosophy

July 2020

Abstract

Great benefits of biomimetic textured surfaces have been recognised through recent research. Such studies highly impact transportation-related fuel consumption and emission of carbon-dioxide. With 10% reduction of friction drag, 4 billion GBP/year savings are expected in the ship industry alone. The shape, spacing and alignment of the textured geometries together with the Reynolds number are the main parameters to characterise turbulent flow and drag performance associated with the use of these surfaces. The present research aims at investigating the effect of a novel biomimetic texture surface on turbulent flow behaviour and drag reduction. The texture is inspired by an aerodynamically-efficient insect called the Backswimmer also known as Notonecta Glauca.

Direct Numerical Simulations (DNS) has been used to examine turbulence and drag reduction for the texture geometry. An in-house code for channel and pipe flows, CHAPSim, is used for the simulations. The code is adopted for (i) treating the novel textured surface using an Immersed Boundary Method (IBM) and (ii) improving the solver scalability by implementing a hybrid parallelisation approach. Verification and validation (where possible) for smooth and textured simulations have been undertaken. The effect of using the backswimmer geometry is studied at different geometry conditions with a constant bulk velocity at Reynolds number Re = 2800. Additionally, the effect of changing the Reynolds number was studied for one geometry condition at Re = 2800, 3500, 5500 and 7400.

Compared to smooth channel, the backswimmer cases showed an increase in the wall-normal and spanwise fluctuating velocities, near wall vorticity and Reynolds shear stress. Among all the backswimmer cases, the increase in the wall normal and spanwise vorticity profiles with the textured element was almost unaffected by either the changes in the geometry or the increase in Reynolds numbers. Compared against smooth channel, the backswimmer geometry case showed a decrease in the ejection events as Reynolds number increases but a significant increase in the sweep events. The flow visualisations and vortex identification were simulated by calculating low- and high-speed streaks and second-largest Eigen value of the symmetric tensor (λ_2). It was shown that the streaky structures and vortex strength within the roughness elements were dependent on the change in the geometry conditions and Reynolds number. As the Reynolds number increased, the intensity of λ_2 increased within the roughness for the smaller Reynolds numbers and above the roughness crest for the higher Reynolds numbers.

Acknowledgement

I would like to take this opportunity to thank everyone who came on board this wonderful research journey. Without you, this work would not have materialized. For that, the least I can say is “Thank You”.

I would like to thank my academic supervisor Dr Mehdi Seddighi for all the academic, professional and personal support. You have been a supervisor, a mentor and a role model. You have introduced me to the world of biomimetics, scientific programming, HPC commissioning and technical support, technical writing, and of course have taught me a lot about CFD and fluid mechanics. On the personal level I have learned a lot from you about dedication to work, passion for innovation, time management and most importantly devotion to research, colleagues and post-graduate researchers.

I would like to thank my second supervisor Dr David Allanson. Throughout this journey I have learned a lot from you about CFD, teaching and working with students (Also thank you for always making sure I am working hard!).

I would like to thank everyone in Liverpool John Moores University (Helen, Natasha, Elizabeth, Laura, Mike, Neil and Neil) and the UK Turbulence consortium for their help and support throughout every stage of the project. Thank you for every simulation I ran. Thank you for giving me the chance to present my work in prestigious conferences which made this research journey even more rewarding.

I would like to thank my family Walid, Sawsan and Yara for their continuous love, motivation and support throughout every stage of this journey. Also, I would like to thank my second family whose support never stopped since day one of this journey my in-laws Fuad, Fatin, Aseel, Haneen, Husam and Shahed.

Last but not least a huge thank you to the one person who motivates, inspires, loves and supports me unconditionally every minute of every day, my wife and best friend Bushra. Thank you for every time you lifted and motivated me, celebrated or thought with me and many times worried about me throughout this four-year journey. For that I was, I am and I will always be grateful. I Love You.

This thesis is dedicated to my Father
Walid Takrouri
No words can describe your endless support

Table of Contents

Nomenclature

Symbols

A, B, C	-	Constants
C_f	-	Friction drag coefficient
DR	-	Drag reduction
h	m	Roughness height
H	-	Shape factor
k_s	m	effective roughness height
L_x	m	Computational domain in the streamwise direction
L_z	m	Computational domain in the spanwise direction
M	-	Number of Roughness elements in the streamwise direction
N	-	Number of Roughness elements in the wall-normal direction
N_l	-	Number of instantaneous flow fields for ensemble-averaging
N_x	-	Number of mesh points in the streamwise direction
N_y	-	Number of mesh points in the wall-normal direction
N_z	-	Number of mesh points in the spanwise direction
p	Pa	Pressure
$\overline{u''v''}_{Q_1}$	-	First quadrant
$\overline{u''v''}_{Q_2}$	-	Second quadrant
$\overline{u''v''_{Q_3}}$	-	Third quadrant
$\overline{u''v''_{Q_4}}$	-	Fourth quadrant
Re	-	Reynolds number based on channel half-height and bulk velocity
Re_p	-	Reynolds number based on channel half-height and centreline velocity of laminar Poiseuille flow

Re_τ	-	Reynolds number based on channel half-height and friction velocity
S	$\frac{1}{s}$	Symmetric part of velocity gradient tensor
U_b	$m.s^{-1}$	Bulk velocity
U_p	$m.s^{-1}$	Centreline velocity of laminar Poiseuille flow.
u_τ	$m.s^{-1}$	Friction velocity
u	$m.s^{-1}$	Streamwise velocity
$\overline{u}$	$m.s^{-1}$	Spatially-averaged streamwise velocity
u'	$m.s^{-1}$	Phase-averaged fluctuating streamwise velocity
u''	$m.s^{-1}$	Spatially-averaged fluctuating streamwise velocity
u''_{rms}	$m.s^{-1}$	RMS of spatially-averaged fluctuating streamwise velocity
v	$m.s^{-1}$	wall-normal velocity
v''	$m.s^{-1}$	Spatially-averaged fluctuating wall-normal velocity
v''_{rms}	$m.s^{-1}$	RMS of spatially-averaged fluctuating wall-normal velocity
w_x	m	Roughness width in the streamwise direction
w_z	m	Roughness width in the spanwise direction
w	$m.s^{-1}$	Spanwise velocity
w''	$m.s^{-1}$	Spatially-averaged fluctuating spanwise velocity
w''_{rms}	$m.s^{-1}$	RMS of spatially-averaged fluctuating spanwise velocity
$\overline{u''v''}$	pa	Spatially-averaged Reynolds shear stress
x	m	Streamwise coordinates
y	m	Wall-normal coordinates
z	m	Spanwise coordinates

Greek

δ	m	Channel half-height
Δx	m	Grid spacing in the streamwise direction
Δy	m	Grid spacing in the wall-normal direction
Δz	m	Grid spacing in the spanwise direction
ϵ	m	Geometry origin shift
κ	-	Von-karman constant
λ_2	-	Second largest eigen value of symmetric tensor $S^2 + \Omega^2$
μ	$Pa.s$	Dynamic viscosity

ν	$\frac{m^2}{s}$	Kinematic viscosity
Π	-	Mean pressure gradient normalised by U_p and δ
ρ	$\frac{kg}{m^3}$	Fluid density
τ	Pa	Wall shear stress
τ_s	Pa	Smooth wall shear stress
τ_r	Pa	Rough wall shear stress
$\omega''_{x\ rms}$	s^{-1}	Spatially-averaged streamwise fluctuating vorticity
$\omega''_{y\ rms}$	s^{-1}	Spatially-averaged wall-normal fluctuating vorticity
$\omega''_{z\ rms}$	s^{-1}	Spatially-averaged spanwise fluctuating vorticity
Ω	$\frac{1}{s}$	Anti-symmetric part of velocity-gradient tensor

Subscripts

$i = 1, 2, 3$	Streamwise, wall-normal, spanwise directions
rms	Root mean square value
b	Bulk value
s	Smooth
r	Rough

Superscripts

$+$	Inner scaling
$*$	Non-dimensional quantity

Abbreviations

CFD	Computational Fluid Dynamics
DNS	Direct Numerical Simulation
LES	Large Eddy Simulation
LIS	Liquid Infused Surface
PIV	Particle-Image Velocimetry
RANS	Reynolds-Averaged Naiver Stokes
SHS	Superhydrophobic Surface

List of Figures

List of Tables

Chapter 1

Introduction

1.1 Background

Drag reduction has been an interesting field of research for a number of years. It is estimated that a 10% drag reduction in friction drag saves 4 billion GBP/year in the ship industry [26]. Drag reduction research applications can range from wind tunnel experiments on flat plate, pipe or channel flows to the study of the total drag reduction techniques on ships and aeroplanes to improve their aerodynamic performance.

Drag reduction can be achieved by introducing foreign substances like polymers, powders and fibres also known as active methods or by mechanically altering flow control surfaces also known as passive methods [27]. The use of textured surfaces inspired by biomimetic surfaces is one of many passive methods used in drag reduction. The effect of using textured surfaces on the drag performance is mainly dependent on the texture geometry, placement and Reynolds number. Although a number of textured surfaces were tested through previous literature, there is no clear relationship between the geometry of the texture used and its corresponding drag performance. When it comes to the study of turbulent drag reduction using textured surfaces there are many questions to answer in this area; for example; What is the flow behaviour in the vicinity of the small-scale textures? How textured surfaces can be modelled accurately using less computationally expensive Computational Fluid Dynamics (CFD) approaches? What is the flow behaviour over textured surfaces at higher Reynolds numbers? Can textured surfaces be combined with other drag reduction methods such as flow unsteadiness, pulsating flow or any of the active methods? The scope of this project is to study the effect of biomimetic surfaces, specifically the Backswimmer insect micro structure on turbulent flow behaviour and drag performance at various topologies and Reynolds numbers.

1.2 Aims and Objectives

The present research aims at investigating the effect of a novel biomimetic texture surface on turbulent flow behaviour and drag reduction. The texture is inspired by an aerodynamically-efficient insect called the Backswimmer also known as Notonecta Glauca. Direct Numerical Simulations (DNS) as the-state-of-the-art CFD approach is used for this study.
The followings are specific objectives of the work presented in this thesis:

- To implement the novel texture in the code and perform modernisation for parts of the solver and post-processing codes.
- To investigate turbulent behaviour using textured surface to understand the effect of changing the number of roughness elements in the streamwise and spanwise directions at Reynolds number $Re = 2800$.
- To investigate the effect of the change in Reynolds number on the turbulent flow behaviour over the backswimmer textured surface.

1.3 Thesis Outline

The present thesis consists of seven chapters. Chapter 2 presents a literature review of the previous relevant studies investigating drag reduction, flow control and turbulence structure. Chapter 3 presents the numerical approaches used for the presented work. The chapter discusses the DNS code used for the investigations. Also, the main parallelisation and code optimisation methods are described in this section. Chapter 4 discusses the Immersed Boundary Method (IBM), as the main approach to treat roughness elements. Also, presented in this chapter, is the implementation of the texture in the code and the associated challenges. Chapter 5 presents a detailed analysis to understand the effect of increasing the number of textured elements in the streamwise and spanwise directions at $Re = 2800$. The analysis is in terms of turbulence statistics and flow visualisations. Chapter 6 studies the turbulence structure and drag performance for the backswimmer geometry at different Reynolds numbers and compares it against smooth channel flow over a range of Reynolds numbers $Re = 2800 - 7400$. Finally, chapter 7 presents the conclusions from the generated results presented in the previous chapters in addition to future suggestions and chances of improvements.

Chapter 2

Literature Review

This chapter is dedicated to presenting previous literature where biomimetic surfaces turbulence and drag reduction were investigated. The presented literature is in two categories: a biology aspect, where the biomimetic surfaces were studied experimentally or by observation of the animals in their natural habitat. Another approach is from an engineering perspective, where the geometries are studied analytically for laminar flow cases, experimentally by testing the textured surfaces in wind tunnels or numerically using CFD.
Previously studied geometries in terms of shape are categorized as follows: superhydrophobic surfaces (SHS), 3D geometrical riblets and posts including: square, triangular, pyramid, circular and biomimetic inspired textured surfaces like the herringbone feather texture and shark denticles .
In terms of drag performance, the presented literature is divided in two categories: i) turbulent drag reduction using biomimetic textured surfaces and ii) turbulent drag increase using biomimetic textured surfaces.

2.1 Turbulent Drag Reduction Using Biomimetic Textured Surfaces.

The aerodynamic drag on a body is defined as the total of pressure drag and skin friction drag. The pressure drag known as form drag is caused by the regions of flow separation. The skin friction drag is caused by the friction of

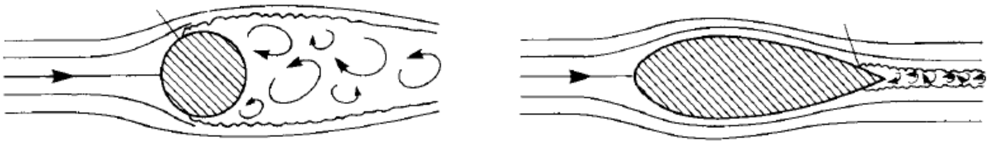

(a) Blunt Bodies (b) Streamlined bodies

Figure 2.1: Aerodynamic bodies classification based on the major contribution of the drag component (a) Blunt body and (b) Streamlined body [1].

the object against the fluid while moving through it [1]. The contribution of each drag component towards the total drag is useful in analysing different aerodynamic phenomena. Thus, aerodynamic bodies can be divided into two generic categories in terms of the major drag contributor towards the total drag: blunt bodies shown in Figure 2.1(a); where the major contribution into the total drag is from pressure drag, and streamlined bodies shown in Figure 2.1(b) where skin friction drag plays the major contribution into the total drag.

Drag reduction using biomimetic surfaces has been an interesting field of research for the past few years. The energy crisis in the 1970s was one of the key motivations to develop drag reduction techniques for all types of land, sea and air transportation. The aim was to develop, understand and implement alternative drag reduction methods inspired by nature. Early drag reduction studies were suggested by Avians and Nekton [24], inspired by fliers and swimmers in nature. They assumed that nature creatures have developed drag reduction adaptations to improve both their efficiency and speed. Such studies were trying to answer three main questions: How to understand such adaptations to improve and optimise them for practical applications? Where do human derived technologies occur in the natural world? And how can we understand the animals' forms and functions? [24]. The outcome of the historically studied turbulent drag reduction techniques using Biomimetic surfaces can be described in three categories: (i) techniques which the effect of using a biomimetic inspired method proved to work in an industrial application, (ii) techniques which preliminary data exists but is not yet applied to an industrial application and (iii) techniques which previous

Table 2.1: The use of biomimetic surfaces among literature as categorized by Bushnell and Moore [24].

Category	Example
Biomimetic texture implemented in the industry.	Dragonfly [2], triangle riblets [3], Shark skin [4].
Biomimetic texture with preliminary data showing drag reduction.	k- and d- type Roughness [15], Superhydrophobic surfaces [7], Liquid infused surfaces [8].
Biomimetic texture with observations and recommendation.	Backswimmer [12], Penguin [28], Bell spiders [29].

literature suggests there is potentially an effective drag reducing technique based on previous observations or experimental analysis but yet still needs to be further studied and investigated [24]. Examples of these three categories are shown in Table 2.1.

The earliest efforts to study biomimetic textured surfaces include: owl leading edge comb by Hertel [30] in 1963 as a natural vortex generator, leaf or branch deformation to exploit favourable interference by Meroney [31] in 1968, the studies by Newman et al [32] in 1977 for dragonfly wings to control flow separation, fish gills by Magnuson [33] in 1978 to enhance turbulence function near maximum girth. A detailed description of the history of the previous biomimetic efforts is summarised and explained by Bushnell and Moore [24].

2.1.1 Biomimetic Surfaces in the Industry.

A number of biomimetic surfaces have been used in industrial applications. The main geometries to appear in these applications are: (i) zigzag wing structure inspired by the dragonfly, (ii) riblets with different geometrical shapes and (iii) shark skin inspired structures.

Dragonflies can fly long distances with minimal energy consumption. Additionally, they are capable of performing complex manoeuvres like rapid acceleration, sharp turning, hovering and gliding. Such characteristics are due to the complex structure of their wings. The main characteristics for the dragonflies are the zigzag structure on the edge of the dragonfly wing and

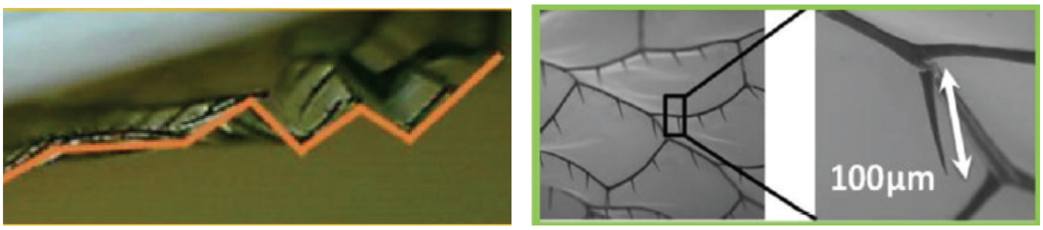

(a) Zigzag dragonfly (b) Dragonfly pin

Figure 2.2: Dragonfly drag reducing textures (a) Zigzag dragon fly and (b) Dragonfly pin-veins by Zhang et al [2].

the pin structure present on the dragonfly's veins shown in Figure 2.2 [2]. Zhang et al. [2] tested the drag reduction inspired zigzag wing-pillar and a zigzag wing only and compared it against conventional flat wings for the case of gliding flight. The tests were constructed at a range of Reynolds number between $Re = 1000$ and 3000. The corresponding drag reduction compared to the flat wing varied between 13% for the zigzag wing and 27% for the zigzag-pillar configuration.

Although riblets are not directly inspired by nature, there has been a number of industrial applications where the use of these textured surfaces improved the drag performance. Viswanath [3] reviewed the effect of using riblets (shown in Figure 2.3) on aircraft viscous drag for 2D airfoils, 3D swept wings and wing body configurations experimentally over a wide range of Mach numbers $M = 0.3 - 0.8$. For the case of 2D airfoils the skin friction drag reduction was between 5-8%. For the case of the wing-body configuration the total drag reduction was about 2-3%. In addition to the drag performance, Viswanath [3] included spatially averaged statistics; velocity profiles, friction velocity, Reynolds shear stress profiles and quadrant analysis for use of riblets on NACA0012 2D airfoil.

Riblets structure are also used to manufacture drag reducing paints to enhance the fuel consumption for the aviation and shipping industries by Stenzel et al. [34]. The measurements were carried out on a torpedo-shaped model and tested experimentally where the riblet spacing was 50 μm, height 25 μm in a 10 m/s water flow. The drag reduction obtained from the riblet tex-

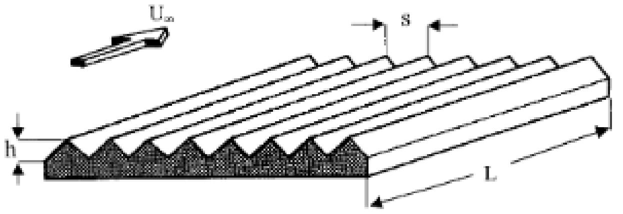

Figure 2.3: Triangular riblets used for aircraft wings drag reduction by Viswanath [3]

tured coating was compared against a smooth coating. The obtained drag reduction tested for torpedo shaped specimens was 5.2%. The paint was also tested on a wing section with 1.55 m span, 0.7 m chord length with a riblet spacing of 150 μm, height 25 μm and Reynolds number $Re = 1.6 \times 10^6$. The achieved drag reduction for the wing section was equal to 6.2%
The shark skin structure was mimicked to improve the swimming speed through the Speedo Fastskin swimsuit to enhance swimmers' drag performance. The textured swimsuit improved the efficiency of the locomotion [35]. The Speedo Fastskin swimsuit was tested by Toussaint et al. [4] and compared against conventional swimsuits shown in Figure 2.4 by 13 swimmers at velocities between $1.0 - 2.0$ $m.s^{-1}$. Although the claimed drag reduction by Speedo was 7.5%, the experimentally achieved drag reduction was equal to 2.5% which translates to 1.2 seconds quicker for a 100 meter race which provides a large competitive advantage.

2.1.2 Biomimetic Surfaces in Research

A wide number of textured geometries were studied and examined through out literature. Most of the studies in this category were for channel or pipe flows. This category was studied not only to analyse the drag performance but to understand the turbulent behaviour through turbulence statistics and detailed flow structures. Also, this category of biomimetic textures worked on answering a number of questions like: How do the texture geometries affect the drag performance and the turbulence statistics? What is the effect of changing the alignment, spacing, orientation and height of the textures

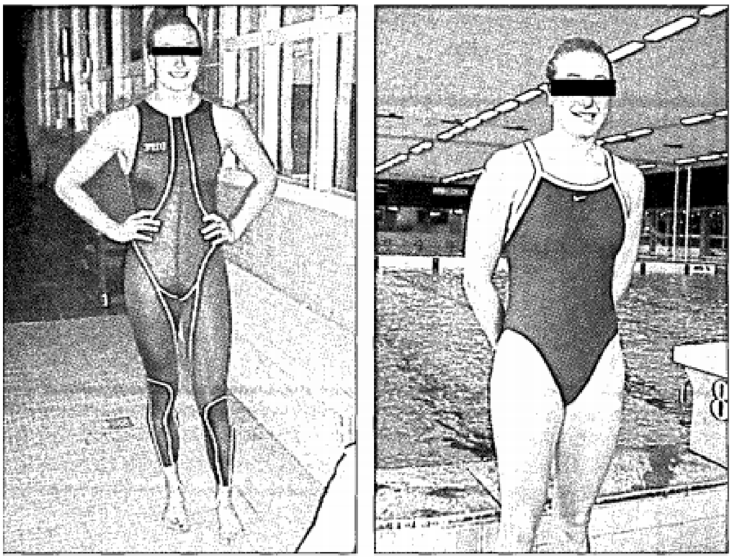

Figure 2.4: Fastskin swimsuit inspired by shark geometry (left) compared to conventional swimsuit (right) by Toussaint et al. [4].

across the channel or the pipe? And how does the change in Reynolds number affect the turbulence structures and drag reduction for textured surfaces? It is also worth mentioning that the studies under this category were viewed from an engineering point of view, unlike the last category where the studies are mainly viewed from a biological point of view.

2.1.2.1 Superhydrophobic Surfaces

Superhydrophobic surfaces are inspired by the leaves of the lotus plant known for their exceptional water repellency features. The repellency features are achieved by trapping pockets of air within the pores of the outer surface of the organisms. The entrapped air can cause friction drag reduction for turbulent flows [36]. Numerically, the implementation of SHS is done using slip/no-slip boundary condition which defines the SHS along the channel wall in the streamwise and spanwise directions only. The magnitude of the slip velocity is proportional to the magnitude of the shear rate due to the fluid flow. The region of the slip is quantified using the slip length factor [37]. Recently, SHS are also being modelled as 3D geometry using the Immersed Boundary Method (IBM) which takes into account the changes in the roughness height. The method is capable of treating complex geometries at minimal computational cost.

Martell et al. [7] investigated drag reduction over superhydrophobic surfaces for turbulent channel flow at low friction Reynolds number $Re_\tau = \frac{u_\tau \delta}{\nu} = 180$ using Direct Numerical Simulations (DNS) and obtained a maximum wall shear stress reduction of 40%. The SHS was defined using the slip/no-slip boundary. The improvement in the drag performance was inversely proportional to the spacing between the SHS elements.

Martell et al. [7] quantified the change in drag by means of turbulence statistics, compared it to smooth channel case and summarized the effect of SHS for the case of drag reduction in terms of spatially averaged streamwise velocity, fluctuating velocities and Reynolds shear stress profiles as follows,

- Spatially averaged velocity: for the case of drag reduction, the value of the velocity profile exhibited an increase compared to smooth channel flow.
- Fluctuating velocities: for the case of drag reduction, the fluctuating velocities in the streamwise, wall-normal and spanwise directions exhibited a decrease in the profile compared to smooth channel flow.
- Reynolds shear stress: A dip in the shear stress profile in the negative direction was observed for the case of drag reduction, unlike smooth channel flow where the profile values were positive.

As a follow up work, Martell et al. [38] studied the effect of superhydrophobic surfaces on drag performance at three different friction Reynolds numbers $Re_\tau = 180, 395$ and 590 for turbulent flows. The maximum drag reduction was 50%. The spacing between the SHS elements was still the major parameter affecting the drag performance at all Reynolds numbers.

In addition to the change in the Reynolds number, the alignment of the SHS elements with the mean flow direction or transverse to flow direction were examined. The transverse alignment exhibited a behaviour similar to smooth channel flow.

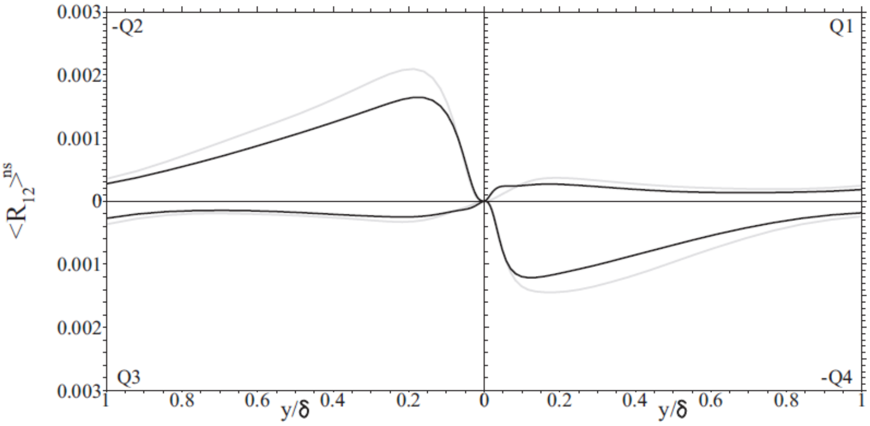

Figure 2.5: Quadrant analysis by Jelly et al. [5] for SHS (—) and smooth (—) cases. R_{12} denotes Reynolds shear stress averaged across no-slip phases.

Jelly et al. [5] took the analysis by Martell et al. [7] [38] one step further to better understand the flow around superhydrophobic surfaces for streamline aligned superhydrophobic surfaces. The overall drag reduction was reduced by 21.6%. The purpose of the analysis was to study the change in the turbulent budget terms, Reynolds shear stress detailed contour plots, quadrant analysis and comparing it with those from smooth channel flow. The quadrant analysis showed a suppression in the second and the fourth quadrant which represent the ejection and sweep motions, the amount of reduction was 23% and 17% for Q2 and Q4 respectively. It was also noticed that Q2 and Q4 profiles exhibited a shift towards the SHS wall for the case of drag reducing flows as shown in Figure 2.5. Jelly et al. [5] also studied the vortex identification for smooth and SHS surfaces using the second largest Eigen value of symmetric tensor λ_2 criterion proposed by Jeong and Hussain [6] and noticed that for the case of the drag reduction, the intensity of λ_2 significantly decreased compared to smooth channel flow as shown in Figure 2.6.

The alignment of SHS texture elements and its effect on drag reduction compared to the longitudinal configuration and smooth channel flow was examined by Wantabe et al. [39]. They studied the effect of changing the SHS angle to the flow on drag reduction. DNS simulations at $Re_\tau = 180$ were used at constant pressure gradient while maintaining constant width for the SHS elements. The drag reduction was inversely proportional to the change in

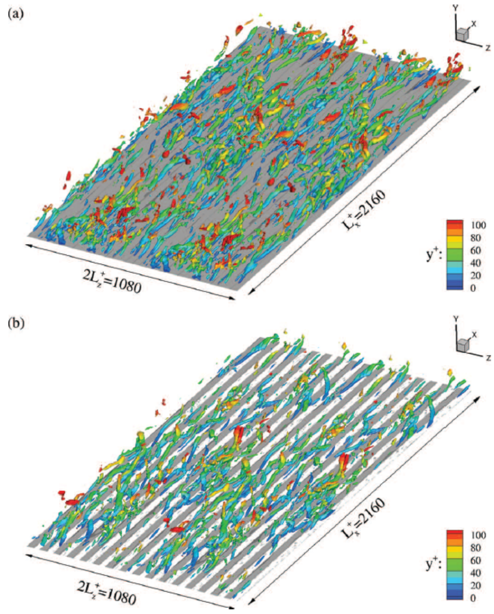

Figure 2.6: 3D iso-surface for λ_2 distribution along (a) smooth and (b) SHS by Jelly et al. [6] coloured by the value of the wall-normal distance away from the channel wall.

angle compared to the parallel configuration, for a micro-ridge angle equal to zero the increase in the bulk mean velocity was about 15%. when the micro-ridge angle reached 90 degrees the increase in bulk velocity was about 5% . The effect of the different micro-ridge angles was clearly visible for the case of the spatially averaged velocity profile and fluctuating velocities. However, for the case of the Reynolds shear stress the effect of changing micro-ridge angles was negligible compared to the parallel configuration.

Alame and Mahesh [40] studied the flow over 3D roughness elements using IBM they called it a “realistically rough” superhydrophobic surface for laminar Couette flow for friction Reynolds number $Re_\tau = 180$. The roughness effect was up to 40% of the channel height in the wall-normal direction. It was found that the DR is mainly dependent on two components: the slip velocity and the turbulent losses due to the Reynolds shear stress contribution. The 3D implementation allowed Alame and Mahesh [40] to change the interface region from fully wetted to fully covered by changing the roughness height and found significant changes in the fluctuating velocities profile due to the presence of trapped air in the textured elements cavity.

Areans et al. [8] also compared superhydrophobic surfaces, against 3D implemented geometries by means of liquid infused surfaces (LIS) inspired by the Nepenthes pitcher plant shown in Figure 2.7. LIS surfaces are composed of functionalised surface textures wetted with chemical lubricant which results in heterogeneous fluid-liquid and fluid-fluid interfaces. SHS are composed from hydrophobic textures which locally stabilizes pockets of air when submerged under water resulting in an air-water and solid-water interface [8].

To replicate superhydrophobic surfaces, large viscosity ratio equal to 100 was used and the resulting profiles were compared against the free-slip boundary conditions. The comparison was in terms of the drag performance, spatially averaged velocity profiles and fluctuating velocities profiles. The geometries used throughout the study were: longitudinal square streamwise bars, transverse square bars and staggered cubes. The velocity profiles were similar for both implementations, however, the profiles for the case of the SHS free-slip boundary case were larger than the high viscosity ratio case where IBM was used for the case of the transverse and longitudinal bars.

Areans et al [8] concluded that whether it's a case of drag reduction or drag increase, the structure of the near wall turbulence is dominated by the total shear and not by the local boundary condition used, whether it is a superhydrophobic surface simulated using the no-slip boundary or using a 3D geometrical rough surface. Although for this particular case the no-slip method did not have major differences compared to the IBM method, the use of 3D implemented geometries gave a great opportunity to study the turbulent behaviour and the drag reduction of a vast majority of geometrical textured surfaces. Examples of such geometries include the use of triangle, pyramid, square, circular, and the presented work of the backswimmer texture as well.

2.1.2.2 3D Geometries, Riblets and Biomimetic Surfaces.

Sassun et al. [9] studied 3D geometries shown in Figure 2.8 using DNS and compared its drag performance for channel and pipe flows. The geometries include: square riblets (longitudinal and transverse), triangular riblets (lon-

(a) Lotus leaf (SHS)

(b) Nepenthes Pitcher plant (LIS)

Figure 2.7: Superhydrophobic surfaces [7], [5] inspired by (a) Lotus leaf and liquid infused surfaces inspired by (b) Nepenthes Pitcher plant in nature [8].

gitudinal and transverse) and scattered cubes for friction Reynolds numbers $Re_\tau = 180 - 360$ using IBM. All the geometries were compared against a reference smooth channel and pipe flows at $Re_\tau = 204$ and $Re_\tau = 169$, respectively. The most drag reduction was found for the case of longitudinal triangular bars where $Re_\tau = 157$ with a $DR = 23.0\%$ for channel flows and pipe flows as well with $Re_\tau = 162$ with $DR = 4.1\%$ drag reduction. The authors noticed that the drag performance of longitudinal bars is significantly better than the same geometries with transverse bars.

Goldstein et al. [41] studied the drag performance and modelled the turbulent flow over triangle riblets. The obtained drag reduction was equal to 4%. Simulations were performed for small, medium, and large riblets. The largest amount of drag reduction was obtained in the case of relatively large blunt elements. Compared to SHS and the square riblets, the triangle riblets exhibited different statistics specially for the cases of drag reduction. The differences were mainly in terms of the streamwise fluctuating velocity and the Reynolds shear stress profile. Although drag reduction was obtained, there was an increase in both of these profiles. Also, the peak of the profiles was shifted away from the channel lower wall.

Itoh et al. [10] studied the seal fur inspired surface shown in Figure 2.9 drag reduction experimentally using Laser Doppler Velocimetry (LDV). A maximum drag reduction of $DR = 12\%$ was obtained which was claimed to

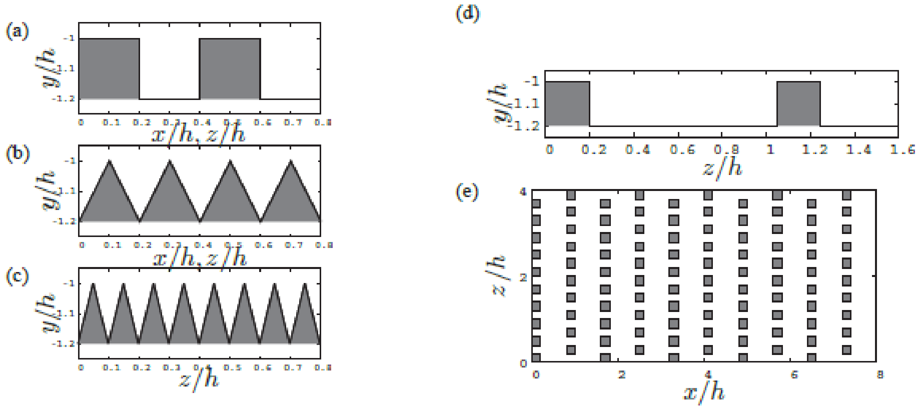

(a) (a) Square bars longitudinal(SL) (b) Triangular bars longitudinal (TL) or transverse (TT) (c) Longitudinal triangular bars(TLS) (d) Longitudinal square bars(SLL), (e) Staggered cubes (SC)

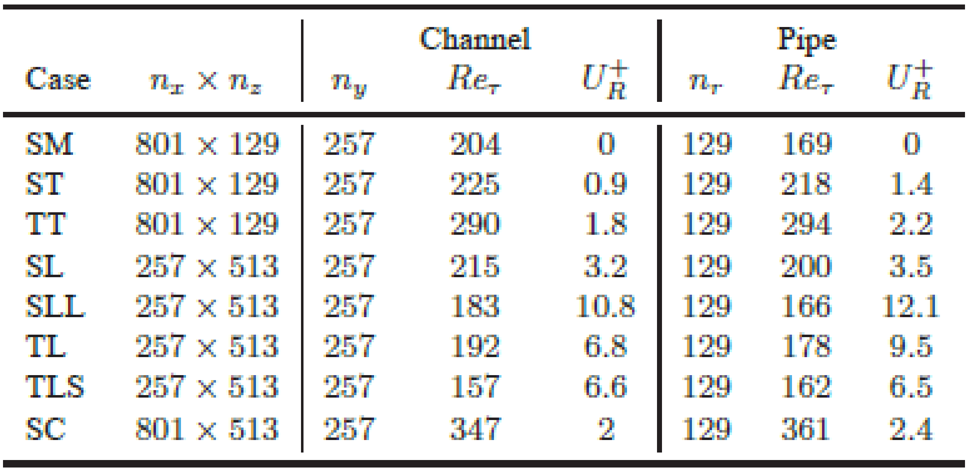

Case	$n_x \times n_z$	Channel n_y	Channel Re_τ	Channel U_R^+	Pipe n_r	Pipe Re_τ	Pipe U_R^+
SM	801 × 129	257	204	0	129	169	0
ST	801 × 129	257	225	0.9	129	218	1.4
TT	801 × 129	257	290	1.8	129	294	2.2
SL	257 × 513	257	215	3.2	129	200	3.5
SLL	257 × 513	257	183	10.8	129	166	12.1
TL	257 × 513	257	192	6.8	129	178	9.5
TLS	257 × 513	257	157	6.6	129	162	6.5
SC	801 × 513	257	347	2	129	361	2.4

(b) Computational grids for channel ($n_x \times n_z$) and pipe (n_r), friction Reynolds numbers Re_τ and slip velocities.

Figure 2.8: Sassun et al. [9] 3D geometries and their corresponding mesh parameters, friction Reynolds numbers and slip velocities.

be higher than the one for riblets. Also, it was reported that for the case of seal fur the drag increase due to the effect of the roughness surface was not present even at the highest Reynolds numbers tested in this study. Compared against riblet surface, one of the reasons behind the obtained drag reduction being higher than the riblet case was the non-uniform geometry structure unlike uniformly shaped riblets. The drag reduction was quantified using

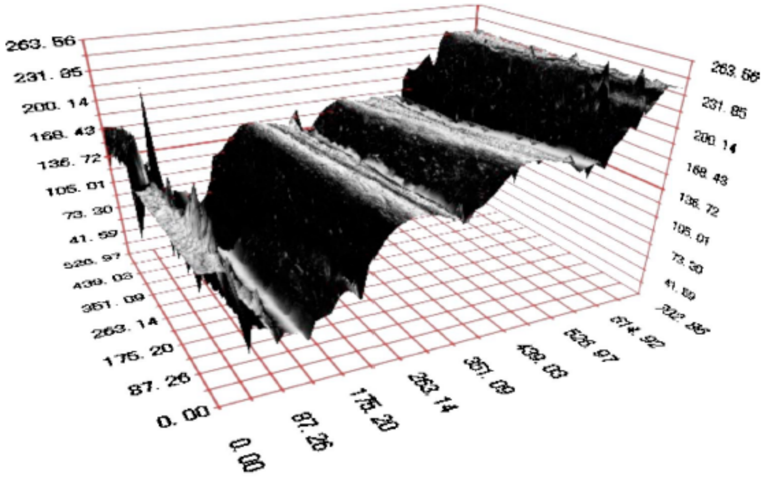

Figure 2.9: Seal fur inspired drag reducing surface by Itoh et al. [10].

both spatially averaged velocity profiles and fluctuating velocity profiles. An overshoot was obtained for the case of the spatially averaged profiles where a decrease in the streamwise fluctuating velocity was obtained compared against smooth channel flow.

2.1.3 Potential Drag Reducing Surfaces from a Biological Perspective.

The third category for drag reducing surfaces is potential drag reducing surfaces from a biological point of view. These textured surfaces were studied by biologists to understand animal behaviour or as a potentially drag reducing surface. However, there has been no numerical or experimental data to prove the texture reliability in an industrial context.

Diez et al. [11] studied the effect of denticles across shark bodies on drag for Mako shark. The morphology, density and orientation of the denticles for 49 different texture patterns (shown in Figure 2.10) for a shark in sea water enclosure at Reynolds number $Re = 3.42 \times 10^6$ and shark length of 1.33 m. The aerodynamic performance in terms of the lift, drag, skin friction drag coefficients and time-averaged velocity flow fields showed that the height increase of the denticles $h = 500\mu m$ had a negative effect on the drag

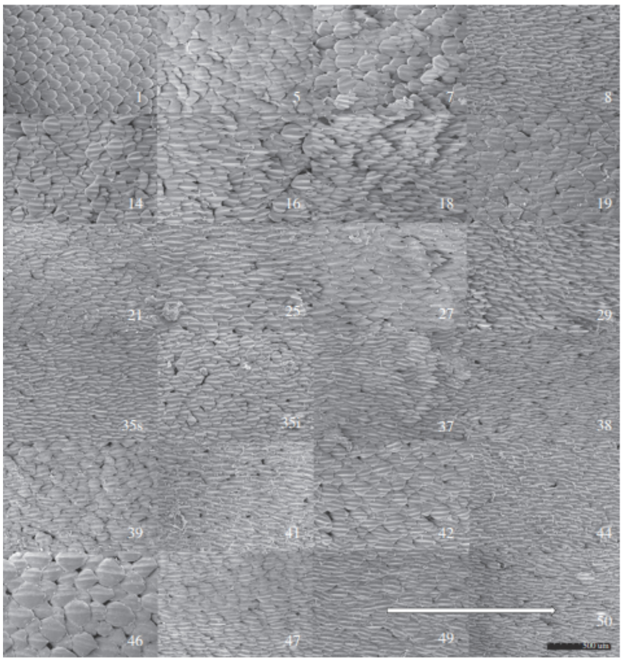

Figure 2.10: Shark denticles patterns across a Mako shark body investigated by Diez et al. [11] .

performance compared to the $h = 250\mu m$ case. Additionally, the pectoral fins area (along the shark body) exhibited maximum values of skin friction drag.

The Backswimmer insect shown in Figure 2.11 also known as Notonecta glauca can dive and swim quickly through water [12]. The Backswimmer is capable of supporting itself under water using its forelegs and the tip of its abdomen. From a biological point of view, air layers found on the wings of the backswimmer are considered a biological role model for biomimetic fluid drag reduction using its double structure of hairs and microvilli (the implemented geometry) responsible for air retention and other sensory functions. Ditsche et al. [12] studied the air retaining properties for the backswimmer and demonstrated outstanding film persistence under hydrostatic and hydrodynamic conditions. The backswimmer hairs and microvilli structure were able to hold an air film for long periods (up to 130 days) and flow velocities up to 5 m/s.

More recently Mail et al. [22] proposed a bio-inspired method for pressure

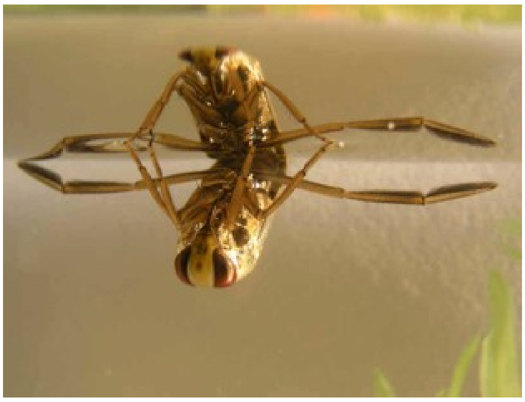

Figure 2.11: The Backswimmer insect studied in Ditsche et al. [12]

sensing based on the underwater retaining properties of the Backswimmer. This made the Backswimmer structure an interesting biomimetic model for drag reduction in the ship industry.

The present study examines turbulent drag reduction for a novel texture geometry implementation inspired by the Backswimmer. Examples of other biomimetic surfaces inspired by nature studied from a biological point of view include: the study of drag reduction inspired by jumping emperor penguins using bubble clouds by Davenport et al. [28], bell spiders [29], water strider [42], geese and ducks feathers [43].

2.2 Turbulent Drag Increase Using Biomimetic Textured Surfaces.

Boomsma and Sotiropoulos [13] used DNS to study turbulent flow and the drag performance over 3D implementation of shark denticles which they named “realistic denticles”. The simulations were performed at $Re_\tau = 180$ and the geometry was implemented using IBM. The flow was characterised based on the spacing between the keels in wall units s^+ as shown in Figure 2.12 and the tests were performed for $s^+ = 13-15$ aligned and staggered. Compared against riblets which exhibited 5% drag reduction under the same conditions, all the tested shark skin denticles resulted in an up to 50% drag

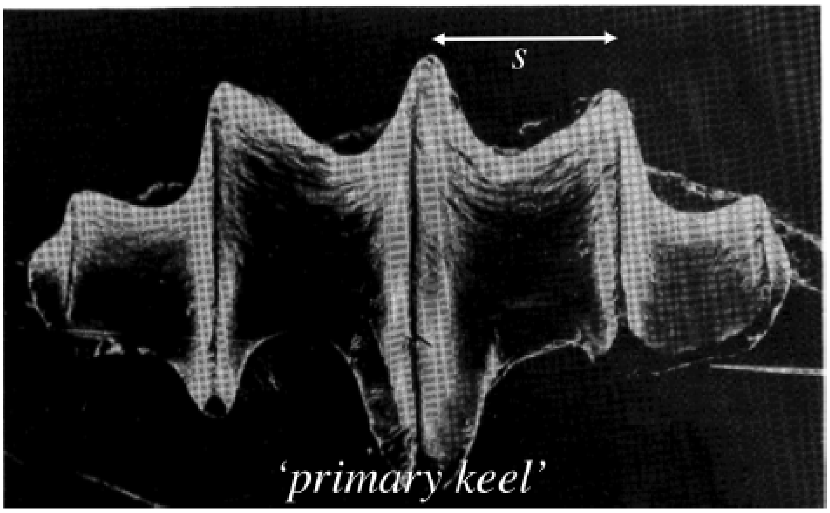

Figure 2.12: 3D shark keels texture where s^+ is the spacing parameter investigated by Boomsma and Sotiropoulos [13].

increase. 25% of the total drag increase was form drag. The increase in drag was due to 3D complex shape of the denticles which resulted in an increase in the flow dominated by strong secondary flow.

The Herringbone feather inspired texture shown in Figure 2.13 was studied using DNS by Benschop and Breugem [14] at $Re_\tau = 180$ after 16% drag reduction was achieved by Chen et al [44] [45] experimentally.

The texture consisted of blade riblets in converging/ diverging herringbone pattern. Although the herringbone structure is inspired by an aerodynamically-efficient natural creature, the drag performance compared against smooth channel flow resulted in a drag increase of up to 73%. This was due to the strong secondary flow which formed above the riblets. The conclusion of the study suggested that converging /diverging riblets are not capable of reducing drag. However, it was found that one way to improve the geometry is by increasing the feather width, which reduces the amount of the texture subjected to the secondary flow as the texture behaves similar to the conventional parallel riblets configuration.

Although birds are aerodynamically-efficient creatures and probably the idea of flying was inspired by their form of locomotion in nature, yet, this is an example of the industrial implementation of a natural drag reduction method

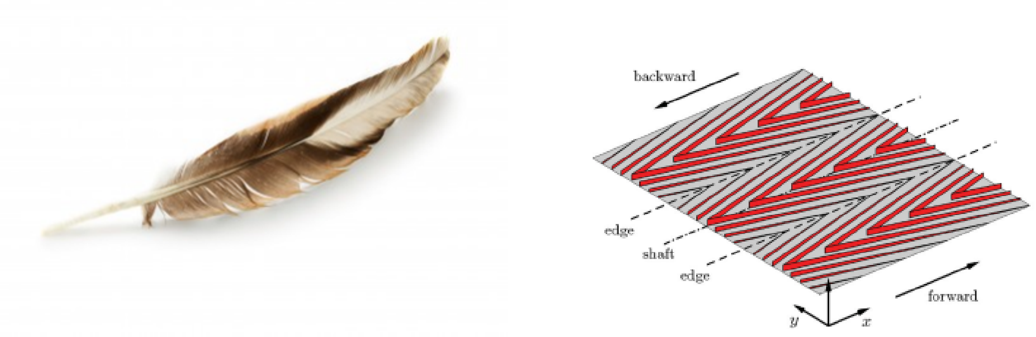

(a) Herringbone bird feather

(b) Herringbone bird 3D riblet

Figure 2.13: Herringbone bird feather (a) in nature and (b) numerical 3D implemented riblets by Benschop and Breugem [14].

which can lead to either no drag reduction or significant drag increase.

Sassun et al.'s [9] DNS database mentioned earlier (shown in Figure 2.8) included a wide range of examples where the use of textured surfaces resulted in no change of drag or even a significant drag increase. About 63% of the studied test cases resulted in drag increase compared against smooth channel and pipe flows. The drag increase was recorded for transverse elements and staggered cube cases. The highest drag increase was found for the scattered cubes pipe flow where $DR = -113\%$ and for channel flows at $DR\% = -70\%$. Overall, it was found that the drag reduction over channel flows was more effective than over pipe flows. The drag reduction for more geometries is shown in Table 2.2 in addition to the simulation parameters for the DNS works shown in Table 2.3.

Table 2.2: Literature review summary including the method of study, Re_τ, texture shape and drag reduction where EXP denotes experimental studies.

Author	Method	Re_τ	Texture	DR%
Zhang et al. [2]	EXP	[-]	Zigzag dragonfly	13%
Zhang et al. [2]	EXP	[-]	Zigzag pillar dragonfly	27%
Viswanath [3]	EXP	[-]	Triangle riblets	2 - 8%
Stenzel et al. [34]	EXP	[-]	Shark skin riblets (torpedo)	5.2%
Stenzel et al. [34]	EXP	[-]	Shark skin rilblets (wing)	6.2%
Speedo [35]	[-]	[-]	Fastskin swim suit	7.5%
Toussaint et al [4]	EXP	[-]	Shark skin	2.5%
Martell et al. [7]	DNS	180	SHS square	40%
Martell et al. [38]	DNS	180 395 590	SHS square	$> 50\%$
Ibrahim et al. [46]	RANS	$3\,x\,10^6$	Shark skin	4%
Jelly et al. [5]	DNS	180	SHS riblets	21.6%
Watanabe [39]	DNS	180	Oblique SHS	15%
Alame [40]	DNS	[-]	3D SHS	$5{-}35\%$
Arenas et al. [8]	DNS	180	Longitudinal square LIS	4%
Arenas et al. [8]	DNS	180	Staggered cubes LIS	15%
Sassun et al. [9]	DNS	205	Triangle bars (longitudinal)	23%
Sassun et al. [9]	DNS	290	Triangle bars (transverse)	-42.1%
Sassun et al. [9]	DNS	215	Square bars (longitudinal)	-5.4%
Sassun et al. [9]	DNS	225	Square bars (transverse)	-10.3%
Benschop [14]	DNS	175	Herringbone feather	9.3%
Benschop [14]	DNS	587	Herringbone feather	-73%
Chen [44]	EXP	[-]	Herringbone feather	16%
Chen [45]	EXP	[-]	Herringbone feather riblet	20%
Goldstein et al. [41]	DNS	180	Triangle riblets	4%
Boomsma [13]	DNS	180	Shark denticles	-55%
Itoh et al. [10]	EXP	180	Seal fur	12%

Table 2.3: Literature review summary for cases in Table 2.2 where DNS was used. N_x, N_y, N_z are the number of mesh points in the streamwise, wall-normal and spanwise directions. w_x^+, w_z^+ are the elements width in the streamwise and spanwise direction (w_z^+ = [-] is for riblets) and h^+ is the roughness height. BM denotes boundary method, CSM represents cartesian scattered mesh, FDM is finite difference method and FVM denotes finite volume method.

Author	Numerical Method	BM	$N_x \times N_y \times N_z$	w_x^+	w_z^+	$h^{+‘}$
[7]	CSM	Slip	$128 \times 128 \times 128$	$30\mu m$	$30 - 90\mu m$	0
			$256 \times 256 \times 256$			
[38]	CSM	Slip	$128 \times 128 \times 128$	37.031	37.031	0
			$256 \times 256 \times 256$	74.062	74.062	
			$512 \times 512 \times 512$	37.031	111.09	
[5]	CSM	Slip	$512 \times 128 \times 1024$	$30\mu m$	$30\mu m$	0
[39]	FDM	Slip	$128 \times 128 \times 128$	33.75	33.75	0
[40]	FVM	IBM	$448 \times 256 \times 271$	[-]	[-]	3.6
[8]	FDM	IBM	$1280 \times 384 \times 512$	5.4	[-]	5.4
			$512 \times 384 \times 1280$			
[9]	FDM	IBM	$801 \times 256 \times 129$	18,36	[-]	36
			$257 \times 257 \times 513$			
[14]	FVM	IBM	$400 \times 1024 \times 320$	17	[-]	8.5
[41]	Spectral	IBM	$[-] \times$ 32–256 $\times$ 6–80	18	[-]	5.3
				11.7		9.4
[13]	FDM	IBM	$190 \times 150 \times 166$	16	16	8
			$723 \times 123 \times 1466$			
			$1157 \times 104 \times 161$			

2.3 Textured Surfaces Turbulence Modelling.

Turbulent flows over rough surfaces have been studied since 1854 by Hagen [15], who was interested in pressure losses in water conduits defined as pipes or tubes where fluids, cables or electric wires are contained, conveyed or protected. The two main roughness geometries that have been widely investigated through previous literature are the k- and the d- type roughness elements shown in Figure 2.14. The main difference between the two configurations is the value of the effective roughness. Jimenez [15] presented a brief explanation on the history of turbulent flows over rough walls. The author concluded that the effect of rough walls on turbulent boundary layer is mainly dependent on Reynolds number, the equivalent to roughness height by Nikuradse [23] sand grain and the roughness function. Also, it was found that for transitionally rough regime where $k_s^+ < 50$, the extent of the roughness interference with the buffer layer is highly variable especially for uniform geometries as well as drag reducing riblets, and further investigating for the transitionally rough regime was recommended. The author also reviewed theoretical models used to analyse different types of geometries and the basic turbulence quantities where turbulent flow research looks at the implementation of any novel geometry whether experimental or numerical including: spatially averaged velocity profiles, logarithmic velocity distribution adaptations for textured surfaces, wake intensities specially for the d-type roughness and fluctuating velocities and their behaviour as the roughness height increases .

Orlandi et al. [47] studied the effect of the consecutive separation of the roughness elements and their placement along the flow direction or orthogonally. The tested geometries include circular, triangular textured surfaces at two different width to height ratios $w/k = 0, 1$ and square elements placed on the lower channel wall. It was noticed that for the case of the triangle roughness elements, the effect of reducing the width-to-height ratio was more significant than in the case of longitudinal square. In terms of fluctuating velocities, the effect of number of elements is more significant than the spatially averaged velocity profiles. For both alignments, the increase of the

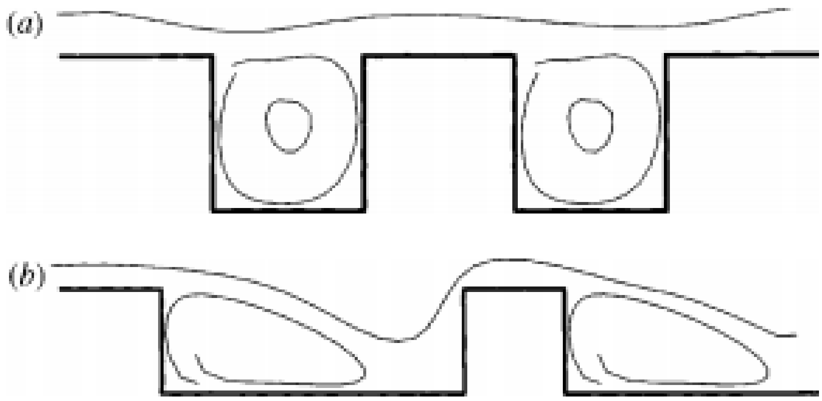

Figure 2.14: Square geometry types (a) d-type and (b) k-type by Jimenez [15]

width-to-height ratio results in an increase in turbulence statistics.

Leonardi et al. [48] studied the effect of changing the width to height ratio on turbulence behaviour for a square roughness element on one wall at $Re_\tau =$ 180 number in terms of the fluctuation velocity contours in addition to higher order statistics for a wide range of width to height ratios equal to $w/k = 1-$ 19. In terms of the fluctuating velocity contours in horizontal planes, it was noticed that the fluctuations in the streamwise direction tended to increase due to the increase in the momentum exchange within the outer layer. The width of the velocity streaks in the spanwise direction was larger than for the smooth case. In terms of the spatially averaged fluctuating velocity statistics, it was noticed that for the wall-normal and spanwise directions the increase in the width-to-height ratio is directly proportional to the fluctuating velocity profile.

Modesti et al. [49] studied the contribution of dispersive effect for Asymmetric triangular, symmetric triangular, trapezoidal and blade shape textured surfaces for a minimal open channel flow at different groove lengths, spacings and aspect ratios at $Re_\tau = 395$. The riblets spacings range in wall units was between 15 and 50, the roughness height range was between 7.5 and 25 and the roughness elements aspect ratio varied between 0.5 and 1.88. The aspect ratio is equivalent to the width-to-height ratio defined earlier. It was found that for the case of small grooves the drag reduction was obtained by shifting the virtual origin away from the wall thus increasing the effective mean velocity at the crest. Large grooves however, act beyond the viscous sublayer thus generated additional crest. Part of this stress is due to turbulent fluctuations where the crest is caused by the secondary flow filling the riblet grooves. The relative contribution towards these stress components was found to be dependent on the aspect ratio. As the aspect ratio increases, the effect of dispersive effect tends to decrease. Also, it was found that for the case of small aspect ratio less than 0.5, more drag reduction can be obtained. There are very few studies on the effect of roughness in unsteady flows. Seddighi et al. [25] studied the turbulence for transient channel flow with pyramid roughness elements on the lower wall. The interaction of the perturbed flow due to the rough wall was characterised by observing the roughness induced laminar turbulent-transition. The flow was characterised in terms of λ_2. Also, the analysis included higher order turbulence statistics like the anisotropy, Reynolds shear stress and pre-multiplied spectra. The use of phase averaging significantly reduced the profiles compared to spatial averaging for fluctuating velocities. The authors found that the turbulent-turbulent transition over the pyramid channel flow, following a flow rapid increase, exhibits a roughness induced laminar-turbulent transition despite the fact that the initial flow from which the acceleration starts, was fully turbulent.

2.4 Textured Surfaces Turbulent Flow at Different Reynolds Numbers.

For textured surfaces, the majority of the previous literature focused on studying the effect of changing textured surfaces geometry conditions on the flow behaviour and drag performance for laminar and turbulent flow. Martel et al. [38] mentioned earlier, studied the effect of using the same SHS array at different Reynolds numbers and compared them against each other for $Re_\tau = 180, 395$ and 590 (see section 2.1.2.1) unlike the majority of literature where the main focus was to study the effect of altering geometry conditions at the same Reynolds number .

For smooth channel flows shown in Figure 2.15, Moser et al. [16] performed DNS simulations for turbulent channel flows and studied the effect of Reynolds number increase on the turbulence statistics at $Re_\tau = 180, 395$ and 590. The authors analysed the effect of increasing the Reynolds number for channel flows described in terms of the spatially averaged profiles, root mean square of fluctuating profiles and root mean square of vorticity profiles. For spatially averaged profiles it was noticed that as the Reynolds number increases particularly $Re_\tau = 590$, the "low Reynolds number effects" are fewer, these effects include: the very short log-layer, the apparent log-law large intercept compared against higher Reynolds numbers and the spatially averaged profile disagreement with higher Reynolds number cases beyond $y^+ = 10$.

In terms of the root mean square of fluctuating velocities, it was noticed that the velocity profiles increase as the Reynolds number increases in the streamwise, wall-normal and spanwise directions. Also, the peak of maximum velocity is shifted away from the wall when plotted in wall normal units as Reynolds number increases.

For the root mean square of vorticity profiles it was noticed that the vorticity profiles increase as Reynolds number increases in the streamwise, wall-normal and spanwise directions. However, unlike the fluctuating velocities, the location of the peak vorticity is independent of the change in Reynolds numbers.

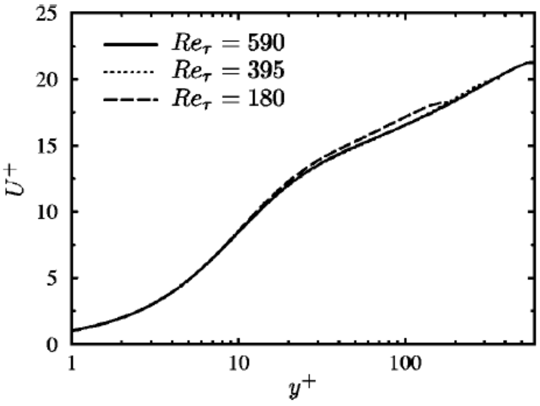

(a) Spatially averaged velocity.

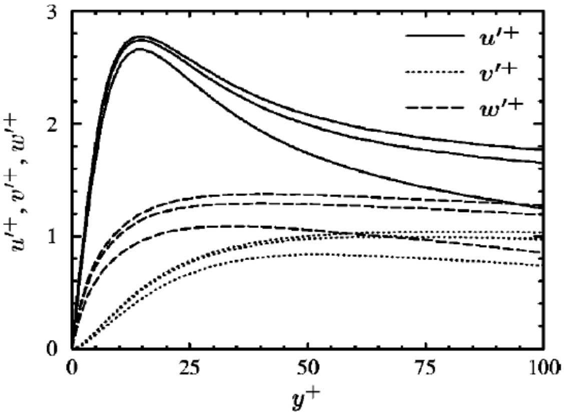

(b) Spatially averaged fluctuating velocities.

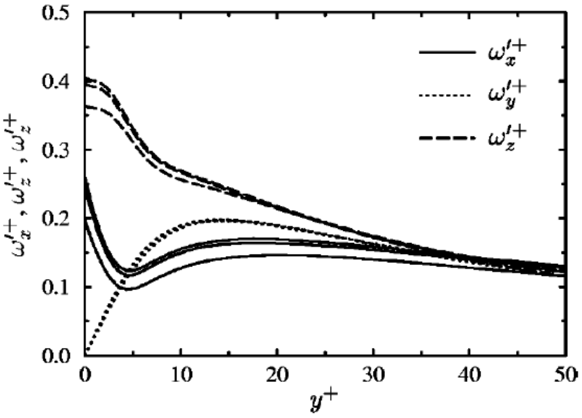

(c) Spatially averaged fluctuating vorticities.

Figure 2.15: Moser et al. [16] smooth channel turbulence statistics at different Reynolds numbers.

Chapter 3

Direct Numerical Simulations In-house Computer Code CHAPSim

This chapter is dedicated to describe the theory behind the presented work including an introduction to the in-house DNS code CHAPSim. The chapter includes an overview of the most common CFD approaches, a brief history of the in-house code used, in addition to the list of updates applied to the code. Also, presented in this chapter are descriptions of the implementation of the spatial and temporal methods used in the code, boundary conditions assigning for the smooth channel simulations, initial conditions, statistical calculations, vortex identification using λ_2, code parallelisation and optimisation methods. The code validation against benchmark data is also discussed.

3.1 CFD Approaches

The governing equations of incompressible fluid flow are the conservation of mass (continuity) and conservation of momentum (Navier-Stokes) can be presented as follows,
Conservation of mass:

$$\frac{\partial u_i^*}{\partial x_i^*} = 0 \tag{3.1}$$

Navier-Stokes:

$$\frac{\partial u_i^*}{\partial t^*} + u_j^* \frac{\partial u_i^*}{\partial x_j^*} = -\frac{\partial p^*}{\partial x_i^*} + \frac{1}{Re} \frac{\partial^2 u_i^*}{\partial x_j^* \partial x_j^*} \tag{3.2}$$

The main CFD approaches used to study flows by solving Equations. (3.2 and 3.1) can be categorized into the following groups: Reynolds Averaged Navier-Stokes Equations (RANS), Direct Numerical Simulations (DNS) and Large Eddy Simulations (LES).

3.1.1 Reynolds Averaged Navier-Stokes Equations (RANS)

The Reynolds Averaged Navier Stokes Equations (RANS) is the most popular CFD approach among the CFD industry. The RANS approach is based on the classical approach of Osborne Reynolds. Mainly, the velocity and pressure quantities are decomposed to mean and fluctuation components expressed as shown,

$$u_i^* = \bar{u}_i{}^* + u_i^{'*} \tag{3.3}$$

$$p^* = \bar{p}^* + p^{'*} \tag{3.4}$$

where the $(-)$ symbol denotes the mean values and the $(')$ denotes the fluctuating components. The governing Equations. (3.2) and (3.1) become as follows,
Momentum equation:

$$\frac{\partial \bar{u}_i^*}{\partial t^*} + \bar{u}_j^* \frac{\partial \bar{u}_i^*}{\partial x_j^*} = -\frac{\partial \bar{p}^*}{\partial x_i^*} + \frac{1}{Re} \frac{\partial^2 \bar{u}_i^*}{\partial x_j^* \partial x_j^*} - \overline{\frac{\partial u_i'^* u_j'^*}{\partial x_j^*}} \tag{3.5}$$

Conservation equation:

$$\frac{\partial \bar{u}_i^*}{\partial x_i^*} = 0 \tag{3.6}$$

the additional velocity components $\overline{\frac{\partial u_i'^* u_j'^*}{\partial x_j^*}}$ are to be solved using RANS turbulence models. A large number of turbulence models are available to solve different problems for various applications. Until now, it is hard to say that one model shows the best approximation of the Reynolds stresses or can be generalized among all CFD applications. Examples of popular used turbulence models are the $k - \omega$ and the $k - \epsilon$. The use of RANS is mainly implemented in commercial CFD packages and widely used for applications like the aerospace and the automotive industries due to the accuracy, cost efficient combination.

3.1.2 Direct Numerical Simulations (DNS)

Direct Numerical Simulations (DNS) is potentially the most accurate yet most expensive method to solve the Navier-Stokes equations, it does not involve any modelling and captures all the turbulent flow eddies regardless how small they are. The development of the DNS capabilities is directly related to the growth of supercomputers. It started with humble trials to perform 32^3 isotropic simulations by Orzag and Patterson in 1972 [50]. In the 1970s the use of DNS was restricted to inhomogeneous 1D flows and DNS was incapable of analysing any wall-bounded turbulence problem until 1987 when Kim at al. [20] performed a plane channel flow simulation, which proved DNS to be an extremely useful tool to study wall-bounded turbulence. Although the major use of DNS approaches was limited to small Reynolds number, there have been a number of higher Reynolds numbers advances where channel flows were analysed using DNS. Recently, there have been a number of studies which used DNS at high Reynolds number for example: Alcantara et al. [51] who studied thermal channel flows using DNS for friction Reynolds number $Re_\tau = 2000$ and Yamamoto and Tsuji [52] who investigated logarithmic regions for channel flow at a friction Reynolds number $Re_\tau = 8000$.

3.1.3 Large Eddy Simulations (LES)

The Large Eddy Simulations (LES) technique is considered a compromise between RANS and DNS first used by Deardorff [53] back in 1970 who performed LES simulations for turbulent channel flow. It is based on the elimination of smaller scales as they are universal, homogeneous and unaffected by boundary layers using low pass filtering. Applying the suitable turbulence model, LES methods are capable of modelling unsteady flow physics equations accurately representing the influence of smaller scales on larger ones [54]. For the case of LES, the velocity component is split into spatially averaged resolved and sub-grid parts. The resolved part represents the large eddies where the sub-grid part represents the smaller scales where

$$u_i^* = < \overline{u}_i^* > + u_i^{'*} \tag{3.7}$$

$$p^* = < \overline{p}^* > + p^{'*} \tag{3.8}$$

substituting the decomposition terms into the Navier-Stokes and continuity equations becomes as follows,

$$\frac{\partial < \overline{u_i}^* >}{\partial x_i^*} = 0 \tag{3.9}$$

$$\frac{\partial < \bar{u}_i^* >}{\partial t^*} + < \bar{u_j}^* > \frac{\partial < \bar{u_i}^* >}{\partial x_j^*} = - \frac{\partial < \bar{p}^* >}{\partial x_i^*} + \frac{1}{Re} \frac{\partial^2 < \bar{u}_i^* >}{\partial x_j^* \partial x_j^*} + \frac{\partial \tau_{ij}^*}{\partial x_j^*} \tag{3.10}$$

The term $\frac{\partial \tau_{ij}}{\partial x_j}$ arises due to the non-linear advection term expressed in the equation as follows,

$$< \overline{u_j^* \frac{\partial u_i^*}{\partial x_j^*}} > \neq < \overline{u}_j^* > \frac{\partial < \overline{u}_i^* >}{\partial x_j^*} \tag{3.11}$$

and thus τ_{ij} is calculated as follows,

$$\tau_{ij}^* = < \overline{u}_i^* \overline{u}_j^* > - < \overline{u_i^* u_j^*} > \tag{3.12}$$

Similar to RANS, there are a number of models to solve the subscale terms examples of which include: Smagorinsky model and Algebraic dynamic model.

3.2 Channel and Pipe Simulator (CHAPSim)

An In-house DNS/LES Channel and Pipe Simulator (CHAPSim) is used for the present study. The in-house solver is based on the open-source solver written by Kajishima [55]. Seddighi [18], [25] carried on the development of the code and improved its efficiency. The spatial derivatives for DNS flows

are calculated using a second-order finite difference method. A third order Rung-Kutta together with a second order Crank-Nicholson scheme are used for the convective and viscous terms, respectively. The time advancement method is based on a fractional step method introduced by Kim and Moin [20]. The resulting Poisson equation is solved using a 2D fast Fourier transformation taking advantage of the flow periodicity in the streamwise and spanwise directions. Statistical calculations were developed through the turbulence statistics subroutine. The code is parallelised using hybrid Message Passing Interface (MPI) and Open Multi Processing (OMP) methods.
Initially the code was developed for smooth and 2D roughness flows [17]. Later on, LES [56] and pipe flows [57] were implemented to the code. The roughness was treated using an IBM which is explained in detail in chapter 4. The major changes that have been made to the code during the course of the present research include the following:

- The implementation of the novel geometry inspired by the Backswimmer insect
- The implementation of the MPI/OMP model to optimise the parallel performance of the code and enhance its scalability
- Modernisation was performed on the post processing subroutines from Fortran 77 to Fortran 90 to improve the memory usage of the code and widen its usage across different HPC environments

3.2.1 Governing Equations

The governing equations are solved for an incompressible flow. Continuity and N-S equations are solved in non-dimensional form using DNS. The equations including conservation of mass and N-S momentum equations are as below,
x-momentum:

$$\frac{\partial u^*}{\partial t^*} + u^*\frac{\partial u^*}{\partial x^*} + v^*\frac{\partial u^*}{\partial y^*} + w^*\frac{\partial u^*}{\partial z^*} = -\frac{\partial \overline{p}^*}{\partial x^*} - \frac{\partial p'^*}{\partial x^*} + \frac{1}{Re_p}(\frac{\partial^2 u^*}{\partial x^{*2}} + \frac{\partial^2 u^*}{\partial y^{*2}} + \frac{\partial^2 u^*}{\partial z^{*2}}) \tag{3.13}$$

y-momentum:

$$\frac{\partial v^*}{\partial t^*}+u^*\frac{\partial v^*}{\partial x^*}+v^*\frac{\partial v^*}{\partial y^*}+w^*\frac{\partial v^*}{\partial z^*}=-\frac{\partial p'^*}{\partial x^*}+\frac{1}{Re_p}(\frac{\partial^2 v^*}{\partial x^{*2}}+\frac{\partial^2 v^*}{\partial y^{*2}}+\frac{\partial^2 v^*}{\partial z^{*2}}) \quad (3.14)$$

z-momentum:

$$\frac{\partial w^*}{\partial t^*}+u^*\frac{\partial w^*}{\partial x^*}+v^*\frac{\partial w^*}{\partial y^*}+w^*\frac{\partial w^*}{\partial z^*}=-\frac{\partial p'^*}{\partial x^*}+\frac{1}{Re_p}(\frac{\partial^2 w^*}{\partial x^{*2}}+\frac{\partial^2 w^*}{\partial y^{*2}}+\frac{\partial^2 w^*}{\partial z^{*2}}) \quad (3.15)$$

Conservation of mass:

$$\frac{\partial u^*}{\partial x^*}+\frac{\partial v^*}{\partial y^*}+\frac{\partial w^*}{\partial z^*}=0 \quad (3.16)$$

$$\begin{aligned}
x^* &= x/\delta\\
y^* &= y/\delta\\
z^* &= z/\delta\\
u^* &= u/U_P\\
v^* &= v/U_P\\
w^* &= w/U_P\\
t^* &= \frac{t}{\delta/U_P}\\
p^* &= \frac{p}{\rho U_P^2}\\
Re_p &= \frac{U_P\delta}{\nu}
\end{aligned} \quad (3.17)$$

where δ is the channel half-height, U_P is the Poiseuille flow laminar velocity and ν is the kinematic viscosity.

3.3 Spatial and Temporal Discretisation Methods

This section covers a brief description of the discretisation approaches used in CHAPSim for the present work. The explanations include the finite difference method, Adam Bashfort/ Crank Nicholson and the Rung-Kutta/Crank

Nicholson methods.

3.3.1 Spatial Derivatives

For the case of DNS codes, the most common methods used for calculating spatial derivatives are spectral methods and finite difference methods. The spectral methods can achieve the best accuracy for spatial discretisation [20]. However, spectral methods cannot be used for complex geometries or for large distributed memory systems which has limited its usage in recent research applications. The finite difference methods are more popular for DNS flows over textured surfaces (see Table 2.3).

Finite difference methods are based on Taylor series expansion. The order of the finite difference expression is a major factor in enhancing the finite difference method accuracy. The finite difference methods are capable of handling complex geometries compared against spectral methods and perform well for parallel distributed memory systems. However, finite difference schemes require more grid points than spectral methods to achieve the same accuracy [58].

3.3.2 Spatial Discretisations in CHAPsim

CHAPSim uses second order finite difference method to discretise the spatial terms of the governing equations. To do so, the differentiation operator ∂ is substituted by first and second order discrete δ operators and thus the discretised form of the governing equations (Equations. 3.13-3.16) become,

$$\frac{\delta u^*}{\delta t^*}+u^*\frac{\delta u^*}{\delta x^*}+v^*\frac{\delta u^*}{\delta y^*}+w^*\frac{\delta u^*}{\delta z^*}=-\frac{\delta \overline{p}^*}{\delta x^*}-\frac{\delta p^{'*}}{\delta x^*}+\frac{1}{Re_p}\left(\frac{\delta^2 u^*}{\delta x^{*2}}+\frac{\delta^2 u^*}{\delta y^{*2}}+\frac{\delta^2 u^*}{\delta z^{*2}}\right) \tag{3.18}$$

$$\frac{\delta v^*}{\delta t^*}+u^*\frac{\delta v^*}{\delta x^*}+v^*\frac{\delta v^*}{\delta y^*}+w^*\frac{\delta v^*}{\delta z^*}=-\frac{\delta p^{'*}}{\delta x^*}+\frac{1}{Re_p}\left(\frac{\delta^2 v^*}{\delta x^{*2}}+\frac{\delta^2 v^*}{\delta y^{*2}}+\frac{\delta^2 v^*}{\delta z^{*2}}\right) \tag{3.19}$$

$$\frac{\delta w^*}{\delta t^*}+u^*\frac{\delta w^*}{\delta x^*}+v^*\frac{\delta w^*}{\delta y^*}+w^*\frac{\delta w^*}{\delta z^*}=-\frac{\delta p^{'*}}{\delta x^*}+\frac{1}{Re_p}\left(\frac{\delta^2 w^*}{\delta x^{*2}}+\frac{\delta^2 w^*}{\delta y^{*2}}+\frac{\delta^2 w^*}{\delta z^{*2}}\right) \tag{3.20}$$

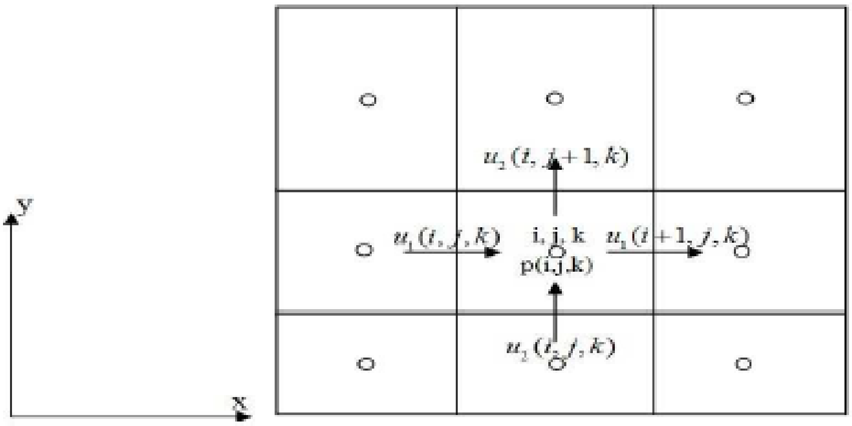

Figure 3.1: Staggered grid schematic in the x-y direction used in CHAPSim [17].

$$\frac{\delta u^*}{\delta x^*} + \frac{\delta v^*}{\delta y^*} + \frac{\delta w^*}{\delta z^*} = 0 \tag{3.21}$$

Staggered grid is adopted to the code which implies that the pressure and velocities are located at the centre and the surfaces of mesh cells respectively (see Figure 3.1) The notation shown in Figure 3.1 is used for the implementation. It should be noted that the mesh size should be small enough to resolve the smallest scales of motion yet large enough so that the boundary conditions do not influence the statistics. Uniform grids are used in the streamwise and the spanwise directions. For the wall-normal direction, non-uniform grids are used due to the significant gradient of the properties near the wall. For the smooth channel non-uniform grids are used for the region from the base wall to the channel centre. For the textured channel, a fine uniform grid is used for the distance between the channel base wall and the crest of the texture where $\Delta x^+ < 20$, $\Delta z^+ < 10$ and $\Delta y^+ < 5$ [59]. Non-uniform grids are used from the roughness crest to the centre of the channel. The non-uniform method is performed using a *tanh* function as shown below,

$$y_v(j) = 0.5(1 + tanh(0.5(\frac{2j-1}{N_y}log(\frac{1+A_{LG}}{1-A_{LG}}))/A_{LG}) \tag{3.22}$$

$$y_p(j) = 0.5(1 + tanh(0.5(\frac{2j-1.5}{N_y}log(\frac{1+A_{LG}}{1-A_{LG}}))/A_{LG}) \tag{3.23}$$

where j is the cell number, N_y is the total number of cells in wall-normal direction and A_{LG} is the non-uniformity coefficient.
The discretised form of the convective terms of the streamwise equation using the second order central difference scheme is shown for the lower wall and internal nodes as shown in Equation 3.24 and Equation 3.25 respectively.
Lower wall:

$$\begin{aligned}&Lu = -\frac{1}{2\Delta x}\{[u(i-1,j,k)+u(i,j,k)]\times[-u(i-1,j,k)+u(i,j,k)]+[u(i,j,k)\\&+u(i+1,j,k]\times[-u(i,j,k)+u(i+1,j,k)]]\}/2+-\frac{1}{2\Delta z}\{[w(i,j,k)+w(i-1,j,k)]\times\\&[-u(i,j,k)+u(i,j,k+1)]+[w(i,j,k-1)+w(i-1,j,k-1)]\times[-u(i,j,k-1)+\\&u(i,j,k)]]\}/2+-\{-\beta_0(j)\times[\alpha_1(j)\times u(i,j,k)+\beta_1(j)\times u(i,j+1,k)]\times[v(i,j,k)\\&+v(i+1,j,k)]/2\}\end{aligned}\tag{3.24}$$

Internal nodes:

$$\begin{aligned}&Lu = -\frac{1}{2\Delta x}\{[u(i-1,j,k)+u(i,j,k)]\times[-u(i-1,j,k)+u(i,j,k)]+[u(i,j,k)\\&+u(i+1,j,k]\times[-u(i,j,k)+u(i+1,j,k)]]\}/2-\frac{1}{2\Delta z}\{[w(i,j,k)+w(i-1,j,k)]\\&\times[-u(i,j,k)+u(i,j,k+1)]+[w(i,j,k-1)+w(i-1,j,k-1]\times[-u(i,j,k)+u(i\\&,j,k+1)]]\}/2+\{-\alpha_0(j)\times[\alpha_1(j)\times u(i,j-1,k)+\beta_1(j)\times u(i,j,k)]\times[v(i,j-1,k)\\&+v(i+1,j-1,k)]/2\}+\{-\beta_0(j)\times[\alpha_1(j)\times u(i,j,k)+\beta_1(j)\times u(i,j+1,k)]\times[v(i,\\&j,k)+v(i+1,j,k]/2\}\end{aligned}\tag{3.25}$$

where $\alpha_0(j)$, $\alpha_1(j)$, $\beta_0(j)$ and $\beta_1(j)$ are calculated based on the location of the surface nodes and the wall-normal distances as follows,

$$\alpha_0(j) = \frac{y_v(j) - y(j)}{\Delta y_v(j)} \tag{3.26}$$

$$\alpha_1(j) = -\frac{1}{\Delta y(j)} \tag{3.27}$$

$$\beta_0(j) = \frac{y(j) - y_v(j-1)}{\Delta y_v(j)} \tag{3.28}$$

$$\beta_1(j) = \frac{1}{\Delta y(j)} \tag{3.29}$$

3.3.3 Time Advancement

Currently the most used time advancement methods in DNS simulations are the Adam Bashfort/ Crank Nicholson and the Runge-Kutta / Crank Nicholson methods. Both methods are semi-implicit and second order. Implicit schemes are used to calculate viscous terms and explicit schemes are used to calculate the convective terms of the N-S equations. One important parameter to be considered before implementing the time advancement method is the time accuracy required versus the corresponding storage required for the arrays. More accurate schemes usually require a large number of arrays, hence higher computational cost and time.

The Crank Nicholson method is a second order time implicit method. This method is unconditionally stable in time which means any time step Δt of arbitrary size can be used. The error of that method is $O(\Delta t^2)$. The Adams-Bashfort explicit method is stable and simple to program.

The following three steps are used for each time advancement based upon a fractional step method as follows,

Step 1.

$$\hat{u}_i = u_i^n + \Delta t(\gamma_1 H_i^n + \zeta_1 H_i^{n-1} + \frac{\alpha_1}{2Re_p}(\frac{\delta^2}{\delta x_1^2} + \frac{\delta^2}{\delta x_2^2} + \frac{\delta^2}{\delta x_3^2})(\hat{u}_i + u_i^n) - \alpha_1(G_i p'^n + S_i^n)) \tag{3.30}$$

$$\nabla^2 \phi^a = \frac{-1}{\alpha_1 \Delta t} D(\hat{u}_i) \tag{3.31}$$

$$\frac{u_i^a - \hat{u}_i}{\Delta t} = -\alpha_1 G_i \phi^a \tag{3.32}$$

$$p^a = p^n + \phi^a - \frac{\alpha_1 \Delta t}{2Re_p} \nabla^2 \phi^a \tag{3.33}$$

Step 2.

$$\hat{\hat{u}}_i = u_i^a + \Delta t(\gamma_2 H_i^a + \zeta_2 H_i^n + \frac{\alpha_2}{2Re_p}(\frac{\delta^2}{\delta x_1^2} + \frac{\delta^2}{\delta x_2^2} + \frac{\delta^2}{\delta x_3^2})(\hat{\hat{u}}_i + u_i^a) - \alpha_2(G_i p'^a + S_i^a)) \tag{3.34}$$

$$\nabla^2 \phi^b = \frac{-1}{\alpha_2 \Delta t} D(\hat{\hat{u}}_i) \tag{3.35}$$

$$\frac{u_i^b - \hat{\hat{u}}_i}{\Delta t} = -\alpha_2 G_i \phi^b \tag{3.36}$$

$$p^b = p^a + \phi^b - \frac{\alpha_2 \Delta t}{2Re_p} \nabla^2 \phi^b \tag{3.37}$$

Step 3.

$$\hat{\hat{\hat{u}}}_i = u_i^b + \Delta t(\gamma_3 H_i^b + \zeta_3 H_i^a + \frac{\alpha_3}{2Re_p}(\frac{\delta^2}{\delta x_1^2} + \frac{\delta^2}{\delta x_2^2} + \frac{\delta^2}{\delta x_3^2})(\hat{\hat{\hat{u}}}_i + u_i^b) - \alpha_3(G_i p'^b + S_i^b)) \tag{3.38}$$

$$\nabla^2 \phi^{n+1} = \frac{-1}{\alpha_3 \Delta t} D(\hat{\hat{\hat{u}}}_i) \tag{3.39}$$

$$\frac{u_i^{n+1} - \hat{\hat{\hat{u}}}_i}{\Delta t} = -\alpha_3 G_i \phi^{n+1} \tag{3.40}$$

$$p^{n+1} = p^b + \phi^{n+1} - \frac{\alpha_3 \Delta t}{2Re_p} \nabla^2 \phi^{n+1} \tag{3.41}$$

where H_i is the discretised operator for the non-linear terms, $G_i p'$ is the discrete fluctuation pressure gradient operator, ϕ is the quantity used to obtain solenoidal velocities and pressure and S_i is the mean pressure gradient in the streamwise direction. All the other parameters, constants and their corresponding values are shown in Table 3.1.

Table 3.1: Factorisation step method constants for all three time steps.

Constant	Value
γ_1	8/15
γ_2	5/12
γ_3	3/4
ζ_1	0.0
ζ_2	−17/60
ζ_3	−5/12
$\alpha_1 = \gamma_1 + \zeta_1$	8/15
$\alpha_2 = \gamma_2 + \zeta_2$	2/15
$\alpha_3 = \gamma_3 + \zeta_3$	1/3

3.4 Boundary Conditions

Three boundary conditions are used for the upper and lower channel walls. For the case of smooth channel flow, periodic boundary condition is applied in the streamwise and spanwise directions and no-slip boundary is applied in the wall-normal direction. For the case of textured surfaces simulations, an IBM is used which will be explained in detail in chapter 4. For the case of periodic boundary condition, the value of the quantities are simply set equal at the first and last surfaces. For the case of the wall-normal direction, the no-slip boundary for the second derivative at the lower wall for the first point away from bottom wall should be treated specifically (see section 4.1.1).

3.5 Initial Conditions

All the presented simulations are undertaken for steady flow test cases. As fully developed channel flow is required for all the test cases, the initial conditions should not affect the results. A streamwise velocity with added disturbance is necessary to make sure the initial flow does not reverse back to a laminar flow. A laminar Poiseuille parabolic profile is produced using $\frac{U(y)}{u_p} = 1 - (\frac{y}{\delta})^2$, where y is the distance from the wall. Afterwards, a random zero-mean disturbance is added to this laminar profile. It should be noted that all the cases for the smooth and textured channel cases were calculated when the simulations reached a steady state condition.

3.6 Statistics Calculation

Post-processing subroutines are developed to calculate turbulence statistics from the instantaneous velocity and pressure fields produced by the solver using Ergodic hypothesis. Initially, computations are carried out for a time period, by then the flow will reach statistical equilibrium. Afterwards, the time and space averaged values for the turbulence statistics are recorded and saved in a file with binary format which is then read by the developed post-processing code in order to:

- Ensemble-average the spatially averaged statistics
- Produce appropriate Tecplot and Matlab format files of the desired statistics

Tecplot360 and Matlab packages were used to present the data for the presented work.

3.6.1 Mean Velocity

The calculation of the spatially averaged velocity is a crucial quantity to quantify the change in the drag performance using textured surfaces. It is calculated as,

$$\overline{u}(j) = \frac{1}{N_l N_x N_z} \sum_{l=1}^{N_l} \sum_{k=1}^{N_z} \sum_{i=1}^{N_x} u_d(i, j, k, l) \tag{3.42}$$

where $u_d(i, j, k, l)$ is the instantaneous velocity where the subscript d denotes the velocity component; N_x N_z are the number of mesh cells in the streamwise and spanwise directions, respectively and N_l is the number of instantaneous flow fields used for ensemble-averaging.

3.6.2 RMS of Fluctuating Velocity

The root-mean-square of turbulent fluctuating velocities can be calculated as follows,

$$u''_{rms}(j) = \sqrt{\frac{1}{N_l N_x N_z} \sum_{l=1}^{N_l} \sum_{k=1}^{N_z} \sum_{i=1}^{N_x} [u_d(i,j,k,l) - \overline{u}_d(j)]^2} \qquad j = 1, N_y \tag{3.43}$$

where the notations are the same as those used in Equation 3.42. Similar calculations are used to calculate the fluctuating velocities in the wall-normal v''_{rms} and spanwise directions w''_{rms}.

3.6.3 RMS of Fluctuating Vorticity

The root-mean-square of fluctuating vorticities are calculated as follows,

$$\begin{aligned} \omega''_x &= \frac{\partial w''}{\partial y} - \frac{\partial v''}{\partial z} \\ \omega''_y &= \frac{\partial u''}{\partial z} - \frac{\partial w''}{\partial x} \\ \omega''_z &= \frac{\partial v''}{\partial x} - \frac{\partial u''}{\partial y} \end{aligned} \tag{3.44}$$

where u'', v'' and w'' are the fluctuating velocities in the streamwise, wall-normal and spanwise directions. As staggered grid is used at cell surfaces, the gradient components are evaluated first at the edge of the cell, then the components are interpolated at the cell centre.

3.6.4 Turbulent, Viscous and Total Stresses

The turbulent and viscous stresses are calculated as shown,
Turbulent stress:

$$S_T = \overline{u''^{*} v''^{*}} \tag{3.45}$$

Viscous stress:

$$S_V = \frac{1}{Re_c}\frac{\partial \overline{u}^*}{\partial y^*} \tag{3.46}$$

Total stress:

$$S_A = S_T + S_V \tag{3.47}$$

To evaluate the viscous stress, the mean values of $\overline{u^*}$ are calculated at the cell centre for the lower and the upper surface of the cell as follows,
At lower surface:

$$S_{V_l}(j,t) = \frac{1}{Re_p}\frac{\overline{u^*}(j,t) - \overline{u^*}(j-1,t)}{\Delta y^*(j) - \Delta y^*(j-1)} \tag{3.48}$$

At upper surface:

$$S_V(j+1,t) = \frac{1}{Re_p}\frac{\overline{u^*}(j+1,t) - \overline{u^*}(j,t)}{\Delta y^*(j+1) - \Delta y^*(j)} \tag{3.49}$$

The viscous stress at the centre is calculated as follows,

$$S_V(j,t) = 0.5[S_V(j,t) + S_V(j+1,t)] \tag{3.50}$$

3.7 Vortex Identification

The vortex identification is calculated and plotted using λ_2 criterion proposed by Jeong and Hussain [6]. The presence of vortical structures is related to the production of shear stress. For the study of drag performance, vortical structure analysis is performed to capture the organised motion of turbulence which in addition to the turbulence shear stresses and quadrant analysis contribute towards the levels of skin friction [5]. λ_2 is the second largest Eigen value for the symmetric tensor $S^2 + \Omega^2$ where $S = 0.5(A + A^T)$, $\Omega = 0.5(A - A^T)$ and $A_{ij} = \frac{\partial u_i}{\partial x_j}$ are respectively the symmetric and anti-symmetric parts of the velocity gradient tensor $\frac{\partial u_i^*}{\partial x_j^*}$ shown as,

$$\frac{\partial u_i^*}{\partial x_j^*} = \begin{bmatrix} \frac{\partial u_1^*}{\partial x_1^*} & \frac{\partial u_1^*}{\partial x_2^*} & \frac{\partial u_1^*}{\partial x_3^*} \\ \frac{\partial u_2^*}{\partial x_1^*} & \frac{\partial u_2^*}{\partial x_2^*} & \frac{\partial u_2^*}{\partial x_3^*} \\ \frac{\partial u_3^*}{\partial x_1^*} & \frac{\partial u_3^*}{\partial x_2^*} & \frac{\partial u_3^*}{\partial x_3^*} \end{bmatrix} \tag{3.51}$$

3.8 Parallelisation of the Code

3.8.1 MPI

Message Passing Interface (MPI) is a standardized portable message passing specification for memory distributed systems shown in Figure 3.2(a). MPI libraries are scalable for large size problems demanding a high number of cores. MPI is a popular parallelisation method as it offers a wide range of libraries compatible with many HPC facilities in addition to being free and optimised for a wide range of high-speed networks. The main drawback of the use of MPI is its complexity to program [60]. For the case of CHAPSim the MPI drawbacks are summarized as follows,

- The large number of smaller MPI messages accompanied with short period regions of the code causing a large number of communication messages.
- The use of nested FOR loops specially the MPI send, receive, read and write functions.
- A 1D decomposition of the domain, hence, (i) less efficient compared to more dimensional domain decomposition and (ii) limit the number of processes to the total number of mesh points in the wall-normal direction which is usually less than that in other directions (i.e. streamwise and spanwise).

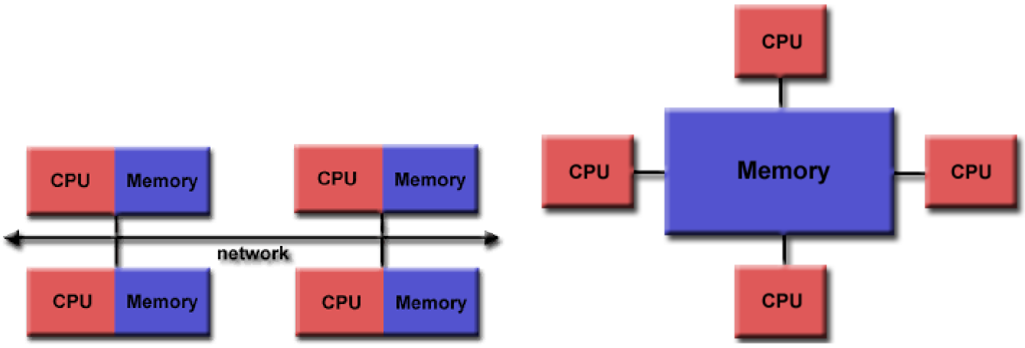

(a) MPI (b) OMP

Figure 3.2: Distributed and shared memory structures for (a) MPI and (b) OMP [18].

3.8.2 OMP

OpenMP is used for shared memory parallelisation shown in Figure 3.2(b). OpenMP is considered easier to program compared to the complexity associated with using MPI libraries. The implementation of OpenMP is a gradual iterative progression, where the code does not have to be re-written from scratch to apply the parallelisation directives to the serial version of the code. The use of OpenMP is limited to problems requiring less than 16 cores which makes it impractical for CFD applications, however, it opened the way to parallel MPI-OMP technique as a useful method to improve and optimise the performance of CFD codes [61] .

3.8.3 Hybrid Parallelisation

The hybrid MPI-OMP method combines the use of MPI functions together with OMP directives to improve the performance of MPI parallel codes. This method can be effective for cases where shared memory algorithms can improve inefficient MPI-only implementation. This method is usually applied to MPI-only codes in order to improve their speed-up performance or fix memory distribution issues for MPI-only codes. It is considered easy to program. However, its effectiveness is highly dependent on the compiler used, software and hardware environments.

3.9 Code Optimisation

3.9.1 2D Decomposition

The 1D decomposition also known as the slab decomposition is a simple way to perform parallel computations on distributed and shared memory systems. For 1D decomposition shown in Figure 3.3(a) the computational domain is decomposed in one direction. The number of slices within the computational domain is specified with respect to the numbers of processors assigned; this limits the simulations to the cell count in the decomposed direction, specially for the cases where a larger number of cells is needed in the other directions. An extension to the 1D decomposition is the 2D pencil decomposition in which the computational domain is decomposed into two directions shown in Figure 3.3(b). Li and Laizet [19] developed a 2-D decomposition tool to the DNS code INCOMPACT3D and showed the effect of the 2D decomposition on performance of the code as mainly enhancing its scalability which made their code scalable for up to one million cores. The main disadvantage of using the 2D decomposition method is its complexity to program. Additionaly, The code has to be restructured in order to demonstrate the impact of 2D decomposition on the code performance.

3.9.2 Hybrid Parallelisation

The use of hybrid MPI-OMP technique is an effective optimization technique to improve the performance of MPI-only CFD codes. The efficiency of the hybrid model is dependent on both the hardware used and the compilation environment. Rabenseifner [62] reviewed various MPI-OMP programming techniques and compared them against pure MPI simulations. Bassi et al. [63] tested the efficiency of the hybrid MPI-OMP on their DNS code and found that the improvement in the performance is mainly dependent on the number of MPI ranks and OMP threads for a problem of a certain size.

In the present study MPI-OMP is applied to the code by adding OMP directives to the subroutines consuming most of the CPU time. The OMP

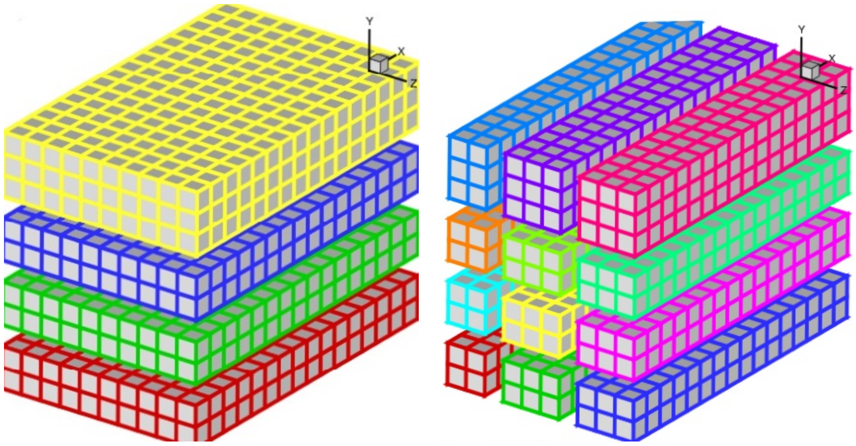

(a) 1-D Decomposition (b) 2-D Decomposition

Figure 3.3: Computational decomposition models (a) 1D decomposition and (b) 2D decomposition by Li and Laizet [19].

directives has the symbol !$\$OMP$. Accordingly, first the subroutines/sections which take the most of simulation time are identified. Then, the OMP directives were applied to the nested for loops which contained the $MPI\_Send\_Recive()$ functions as they consume most of the CPU time. Also, the OMP directives are applied to the smaller regions of the code that generate large numbers of MPI communications compared against their actual required time to finish the job in serial mode. The syntax used in applying the OMP directives to a nested MPI only for loop subroutine is shown in Figure 3.4 as explained and tested by Mallon et al. [60].

3.10 Code Modernisation

Scientific programming has been widely used for the past few years. According to statistics obtained from the UK national supercomputing facility [64], more than 80% of their submitted jobs consist of Fortran codes. Although it is one of the oldest programming languages, it is still the most popular programming language in the scientific programming field due to its high efficiency for parallel applications using MPI. Fortran 66 was the first ANSI standardised version and it did introduce common data types like integers

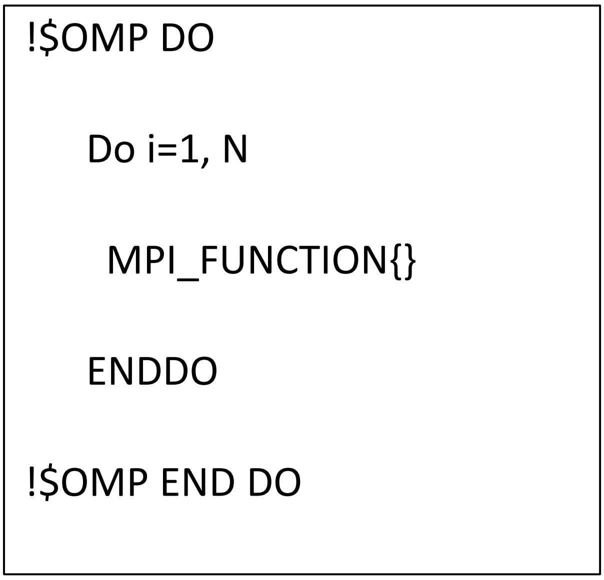

```
!$OMP DO

     Do i=1, N

       MPI_FUNCTION{}

     ENDDO

!$OMP END DO
```

Figure 3.4: OMP Directives for MPI only FOR loops.

and double precision. Also it was the first to introduce IF and DO statements. Later on, Fortran 77 introduced file I/O in addition to character data types. Object Oriented Programming (OOP) is defined as the type of programming where programmers define the type of data structure and the types of operations or functions to be applied to these data structures.
Object oriented programming was popularised by C++ language and has been widely used in the scientific programming field. The use of OOP provided by Fortran 2003 can be emulated in Fortran 90 which gave a great opportunity for scientific programming previously written in Fortran to avoid being re-written in another programming language and still benefit from OOP usage. The modernisation process for a Fortran code includes a large number of edits and modifications on the code in order to convert from one version to the other. In order to optimise the scalability of the code, memory management, overall code performance for the parallel solver code and the serial post-processing code, the following modernisation techniques were applied to the initial F77 FORTRAN code as follows,

- Using implicit none so all variables have to be explicitly defined

- Using modules for global variables instead of using common blocks through the code
- Minimising the use of GO TO statements by replacing them with the proper Do loops or IF statements
- Using array allocation using dynamic memory management for arrays instead of just allocating the arrays directly in the subroutines
- Deallocating array pointers to prevent causing memory leaks
- Generating source code documenting files using Doxygen source codes documentation tool

3.11 Code Validation

The in-house code CHAPSim validation against benchmark data in terms of spatially averaged velocities, r.m.s of fluctuating velocities, Reynolds stresses and r.m.s of fluctuating vorticity at $Re_\tau = 180$ is shown in Figure 3.5. The simulations are compared to the data generated by Kim et al. [20] and validated against Kreplin and Eckelmann [65], Hanaratty et al [66] and Willmarth and Lu [67] and has been widely used across smooth channel simulations literature. Validation of the code at higher Reynolds number and for textured surfaces is available in [18], [17] and [25]. For smooth channel cases, $u^{'}_{rms} = u^{''}_{rms}$ whereas for textured surfaces, $u^{''}_{rms}$ is the r.m.s of spatially-averaged fluctuating velocity and $u^{'}_{rms}$ the r.m.s of phase-averaged fluctuating velocity (this is also applicable for the r.m.s of fluctuating velocities in the wall-normal and spanwise directions).

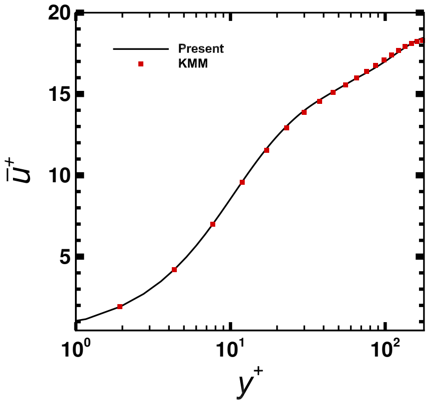

(a) Spatially averaged velocity.

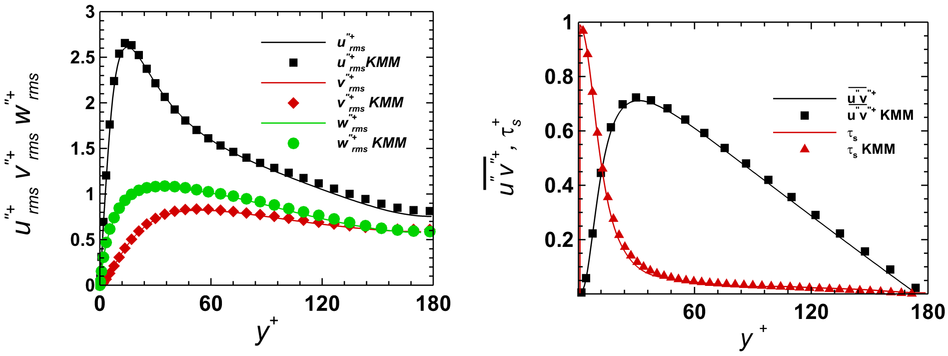

(b) Root mean square fluctuating velocities.

(c) Reynolds shear stress

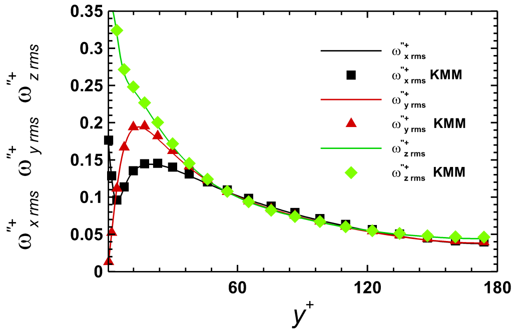

(d) Root mean square vorticity

Figure 3.5: Validation of the DNS in-house code CHAPSim against benchmark data of KMM [20] at $Re_\tau = 180$.

Chapter 4

Implementation of Textured Surfaces in CHAPsim.

This chapter is dedicated to discussing the techniques used for implementing textured surfaces in CHAPSim. Also, presented in this chapter, are discussions on the implementation of the backswimmer geometry, the use of the Immersed Boundary Method (IBM) and the challenges associated with the use of the backswimmer geometry. The simulation procedure adopted in the present code with the textured surface implementation is shown in Figure 4.1.

4.1 Immersed Boundary Method.

The Immersed Boundary Method is a common method to implement 3D geometries. The method is capable of analysing complex geometries and has been widely used in literature as discussed in chapter 2 and shown in Table 2.3. The IBM used in CHAPSim is a method proposed by Leonardi and Orlandi [21] and discussed in detail in Seddighi [18] and Seddighi et al. [25]. The approach is a revised IBM which was initially developed by Faldun et al. [68]. Mainly, the method (i) enforces the flow parameters equal to zero for the points within the roughness elements, (ii) treats the first point away from the wall boundary. This method can efficiently handle complex geometries

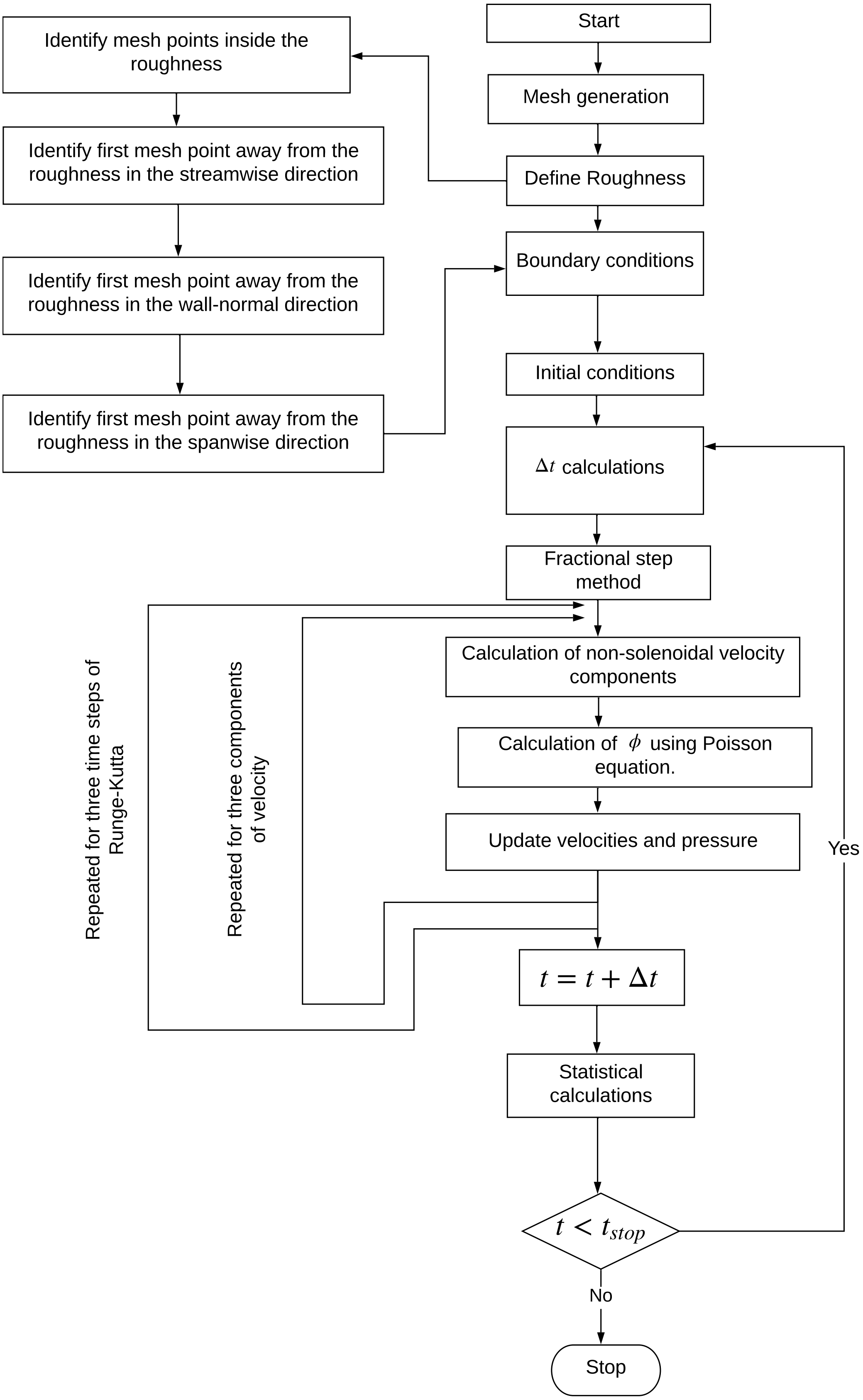

Figure 4.1: Simulation procedure adopted in the present code.

with regular grids by introducing a body force field to allow implementing roughness without using unstructured or multi-block meshes, this reduces the overall simulation time and thus the required simulation cost. As the method aims to identify the first point away from the roughness boundary, this is only done once at the beginning of the simulation hence, no parallelisation is needed which makes it a very affordable method even for fine meshes.
In order to implement a texture geometry to the code, the governing equations for the in-house code should be edited as follows,

$$\frac{\partial u_i^*}{\partial t^*} + u_j^* \frac{\partial u_i^*}{\partial x_j^*} = -\frac{\partial p^*}{\partial x_i^*} + \frac{1}{Re_c} \frac{\partial^2 u_i^*}{\partial x_j^* \partial x_j^*} + \Pi \tag{4.1}$$

$$\frac{\partial u_i^*}{\partial x_i^*} = 0 \tag{4.2}$$

where Π is the pressure gradient required to maintain a constant flow rate [21]. Equation 4.1 is discretised using a second order finite difference approximation. As energy is dissipated due to friction and pressure drag, an external force Π is added to maintain a constant flow rate, Equation 4.1 is solved by integrating the streamwise momentum equation below,

$$\int_V \left(\frac{\partial u_i^*}{\partial t^*} + \frac{\partial u_i^* u_j^*}{\partial x_j^*}\right) dv^* = \int_V -\frac{\partial \overline{p}^*}{\partial x_i^*} + \frac{1}{Re_c} \frac{\partial^2 u_i^*}{\partial x_j^{*2}} \tag{4.3}$$

where V is the volume of the flow domain. Due to the periodicity in the streamwise and spanwise directions and the zero velocity on the channel walls it is found that,

$$\frac{\partial Q^*}{\partial t^*} = \frac{1}{Re_c} \int_V RHS \ . \ dv + \Pi \ . \ V \tag{4.4}$$

where RHS is the right hand side in Equation 4.3, Q^* is the total mass and Π is the constant pressure gradient in Equation 4.1, for the case of flow where $\frac{\partial Q^*}{\partial t*} = 0$, Π is computed as,

$$\Pi = -\frac{1}{V} \frac{1}{Re} \int_V RHS \ . \ dv \tag{4.5}$$

In addition to the change in the governing equations due to the addition of Π, the change in drag calculated by means of total drag is changed compared to smooth channel flow. For the case of smooth channel flow, the wall shear stress is calculated from the spatially averaged velocity profile as shown,

$$\tau_s^* = \frac{1}{Re_c} \frac{\partial \overline{u}^*}{\partial y^*}|_{y=0.0} \tag{4.6}$$

for rough walls, the shear stress contains the contribution of pressure and friction drag. Thus, the wall shear stress is calculated as follows,

$$\tau_r^* = (P_d^* + \tau_f^*) = \frac{\Pi S_e}{L_x} - \tau_s^* \tag{4.7}$$

where S_e is the total flow area. The friction velocity and friction Reynolds number for smooth and textured surfaces are calculated as follows,

$$\begin{aligned} u_{\tau s}^* &= \sqrt{\tau_s^*}\ , Re_{\tau s} = Re_c\ u_{\tau s}^* \\ u_{\tau r}^* &= \sqrt{\tau_r^*}\ , Re_{\tau r} = Re_c\ u_{\tau r}^* \end{aligned} \tag{4.8}$$

The implementation of the texture geometry needs two major steps: (i) treating the roughness and (ii) providing an appropriate value for the pressure gradient. To treat the nodes inside the roughness, the velocity inside the roughness nodes is set equal to the velocity of the roughness. The velocity of the roughness is set to zero as the roughness elements are fixed. No further treatment is required for treating the nodes inside the roughness, only special consideration is required to treat the first point away from the boundary to produce a smoothly varying surface.

4.1.1 Treatment of the First Point Away From the Roughness

The treatment of the first point away from the roughness surface is done by revising the second derivative operator for the first point away from the roughness, taking into account the actual distance between the roughness surface and the numerical mesh point. The pressure and non-linear terms are neglected as they are very small compared to the viscous terms. Figure 4.2 shows a sketch for a roughness and mesh configuration used in IBM where the points within the roughness elements, the roughness wall and the first points away from the roughness wall are marked and the indices are as follows,

- $i-1$ Points on the roughness surface
- i First point away from the wall
- $i+1$ First point away from the roughness

For $i-1$, $u_{i-1}=0$, $\Delta_1 = i-i-1$ and $\Delta_2 = i+1-i$ which is the regular mesh spacing. Using a Taylor series expansion around point u_i, u_{i-1} and u_{i+1} are calculated as follows,

$$u^*_{i+1} = u^*_i + \frac{\partial u^*_i}{\partial x^*_j}\ \Delta_2 + 0.5(\frac{\partial^2 u^*_i}{\partial x^{*2}_j}\ \Delta_2^2) + O(\Delta_2^3) \tag{4.9}$$

$$u^*_{i-1} = u^*_i - \frac{\partial u^*_i}{\partial x^*_j}\ \Delta_1 + 0.5(\frac{\partial^2 u^*_i}{\partial x^{*2}_j}\ \Delta_1^2) + O(\Delta_1^3) \tag{4.10}$$

thus, the first derivatives are calculated as follows,

$$\frac{\partial u^*_i}{\partial x^*_j} = \frac{u^*_{i+1}}{\Delta_2} - \frac{u^*_i}{\Delta_2} - 0.5(\frac{\partial^2 u^*_i}{\partial x^{*2}_j}\ \Delta_2) \tag{4.11}$$

substitute Equation 4.11 into Equation 4.10, u_{i-1} becomes,

$$u^*_{i-1} = u^*_i - u^*_{i+1}\ \frac{\Delta_1}{\Delta_2} + u^*_i\ \frac{\Delta_1}{\Delta_2} + 0.5\ (\frac{\partial^2 u^*_i}{\partial x^{*2}_j}\Delta_1\Delta_2) + 0.5\ (\frac{\partial^2 u^*_i}{\partial x^{*2}_j}\Delta_1^2) \tag{4.12}$$

the second derivatives used in the viscous terms are calculated as follows,

$$\frac{\partial^2 u^*_i}{\partial x^{*2}_j} = (u^*_{i-1} - u^*_i\ (1 + \frac{\Delta_1}{\Delta_2}) + u^*_{i+1}\frac{\Delta_1}{\Delta_2})\ (\frac{2}{\Delta_1\Delta_2 + \Delta_1^2}) \tag{4.13}$$

where,

$$1 + \frac{\Delta_1}{\Delta_2} = \frac{\Delta_1 + \Delta_2}{\Delta_2} \tag{4.14}$$

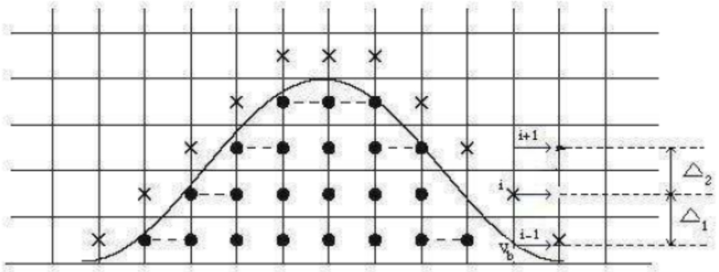

Figure 4.2: Schematic sketch of the roughness nodes identified using IBM where the dots present the points within the roughness, the solid line presents the roughness wall and × presents the first point away from the roughness points [21].

the second derivatives become,

$$\frac{\partial^2 u_i^*}{\partial x_j^{*2}} = \frac{2u_{i-1}^*}{\Delta_1(\Delta_1+\Delta_2)} + \frac{-2u_i^*}{\Delta_1\Delta_2} + \frac{2u_{i+1}^*}{\Delta_2(\Delta_1+\Delta_2)} \tag{4.15}$$

It should be noted that the treatment of the first point away from the roughness direction is done in the streamwise, wall-normal and spanwise directions. Further detail about this method is provided in Leonardi and Orlandi [21].

4.2 Backswimmer Geometry Implementation

The texture used for the simulations is a backswimmer abdomen microstructure geometry. The geometry was provided to the project by Prof. Barthlot [69], University of Bonn. The texture geometry is shown in Figure 4.3 by Mail et al. [22]. The implementation of the Backswimmer geometry is undertaken into CHAPSim. A key challenging issue with the implementation of the backswimmer geometry is the presence of an area below the roughness element. The velocity values are clearly not necessarily zero unlike the other geometries which have been previously implemented in the code, where the change in the velocity components occurs between the roughness elements in the streamwise and spanwise directions only. To set the borders of the boundary points while accurately capturing the geometry, the profile of the backswimmer geometry was digitised and curve fitted using 6^{th} and 10^{th} order polynomial functions for the lower and the upper parts of the texture element

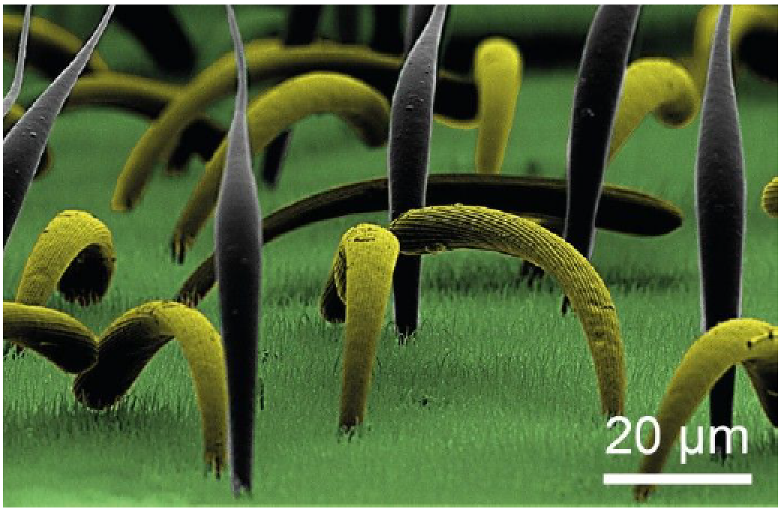

Figure 4.3: The backswimmer abdomen micro-structure [22].

respectively. Three corresponding subroutines to define the boundary points of the texture in the streamwise, spanwise and wall-normal directions are then adopted for the new geometry. The IBM is afterwards applied to the boundary points and the first point away from the geometry. The resulting 2D and 3D implemented computational domain is shown in Figure 4.4.

4.3 Backswimmer Geometry Implementation Challenges

Complexity of the geometry in addition to the required accuracy to obtain a replica for the schematic shown in Figure 4.3 without using excessive computational power was challenging for the backswimmer case. Unlike square or pyramid elements where the geometry borders can be identified using a small number of points due to their uniform shape compared to the Backswimmer texture. Table 4.1 shows a comparison for the simulation parameters used to define the texture between the Backswimmer and the pyramid in Seddighi et al. [25] at a low Reynolds number $Re = 2800$. It is noticed from Table 4.1 that for the case of the backswimmer geometry, a significant increase in the number of roughness points for each texture element is required in the

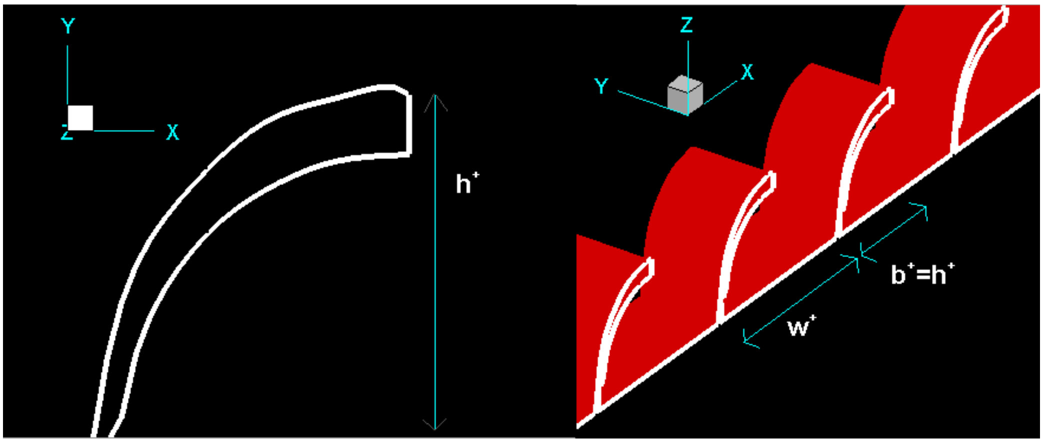

Figure 4.4: Backswimmers' micro-structure textured surface. h^+, b^+, w^+ are the height, width and spacing between the texture elements in the streamwise direction in wall units defined in chapter 5 and chapter 6.

Table 4.1: Details of mesh and domain sizes for backswimmer cases used in the present study and those used in Seddighi et al. [25]. N_x, N_y, N_z are the number of mesh points in the streamwise, wall-normal, and spanwise directions, N_1, N_2, N_3 are the number of roughness points in the streamwise, wall-normal, and spanwise directions, respectively.

Parameter	Backswimmer	Pyramid
Re	2800	2800
N_x	1800	1024
N_y	300	240
N_z	300	720
N_1	50	32
N_2	32	24
N_3	10	32
L_x	7.2	12.6
L_z	1.5	4.50
Δx^+	0.72	2.214
Δz^+	0.9	1.1250

streamwise and wall-normal directions which also yields a significant increase in the number of mesh cells used throughout the simulations even though the computational domain in both directions is smaller than that of the pyramid case. These parameters were used for all the simulated test cases to define the geometry and its corresponding computational domain.

Chapter 5

Backswimmer Turbulent Flow at Different Geometry Conditions

This chapter presents results for cases where the backswimmer geometry details change but the bulk velocity remains unchanged. The corresponding turbulence statistics and flow structures are studied. The changes in geometry are in the form of changing the number of roughness elements in the streamwise and spanwise directions. All the presented test cases in this chapter are at Reynolds number $Re = 2800$. The simulations are compared to smooth channel flow at the same Reynolds number.

The comparisons are in terms of the change in the spatially-averaged velocity, root-mean-squared of fluctuating velocity, root-mean-squared of fluctuating vorticity, Reynolds shear stress and quadrant analysis. All presented statistics are shown for the whole channel and around the roughness element. Flow structures are also shown and the differences in the flow topologies are highlighted using visualisation of instantaneous fluctuating velocities and vortex structure using λ_2 criterion by Jeong and Hussain [6] for the computational domain and around one roughness element.

5.1 Simulation Parameters

To study the effect of changing the number of roughness elements in the streamwise and spanwise directions, three cases were simulated and compared to smooth channel flow as well as each other. All the test cases parameters are shown in Table 5.1.

It should be noted that all the simulations are at the same Reynolds number $Re = 2800$. The notation of the presented cases is based on the number of roughness elements in the streamwise and spanwise directions, respectively, for example; BS1810 denotes 18 elements in the streamwise direction and 10 elements in the spanwise direction. The computational domain and corresponding mesh sizes are consistent with the minimal dimensions used in Chung et al. [70], which proved that flows simulated in minimal-span channels are sufficient to capture the flow behaviour and turbulence characteristics similar to full-span channels for smooth and rough channel flows. To use the minimal-span channels the following criteria must be met in terms of the channel spanwise direction denoted by H_z,

- $H_z/\delta > 100/Re_\tau$, the span must be wide enough to accommodate near wall streaks.
- $H_z/\delta > h/0.4$, the span must be wide enough to immerse the roughness in unconfined wall turbulence.
- $H_z/\delta > \lambda_y$, the minimal span must be wide enough to capture the widest features of roughness.

The Data shown in Table 5.1 is consistent with the previously proposed criteria. The minimal-span length and width are verified using fluctuating velocity two-point correlation in the streamwise and spanwise directions for all test cases. For the instantaneous flow fields, time integral tests were applied and all the captured contour and iso-surface plots were extracted with $\Delta t^+ \approx 100$ apart. It should be noted that BS3610 is equivalent to BS2800 discussed in detail in chapter 6.

Table 5.1: Details of simulated test cases where S denotes smooth ($Re_\tau = Re_{\tau s}$), BS denotes backswimmer ($Re_\tau = Re_{\tau r}$), w_x/h and w_z/h are the width-to-height ratios in the streamwise and spanwise directions, respectively.

Case	Re_τ	M	N	w_x/h	w_z/h	h^+	H_x^+	H_z^+	N_x	N_y	N_z	u_τ	τ	$DR\%$
S00	177.8	0	0	0	0	0.0	1280	267	1800	300	300	0.0508	0.00258	N/A
BS1810	186.0	18	10	1	2.0	5.6	1339	279	1800	300	300	0.0531	0.00281	-9.26
BS3210	182.5	32	10	0.125	2.0	5.5	1369	274	1800	300	300	0.0521	0.00271	-5.18
BS3215	182.8	32	15	0.125	1.0	5.5	1316	274	1800	300	300	0.0522	0.00272	-5.59
BS3610	178.7	36	10	0.0	2.0	5.4	1286	268	1800	300	300	0.0510	0.00260	-0.78

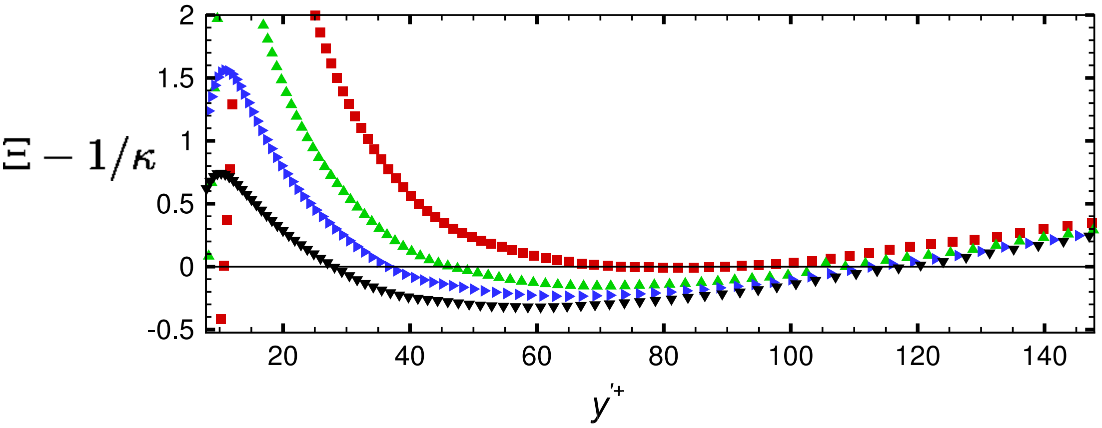

Figure 5.1: Diagnostic function for origin detection for BS7400. $\epsilon = 0.01$ (▼), $\epsilon = 0.015$ (▶), $\epsilon = 0.020$ (▲) and $\epsilon = 0.025$ (■)

5.2 Detection of Origin

Following Breugem et al. [71] the extent of the logarithmic layer can be determined using the diagnostic function $\Xi = y'^{+}(d\overline{u}^{+}/dy'^{+})$ where $y'^{+} = (y + \epsilon)^{+}$ and ϵ is the distance which the origin is shifted. For the region where the log-law is satisfied the value of the diagnostic function must be constant and equal to $1/\kappa$ where κ is the von-Karman constant obtained from the smooth channel simulations as $\kappa = 0.40$. It should be noted that for Reynolds number $Re = 2800$, the log-law region is not clear and hence the highest Reynolds number case was used ($Re = 7400$) to calculate the shift distance for all the results presented as shown in Figure 5.1 at different values of ϵ. The value of the diagnostic function is equal to zero at $\epsilon = 0.025$. Therefore, all the presented results in this chapter and chapter 6 will be shifted by 0.025.

5.3 Drag Reduction

The drag reduction is calculated by means of the change in the total shear stress, taking into account the roughness effect. The drag reduction for all

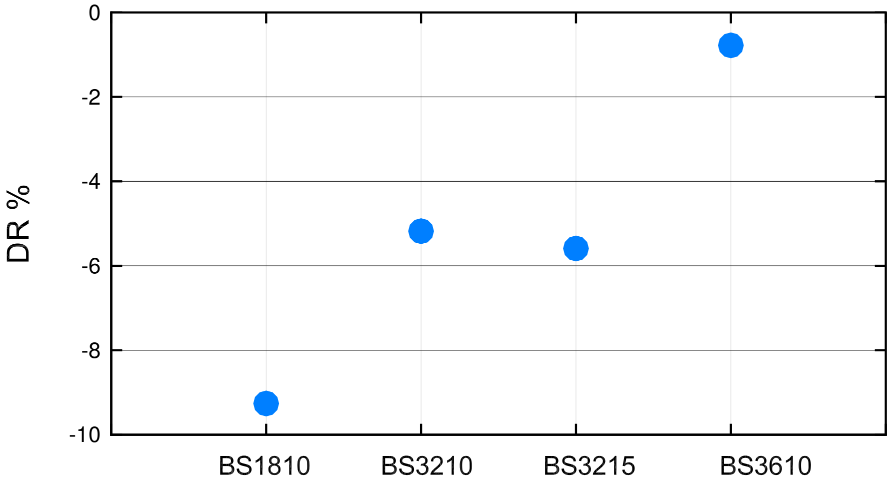

Figure 5.2: Drag reduction for BS1810, BS3210 and BS3215 cases.

test cases is calculated as,

$$DR = \frac{\tau_s - \tau_r}{\tau_s} \tag{5.1}$$

where DR represents drag reduction. Positive DR indicates drag reduction whereas negative DR indicates drag increase, τ_s and τ_r are the smooth and rough textured surface total shear stress, respectively. The time averaged friction velocity, friction Reynolds number and total shear stress are shown in Table 5.1. The DR for all backswimmer cases is shown in Figure 5.2. Compared to S00, all backswimmer cases exhibit an increase in the drag. BS1810 has the most drag increase equal to $DR = -9.26\%$. As the number of roughness elements in the streamwise direction increases the DR value is reduced by 44% compared to BS1810. However, as the number of roughness elements increases in the spanwise direction for BS3215, this results in a drag increase compared to BS3210 by 7.9%.

5.4 Spatially-Averaged Velocity

The spatially-averaged velocity profiles for the backswimmer cases compared to S00 are shown in Figure 5.3. For all backswimmer cases, the velocity

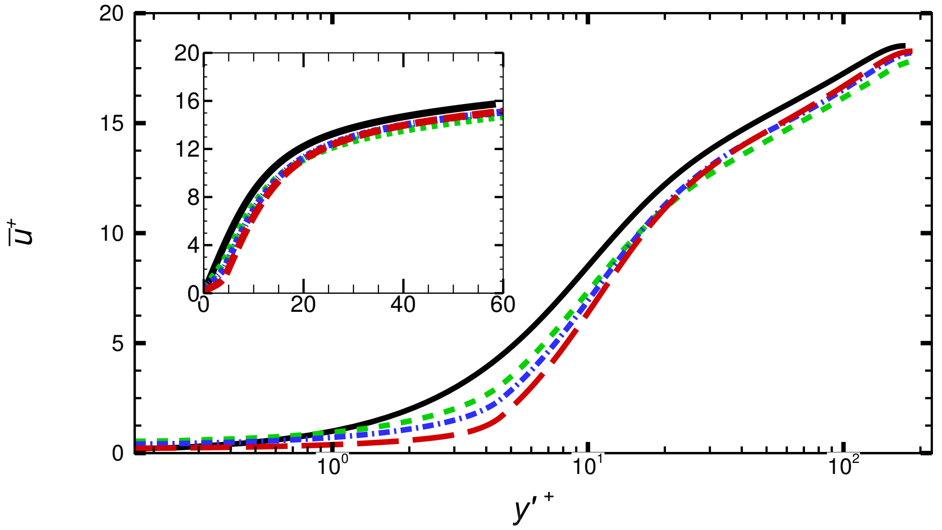

Figure 5.3: Spatially-averaged velocity profiles for S00 (—), BS1810 (- -), BS3210 (-·-·-·-) and BS3215 (— —).

profile decreases compared to S00. This is due to the increase in the wall shear velocity. The maximum downward shift in the log-region of the profile occurs for BS1810. Both BS3210 and BS3215 velocity profiles are similar to S00 specially in the log-region.

5.4.1 Spatially-Averaged Velocity Logarithmic Distribution

The logarithmic distribution for the spatially-averaged velocity profile is a key parameter to characterise textured surfaces. It is also a way to calculate and verify the values of ΔU^+ used to calculate the effective roughness height (see chapter 6). For the smooth channel flow the logarithmic velocity distribution is defined as follows,

$$\overline{u}^+ = 1/\kappa \ln y^+ + A \tag{5.2}$$

where κ is the Von-Karman constant equal to $\kappa \approx 0.40$ and A is the smooth wall log-law intercept equal to $A = 5.39$ obtained from the smooth wall simulations. For the case of the backswimmer textured surface, Equation 5.2

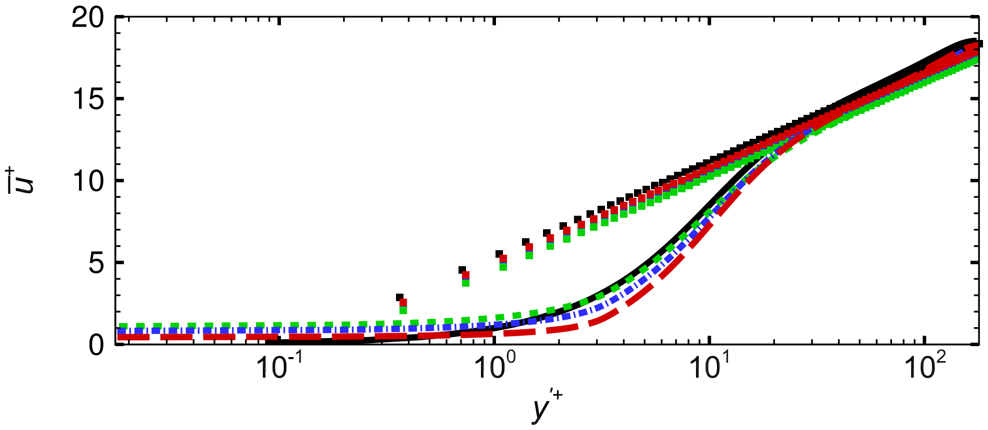

Figure 5.4: Spatially-averaged velocity logarithmic distribution for S00 (—), BS1810 (- -), BS3210 (-·-·-·-) and BS3215 (— —).

becomes [15],

$$\overline{u}^+ = 1/\kappa \ln y'^+ + A - B \tag{5.3}$$

where y'^+ is the shifted wall-normal distance defined earlier, B is the log-law intercept displacement for the textured surface equal to ΔU^+. The logarithmic distribution region for each backswimmer case is shown in Figure 5.4 and the corresponding equations are as follows,

BS1810

$$\overline{u}^+ = 1/\kappa \ln y^+ + 5.39 - 1 \tag{5.4}$$

BS3210

$$\overline{u}^+ = 1/\kappa \ln y^+ + 5.39 - 0.55 \tag{5.5}$$

BS3215

$$\overline{u}^+ = 1/\kappa \ln y^+ + 5.39 - 0.50 \tag{5.6}$$

The value of ΔU^+ is significantly affected by the increase in the number of roughness elements in the streamwise direction. The values of ΔU^+ are also used to determine the effective roughness height (see chapter 6).

5.5 Fluctuating Velocity

The change in the root-mean-square of fluctuating velocities for backswimmer test cases compared to smooth channel flow for the streamwise, wall-normal and spanwise directions is shown in Figures 5.5, 5.6 and 5.7.

The change in the streamwise fluctuating velocity is shown in Figure 5.5. For BS1810 compared to S00, the profile slightly decreases for $y'^{+} < 20$ while for $y'^{+} > 20$ the profile increases. As the number of roughness elements increases in BS3210 the profile increases for $y'^{+} < 20$ whereas for $y'^{+} > 20$, the profile decreases and becomes similar to the S00 case. As the number of roughness elements in the spanwise direction increases, BS3215 has the highest profile for $y'^{+} < 20$ while for $y'^{+} > 20$ the profile is similar to BS3210. Plotted against y'/δ, all backswimmer profile peaks are in the same location, the maximum velocity for all cases is less than S00. Overall, backswimmer geometry effect on u''^{+}_{rms} is the least significant compared to the wall-normal and spanwise fluctuating velocities.

The change in the wall-normal fluctuating velocity is shown in Figure 5.6. All backswimmer cases fluctuating velocity profiles increase compared to S00. BS3210 and BS3215 have the highest profile for $y'^{+} < 30$ followed by BS1810. For $y'^{+} > 30$, BS3215 profile decreases while BS3210 and BS1810 profiles remain similar to S00. Plotted against y'/δ, the location of the profile peak is affected by the increase in the number of roughness elements in the streamwise direction where the peak of profile is shifted further from the roughness base.

The change in the spanwise fluctuating velocity is shown in Figure 5.7. All backswimmer cases exhibit an increase in the profile compared to S00. BS3210 exhibits the highest profile compared to S00 and BS3215. For $y'^{+} > 30$, BS1810, BS3210 and BS3215 profiles are similar to each other but slightly higher than S00. Unlike the wall-normal velocity component, plotted against y'/δ, The location of the profile peak is affected by the increase in the number of roughness elements in the spanwise direction where the peak is shifted away from the roughness base as the number of roughness elements increases in the spanwise direction.

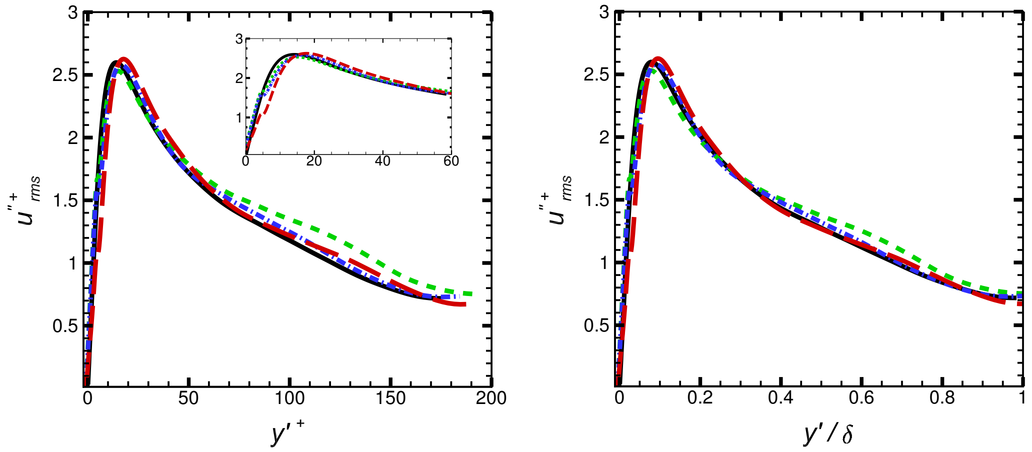

(a) (b)

Figure 5.5: Spatially-averaged r.m.s of streamwise fluctuating velocity for S00 (—), BS1810 (- -), BS3210 (-·-·-·-) and BS3215 (— —). The distance from the wall in (a) wall coordinates: y'^{+} (b) global coordinates: y'/δ.

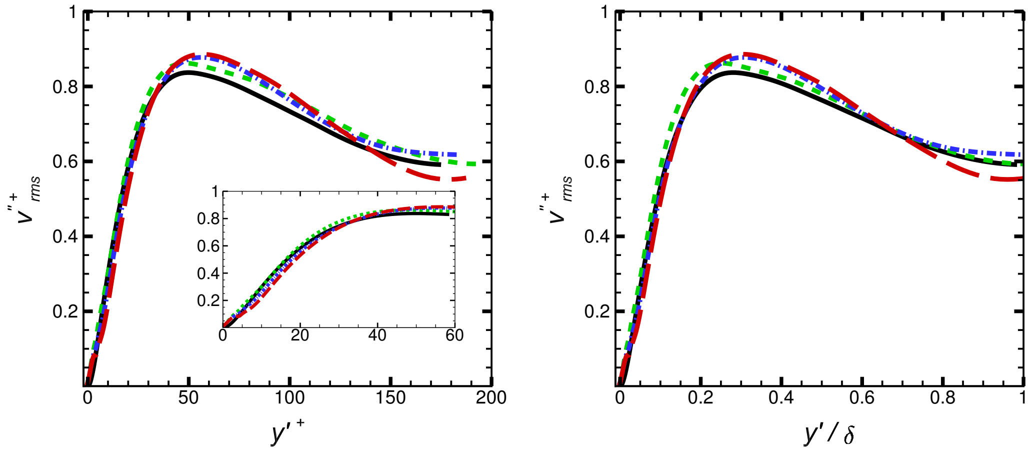

(a) (b)

Figure 5.6: Spatially-averaged r.m.s of wall-normal fluctuating velocity for S00 (—), BS1810 (- -), BS3210 (-·-·-·-) and BS3215 (— —). The distance from the wall in (a) wall coordinates: y'^{+} (b) global coordinates: y'/δ.

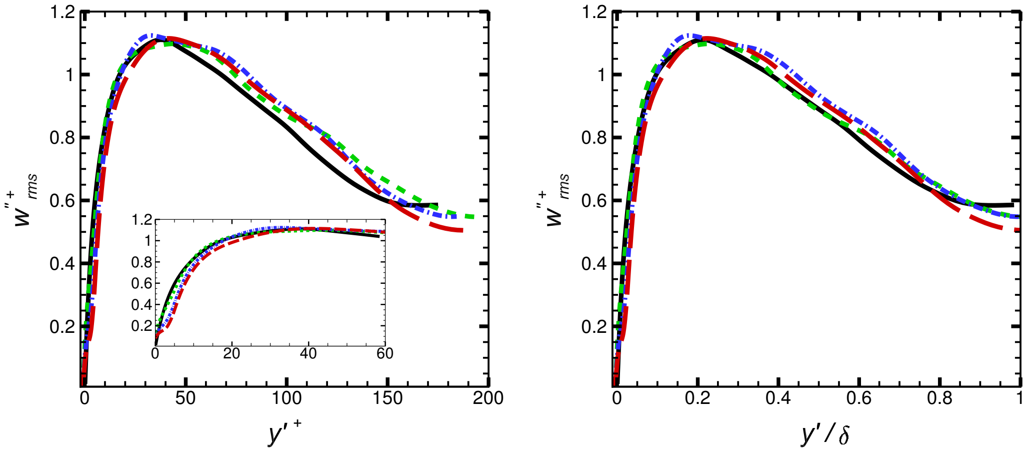

(a) (b)

Figure 5.7: Spatially-averaged r.m.s of spanwise fluctuating velocity for S00 (—), BS1810 (- -), BS3210 (-·-·-·-) and BS3215 (— —). The distance from the wall in (a) wall coordinates: y'^{+} (b) global coordinates: y'/δ.

5.5.1 Fluctuating Velocity Contours

Instantaneous velocity contours u'^{+} (based on phase-averaged velocity) and v^{+} associated with textured surface flows are used to investigate how these changes in the geometry of the arrays of textured surface alter the flow behaviour. This is studied at different conditions in terms of the velocity distribution, streaks alignment with respect to the textured surfaces and the occurrence of ejection and sweep events around the roughness elements [38]. The streamwise fluctuating velocity contours u'^{+} and wall-normal velocity v^{+}, for all backswimmer test cases are shown in this section. The slices are within the roughness height up until the roughness crest and within the roughness crest in the x-y and x-z planes. The contours are presented at three time instants each with $\Delta t^{+} \approx 100$, all have been taken once the flow reached fully developed condition.

Figures 5.8 - 5.10 show contour plots in the x-y plane. For BS1810 the velocity contour around one roughness element is shown in Figure 5.8. Within the roughness element in the wall-normal direction a region of positive velocity is noticed. Also, beyond the roughness crest in the wall-normal direction the

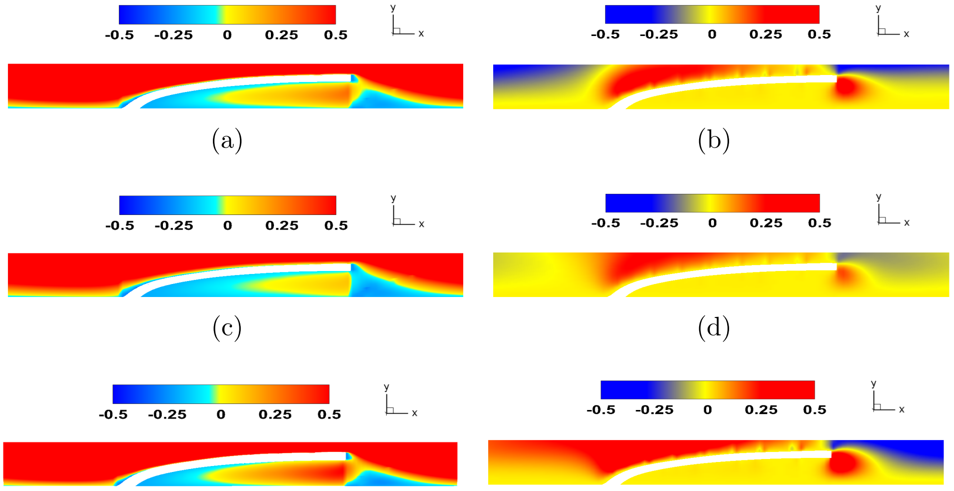

(a) (b)

(c) (d)

(e) (f)

Figure 5.8: Fluctuating streamwise velocity u'^+ (a,c,e) and v^+ (b,d,f) contours for BS1810 at three time instants each with $\Delta t^+ \approx 100$ for one roughness element.

positive velocity component is dominant compared to the negative velocity (in blue). In terms of v^+ within the roughness element the velocity is close to zero and the maximum positive wall-normal velocity is just above the roughness crest.

As the number of roughness elements increases in the streamwise direction BS3210 shown in Figure 5.9, within the roughness element u'^+ tend to decrease and a negative velocity region is noticed compared to BS1810. For v^+, the increase in the number of roughness elements in the streamwise direction is not significant in terms of the velocity distribution however, the velocity magnitudes decrease specially at the roughness crest compared to BS1810. As the number of roughness elements increases in the spanwise direction BS3215 shown in Figure 5.10, u'^+ and v^+ velocity contours exhibit a behaviour similar to BS3210.

For $y/\delta < 0.025$ which is from the roughness base until the roughness crest, u'^+ velocity contours are shown in Figures 5.11-5.13 For BS1810, the high positive velocity region is entrapped between the roughness base and the backswimmer lower surface. As the number of roughness elements increases in the streamwise (Figure 5.12) and spanwise (Figure 5.13) directions the

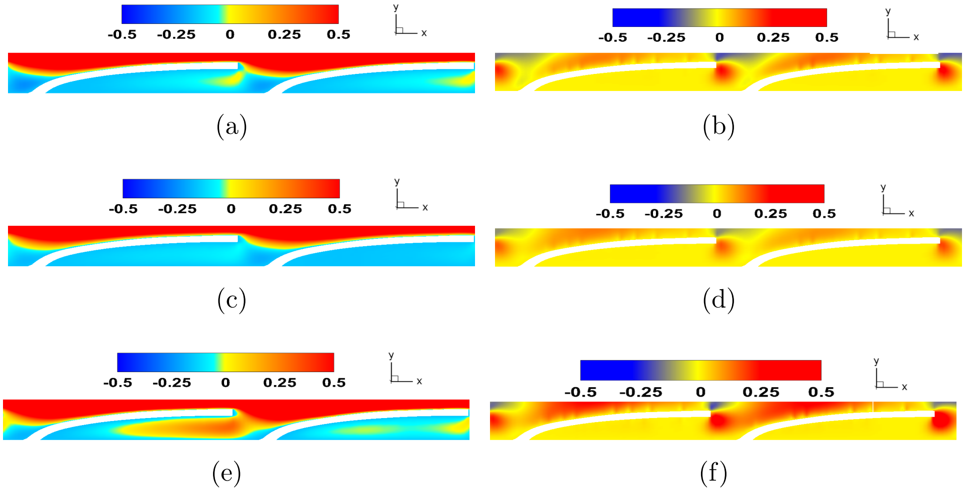

(a) (b)

(c) (d)

(e) (f)

Figure 5.9: Fluctuating streamwise velocity u'^+ (a,c,e) and v^+ (b,d,f) contours for BS3210 at three time instants each with $\Delta t^+ \approx 100$ for one roughness element.

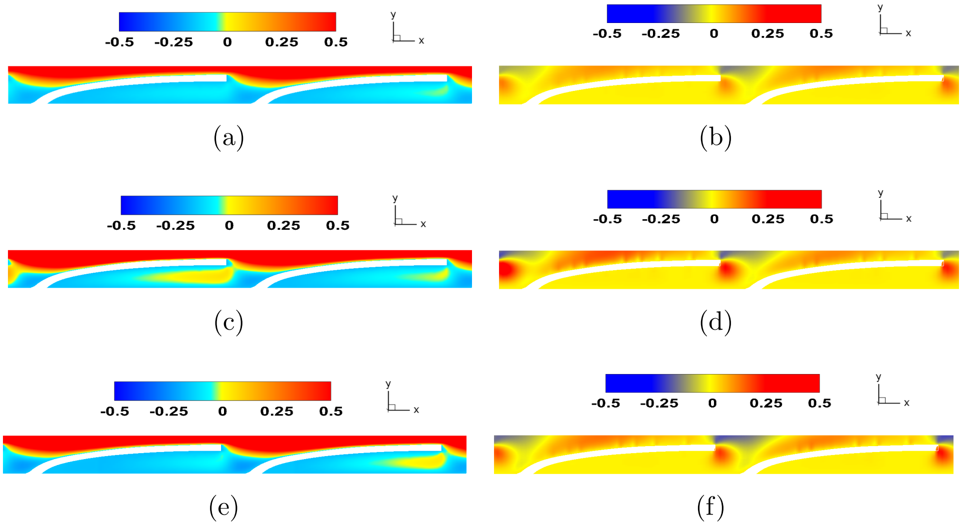

(a) (b)

(c) (d)

(e) (f)

Figure 5.10: Fluctuating streamwise velocity u'^+ (a,c,e) and v^+ (b,d,f) contours for BS3215 at three time instants each with $\Delta t^+ \approx 100$ for one roughness element.

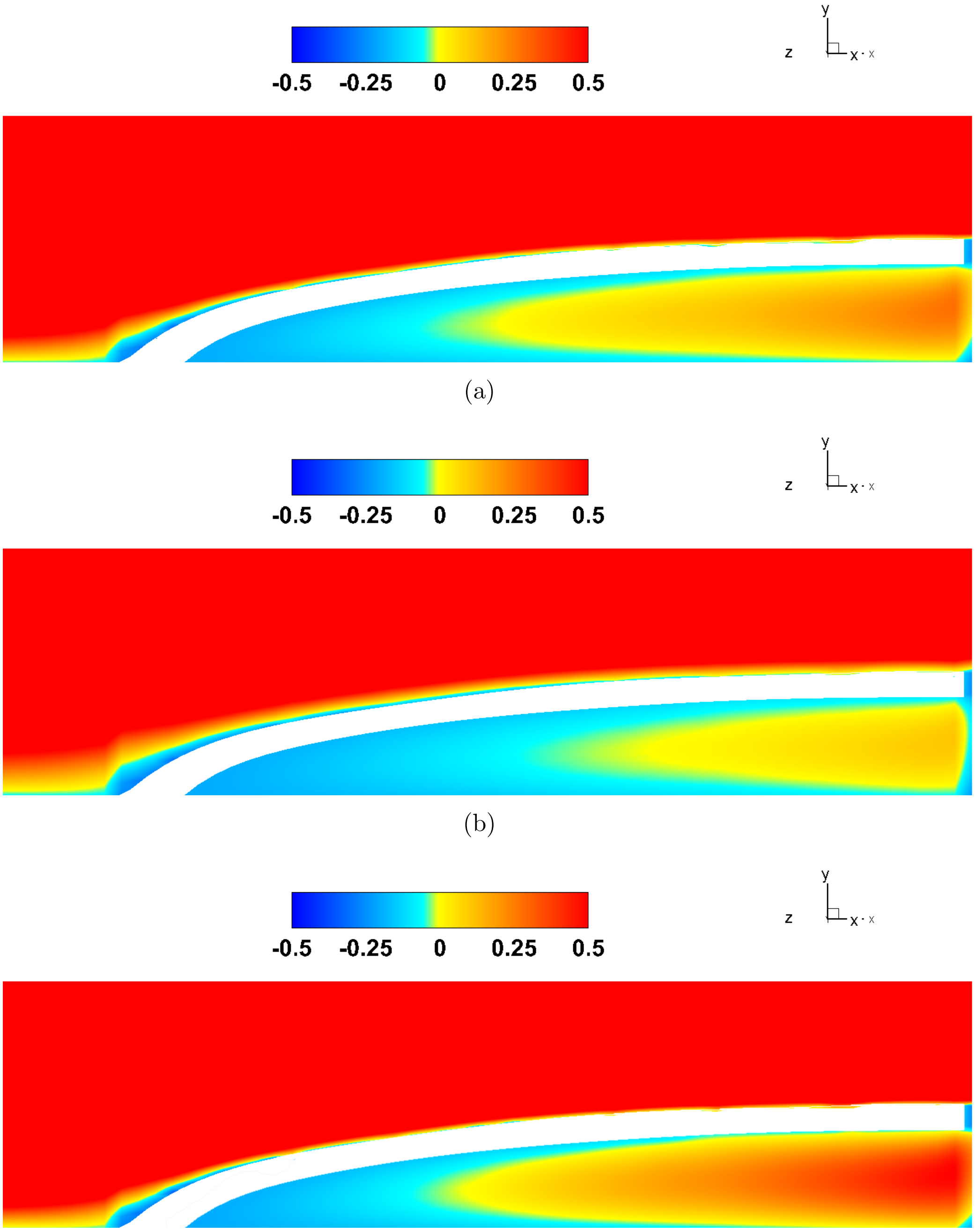

(a)

(b)

(c)

Figure 5.11: Fluctuating streamwise velocity contours u'^{+} for the region within the roughness height at three time instants each with $\Delta t^{+} \approx 100$ for BS1810.

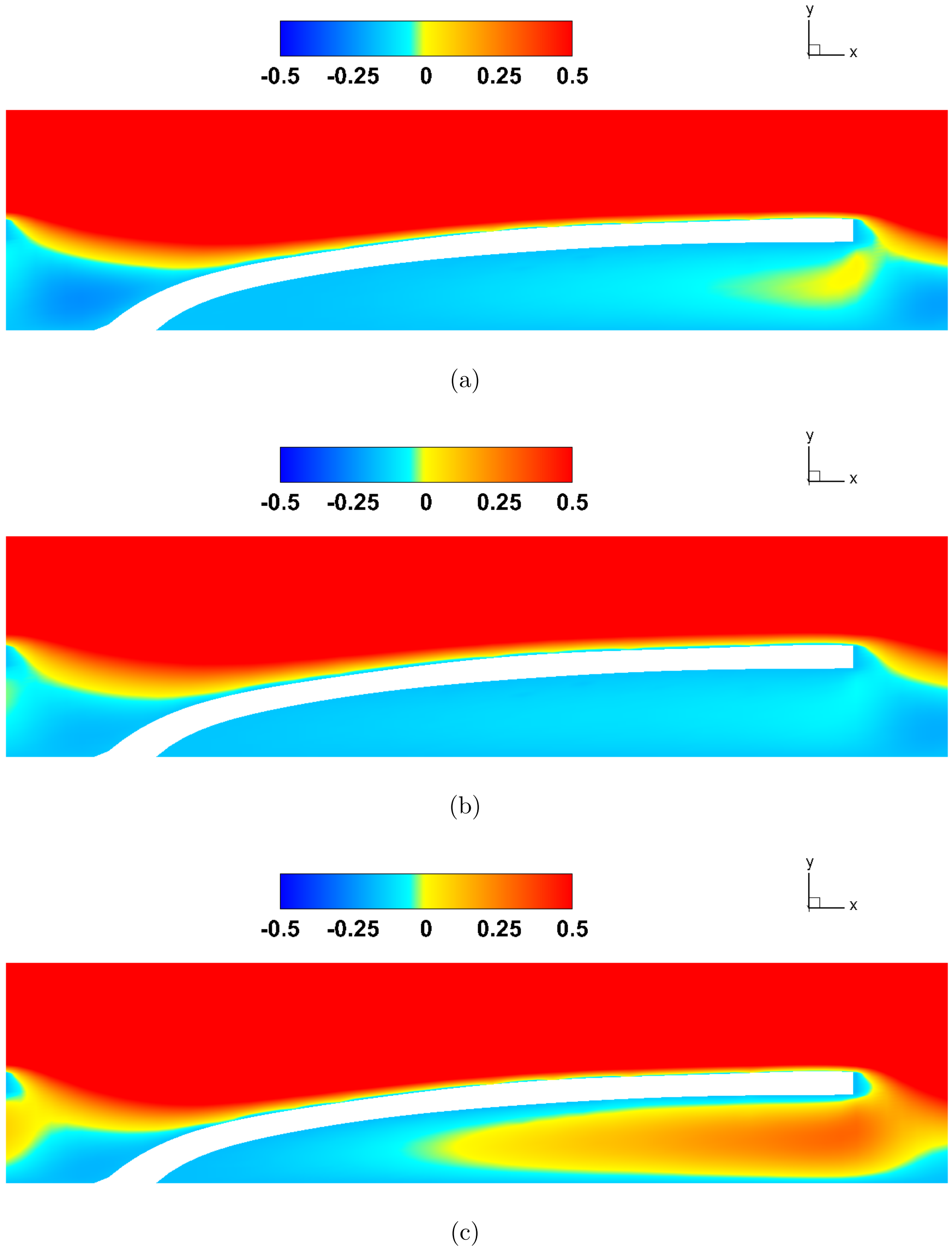

Figure 5.12: Fluctuating streamwise velocity contours u'^{+} for the region within the roughness height at three time instants each with $\Delta t^{+} \approx 100$ for BS3210.

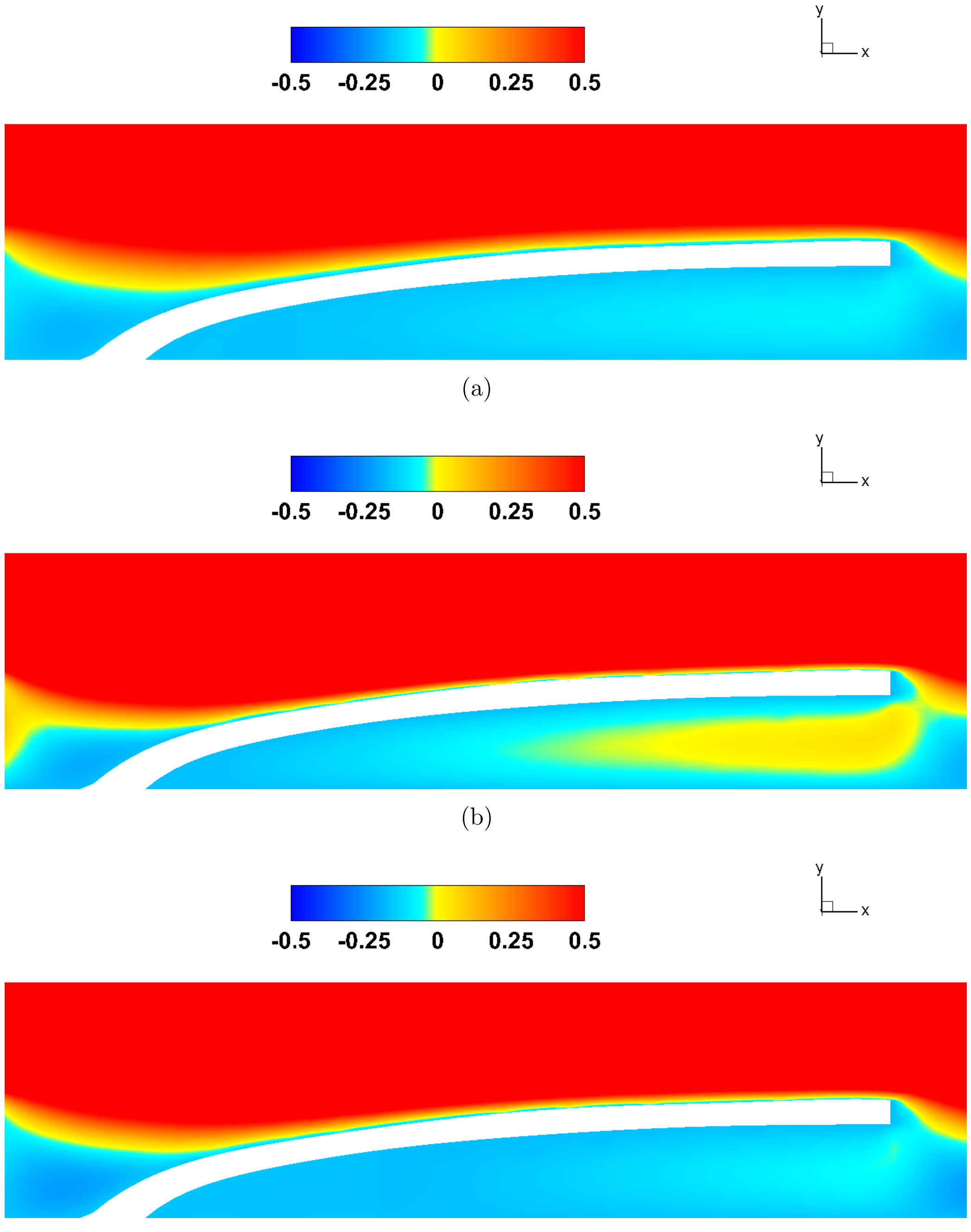

(a)

(b)

(c)

Figure 5.13: Fluctuating streamwise velocity contours u'^{+} for the region within the roughness height at three time instants each with $\Delta t^{+} \approx 100$ for BS3215.

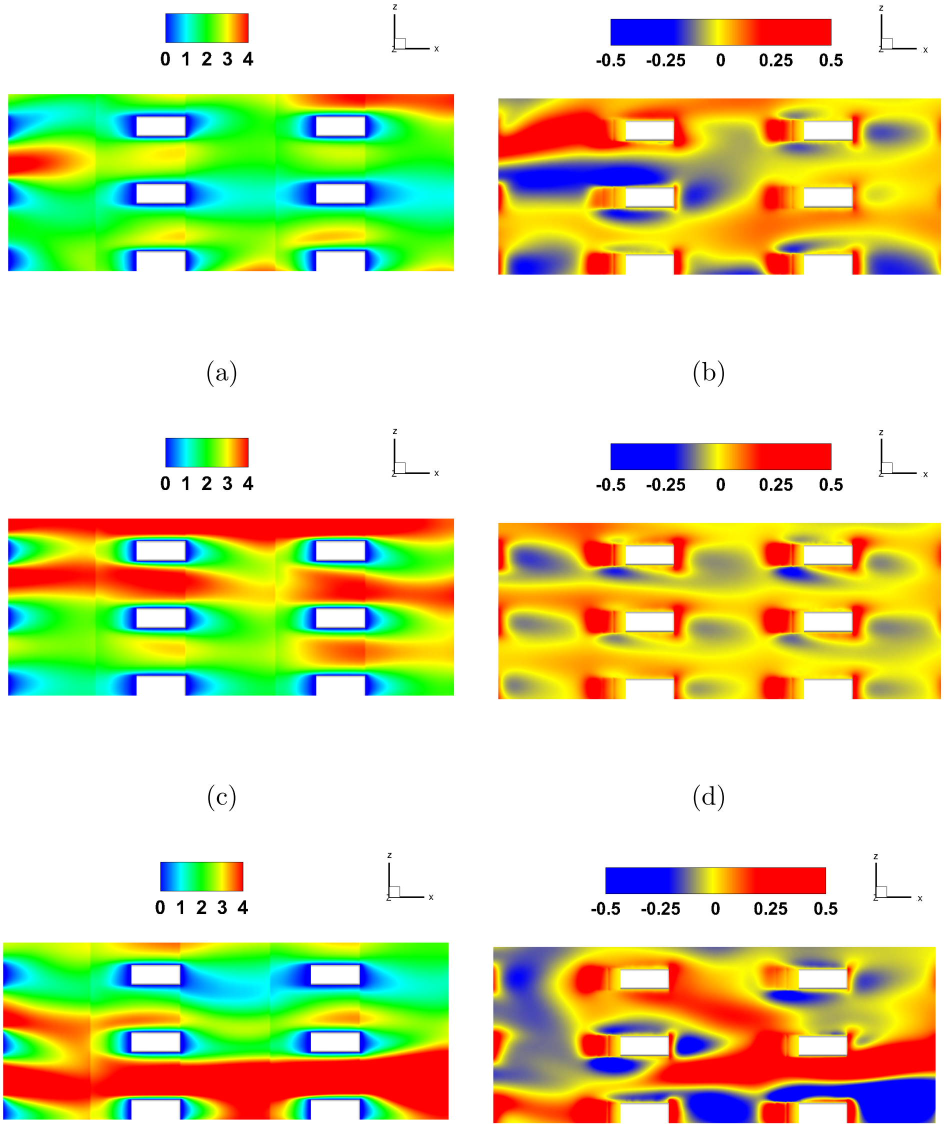

(a) (b)

(c) (d)

(e) (f)

Figure 5.14: Fluctuating streamwise velocity contours u'^{+} (a,c,e) and v^{+} (b,d,f) in the x-z plane for BS1810 below roughness crest ($y/\delta = 0.025$) at three time instants each with $\Delta t^{+} \approx 100$.

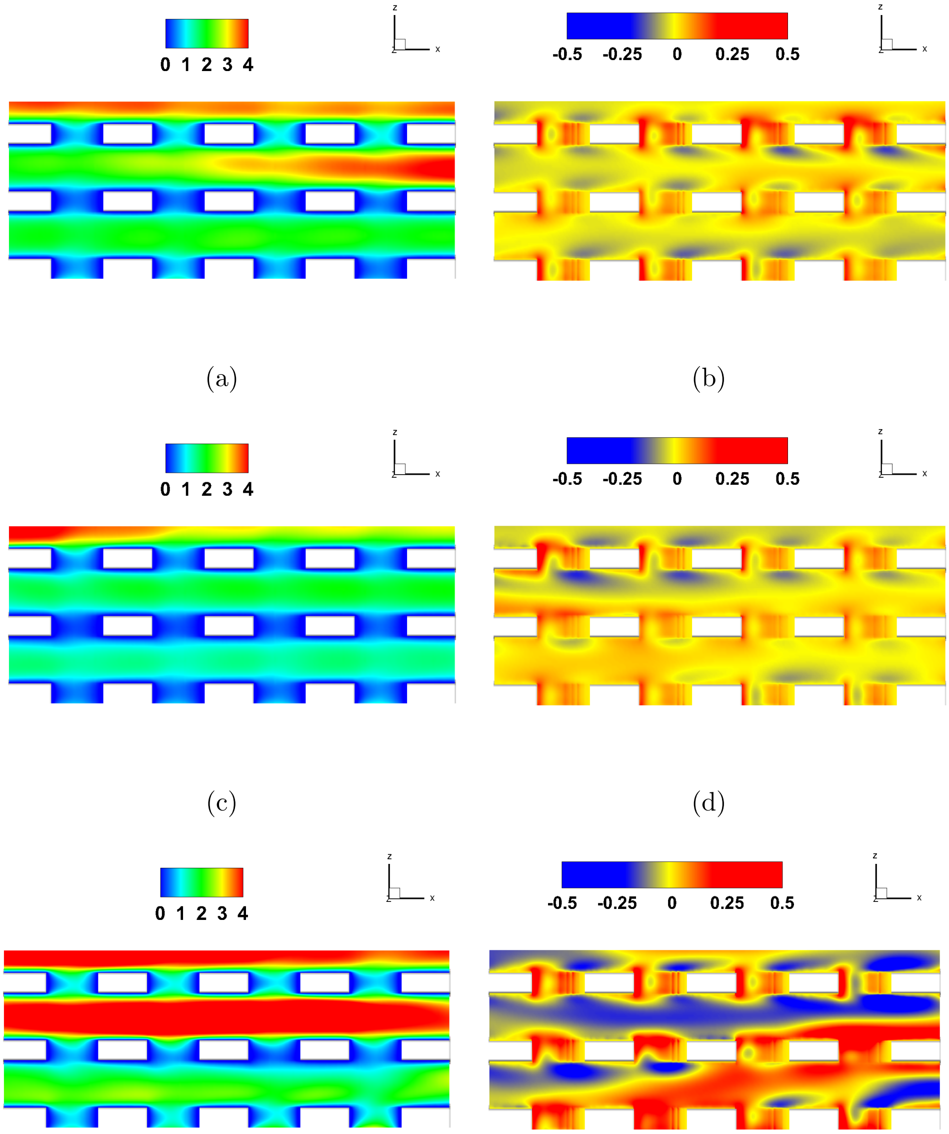

(a) (b)

(c) (d)

(e) (f)

Figure 5.15: Fluctuating streamwise velocity contours $u^{'+}$ (a,c,e) and v^+ (b,d,f) in the x-z plane for BS3210 below roughness crest ($y/\delta = 0.025$) at three time instants each with $\Delta t^+ \approx 100$.

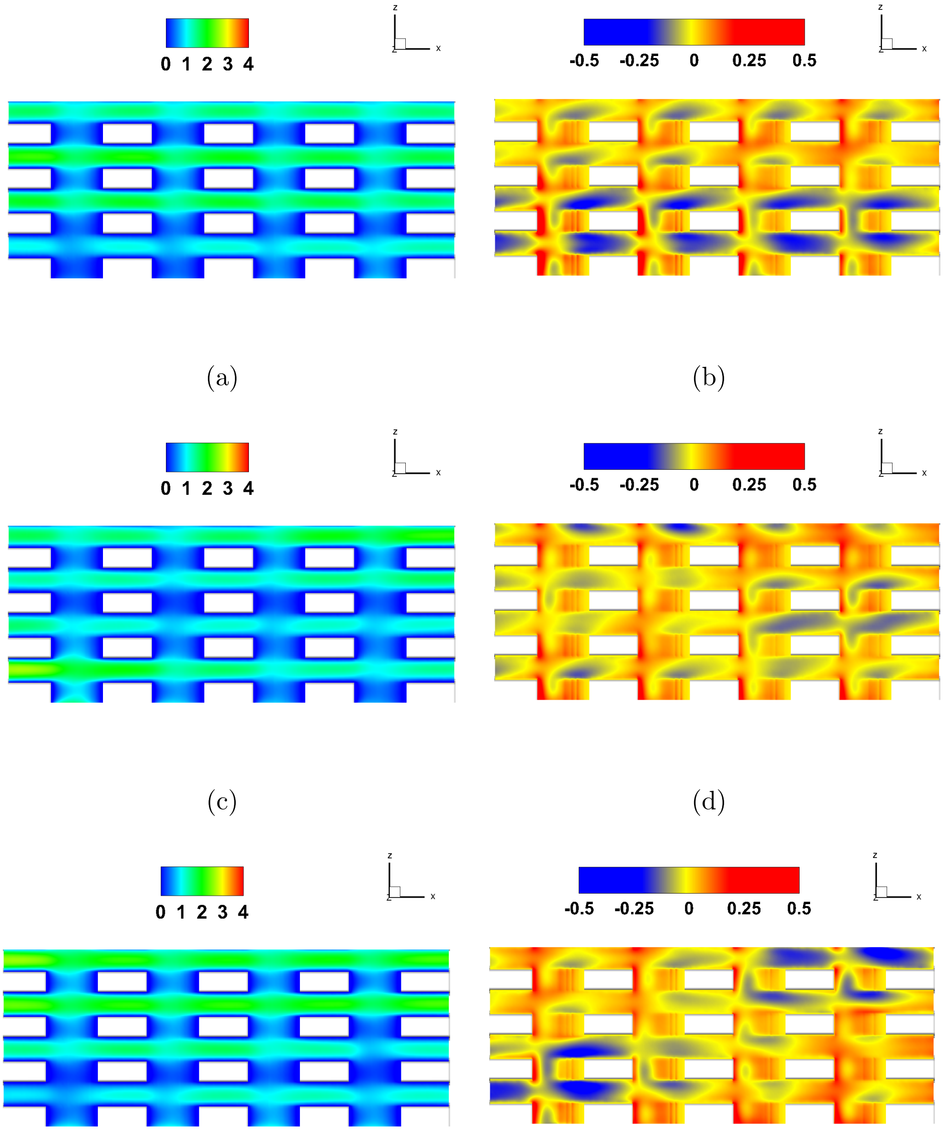

(a) (b)

(c) (d)

(e) (f)

Figure 5.16: Fluctuating streamwise velocity contours u'^{+} (a,c,e) and v^{+} (b,d,f) in the x-z plane for BS3215 below roughness crest ($y/\delta = 0.025$) at three time instants each with $\Delta t^{+} \approx 100$.

positive velocity region decreases and the negative velocity region increases compared to BS1810 where the positive velocity is dominant within and around the roughness element.

Figures 5.14 - 5.16 show contour plots of $u^{'+}$ and v^{+} for all cases at $y/\delta = 0.025$. For BS1810 (Figure 5.14) the width of the velocity streaks is larger than that of BS3210 and BS3215. Also, it is noticed that the distribution of the negative and positive velocity streaks tend to be non-uniform across the channel with respect to the roughness elements position specially for v^{+} in the streamwise and spanwise directions. For BS3210 (Figure 5.15) the distribution of the $u^{'+}$ and v^{+} velocity is more uniform compared to BS1810. The negative velocity is found entrapped within the roughness elements region and the positive velocity components are found in the region between the roughness elements in the spanwise direction for $u^{'+}$. For v^{+}, the positive velocity is entrapped within the roughness elements whereas the negative velocity is between the roughness elements in the spanwise direction.

BS3215 is shown in Figure 5.16. Compared to BS1810 and BS3210, the uniform distribution of $u^{'+}$ in the streamwise and spanwise directions is maintained compared to BS1810 and BS3210. The width of the positive and negative velocity streaks reduces. Also the magnitude of the positive velocity decreases compared to BS1810 and BS3210. In terms of v^{+}, BS3215 has the most uniform velocity distribution compared against BS1810 and BS3210, the width of the negative velocity streaks is reduced however, the change in the velocity magnitude is insignificant compared against BS1810 and BS3210.

5.6 Reynolds Shear Stress

The Reynolds shear stress for backswimmer cases compared to smooth channel flow is shown in Figure 5.17. For $y^{'+} < 20$, all the test cases' profiles are similar to the S00 case whereas for $y^{'+} > 20$ the backswimmer cases exhibit an increase in the profile. BS3215 has the highest profile where the lowest profile is noticed for BS3210. The change in the Reynolds shear stress profiles is consistent with the obtained drag performance. Plotted against

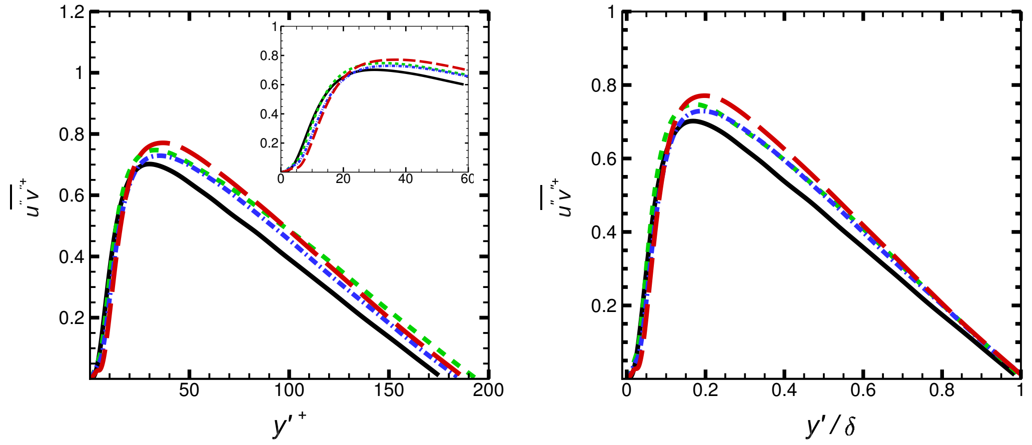

(a) (b)

Figure 5.17: Spatially-averaged Reynolds shear stress for S00 (—), BS1810 (- -), BS3210 (-·-·-·-) and BS3215 (— —). The distance from the wall in (a) wall coordinates: y'^+ (b) global coordinates: y'/δ.

y'/δ, from the texture base up until the profile peak, all backswimmer cases profiles are similar to S00. The peak of the profile is affected by the change in the number of roughness elements in the streamwise direction. As the number of elements in the streamwise direction increases the peak is shifted further from the roughness base. As the number of roughness elements in the spanwise direction increases, the profile magnitude increases.

5.7 R.M.S of Vorticity Profiles

The r.m.s of vorticity profiles compared against smooth channel flow for all backswimmer cases in the streamwise, wall-normal and spanwise directions are shown in Figures 5.18, 5.19 and 5.20. The effect of the textured surfaces compared to smooth channel flow can be divided into two parts: the region within the roughness element and the region beyond the roughness element. Compared to S00, the r.m.s of fluctuating streamwise vorticity (Figure 5.18) profile for all backswimmer cases increases for $y'/\delta < 0.03$. Beyond the roughness crest, the vorticity profiles gradually decrease. The changes in the

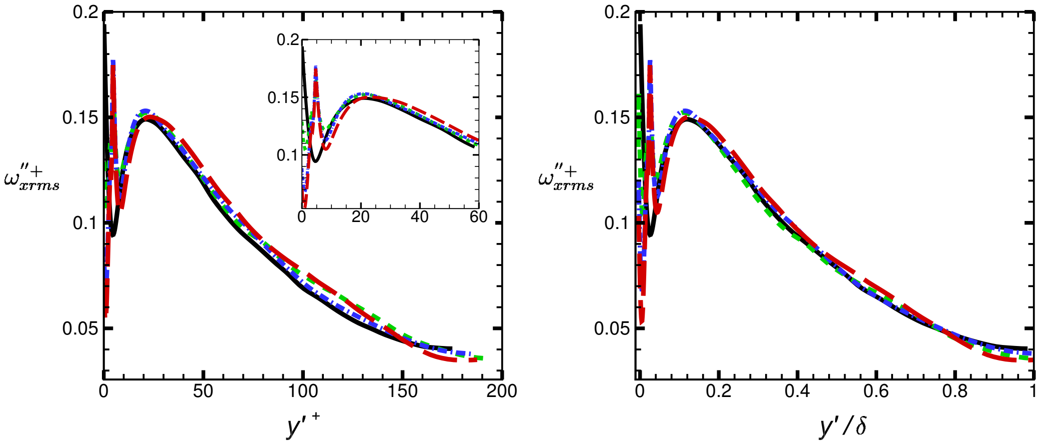

(a)

(b)

Figure 5.18: Spatially-averaged r.m.s of streamwise fluctuating vorticity for S00 (—), BS1810 (- -), BS3210 (-·-·-·-) and BS3215 (— —). The distance from the wall in (a) wall coordinates: y'^{+} (b) global coordinates: y'/δ.

vorticity profiles are not significantly affected by the change in the number of elements either in the streamwise or the spanwise directions.

In the wall-normal direction (Figure 5.19), the r.m.s of fluctuating wall-normal vorticity increases within the roughness height. Beyond the roughness crest, the backswimmer profile for all cases decreases and become close to S00. The profile is not significantly affected by the changes in the roughness geometry.

In the spanwise direction (Figure 5.20), the profile behaviour is similar to the wall-normal direction except for the magnitude of the profiles. Compared to the other vorticity components, the spanwise vorticity has the highest profile and is independent of the changes in the roughness geometry.

Plotted against y'/δ, the maximum vorticity for all backswimmer cases along the channel height occurs at the same location regardless of the change in the number of roughness elements in the streamwise or spanwise directions. This may suggest that the small scale turbulent structures are not significantly affected by the changes in the roughness geometry [72].

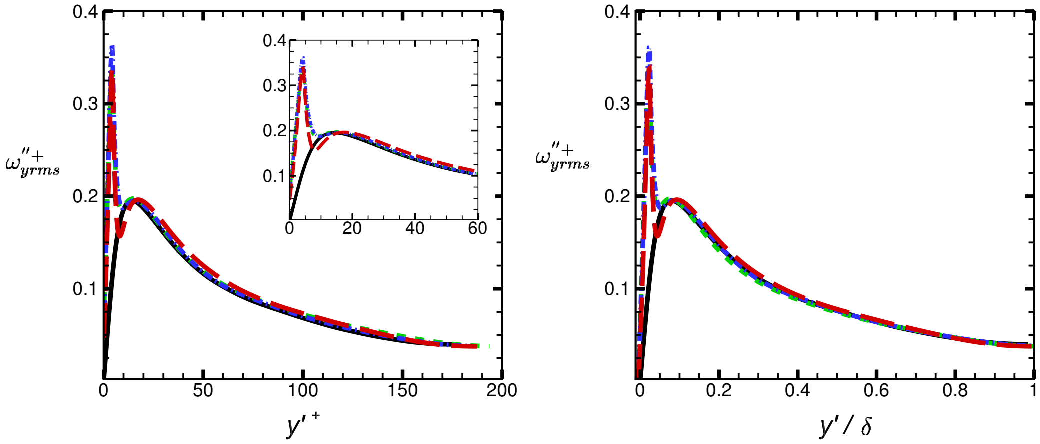

(a) (b)

Figure 5.19: Spatially-averaged r.m.s of wall-normal fluctuating vorticity for S00 (—), BS1810 (- -), BS3210 (-·-·-·-) and BS3215 (— —). The distance from the wall in (a) wall coordinates: y'^+ (b) global coordinates: y'/δ.

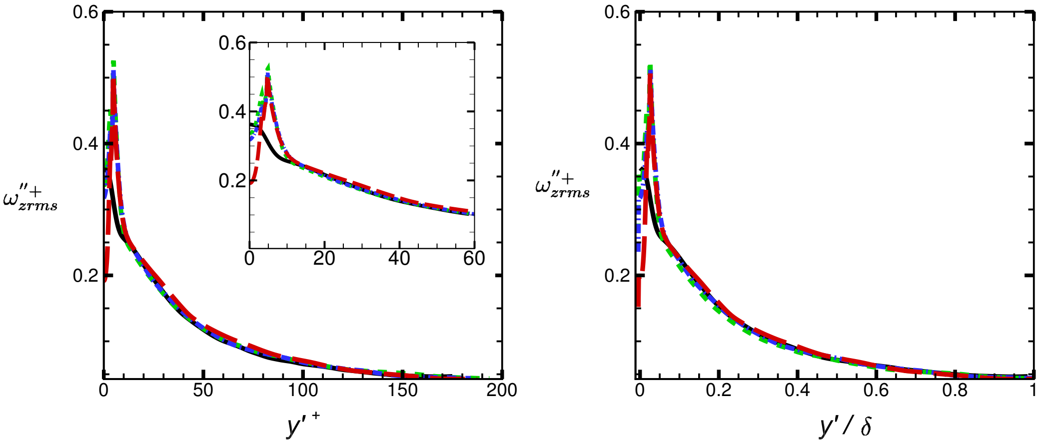

(a) (b)

Figure 5.20: Spatially-averaged r.m.s of spanwise fluctuating vorticity for S00 (—), BS1810 (- -), BS3210 (-·-·-·-) and BS3215 (— —). The distance from the wall is evaluated in (a) wall coordinates: y'^+ (b) global coordinates: y'/δ.

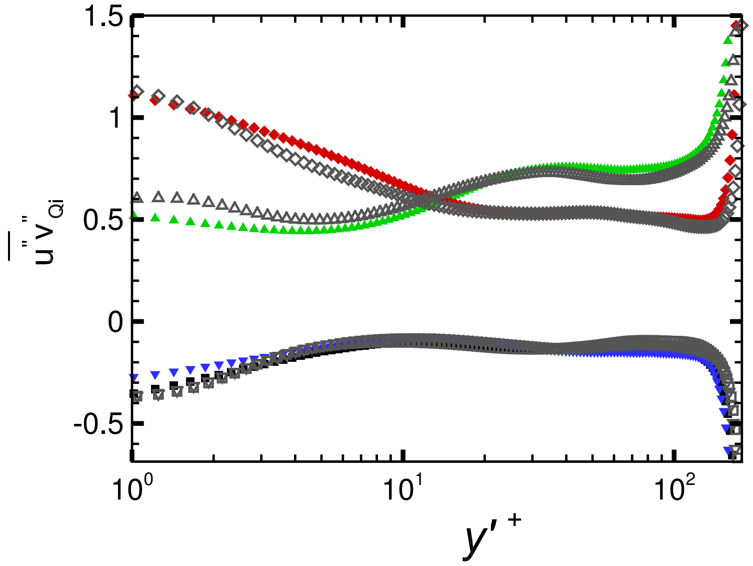

Figure 5.21: Quadrant analysis for S00 compared to Kim et al. [20] (grey). Q1 (■), Q2 (▲), Q3 (▼) and Q4 (♦).

5.8 Quadrant Analysis

The quadrant analysis is a simple yet effective tool for data processing. The flow is mainly recognised based on the sign of the streamwise and the wall-normal fluctuation velocity signs. The four quadrants are categorised as follows: The first quadrant Q1 ($u'' > 0, v'' > 0$) represents the outward motion of high speed fluid. The second quadrant Q2 ($u'' < 0, v'' > 0$) contains the motions associated with ejection of low speed fluid away from the wall. The third quadrant Q3 ($u'' < 0, v'' < 0$) contains the inward motion of low speed fluid. The forth quadrant Q4 ($u'' > 0, v'' < 0$) contains the inrush of the high speed fluid also known as the sweep event [20],[73]. Variation of the four quadrants for S00 is shown in Figure 5.21. Also, plotted on the figure is the corresponding data from Kim et al. [20]. The presented results are in agreement with those in Kim et al. [20] For S00, Q1 and Q3 profiles do not change significantly compared to Q2 and Q4. Sweep event Q4 is dominant for the region starting from the wall up to $y'^+ \approx 12$. After this the contribution associated with ejection event Q2 becomes dominant.

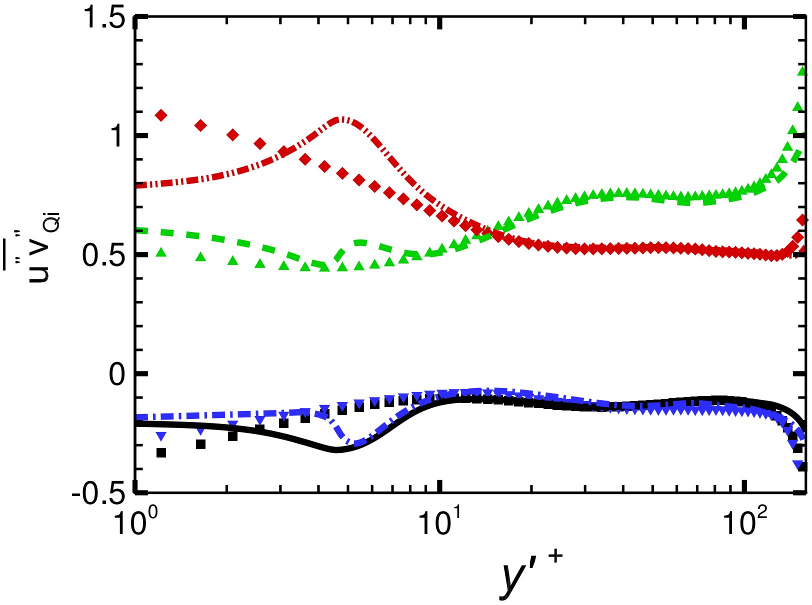

Figure 5.22: Quadrant analysis for BS1810. Q1 (—), Q2 (- -), Q3 (-·-·-·-) and Q4 (-··-··-) compared to S00 case. Q1 (■), Q2 (▲), Q3 (▼) and Q4 (♦).

Among all the presented backswimmer cases in Figures 5.22, 5.23 and 5.24 the quadrant profiles exhibit the following behaviour,

- The dominance of sweep events before Q2/Q4 intersection point and ejection event after Q2/Q4 intersection point.
- The intersection point for Q2/Q4 is slightly shifted away from the channel wall for all the backswimmer test cases as the intersection occurs at $y'^+ = 15$.
- Unlike S00 case the backswimmer cases do not exhibit similar Q1 and Q3 profiles for $y'^+ < 10$.

To analyse the effect of the change in geometry on each quadrant behaviour, Figure 5.25 shows the change in each quadrant for all backswimmer cases compared to S00. Compared to smooth channel flow case the change in the quadrant profile is mainly in the region $y'^+ < 10$ whereas for $y'^+ > 10$, the profile is similar to smooth channel flow and does not significantly change as

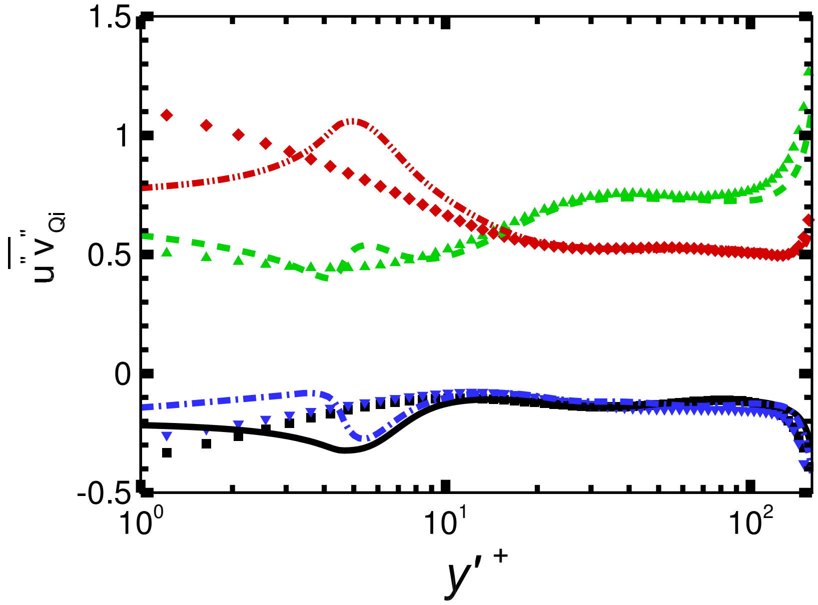

Figure 5.23: Quadrant analysis for BS3210. Q1 (—), Q2 (- -), Q3 (-·-·-·-) and Q4 (-·-·-·-) compared to S00 case. Q1 (■), Q2 (▲), Q3 (▼) and Q4 (♦).

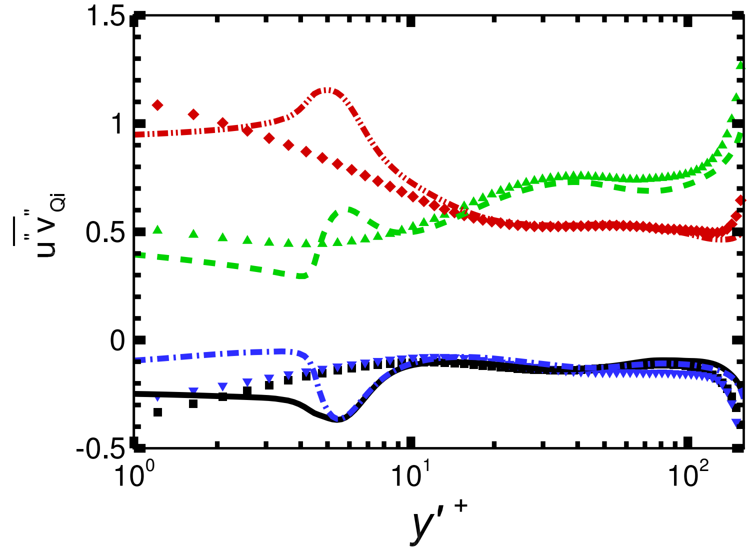

Figure 5.24: Quadrant analysis for BS3215. Q1 (—), Q2 (- -), Q3 (-·-·-·-) and Q4 (-·-·-·-) compared to S00 case. Q1 (■), Q2 (▲), Q3 (▼) and Q4 (♦).

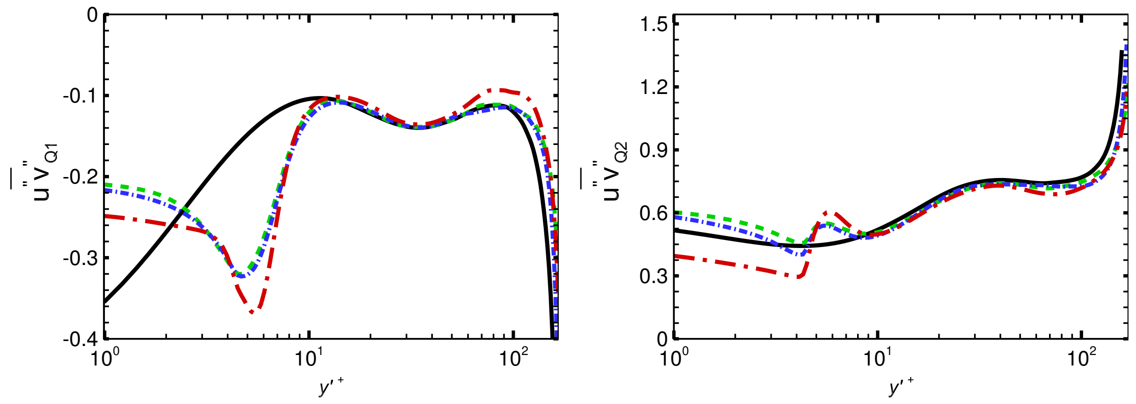

(a) Q1

(b) Q2

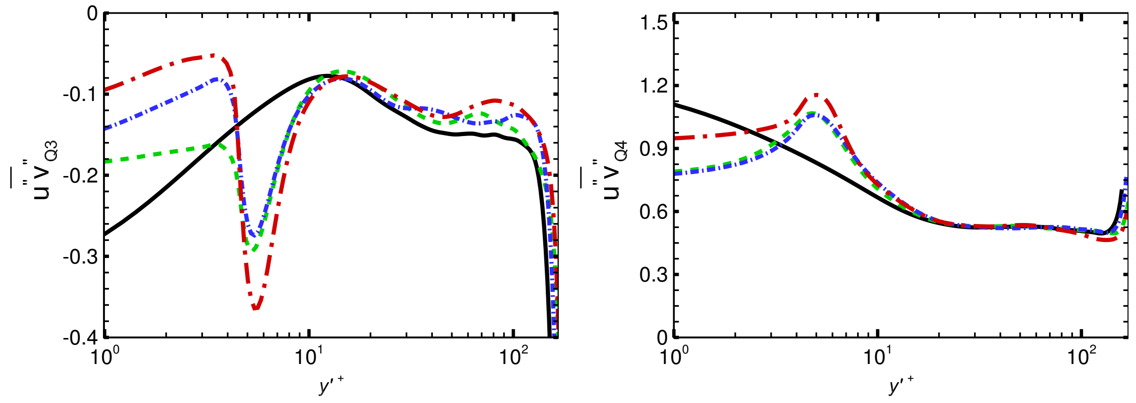

(c) Q3

(d) Q4

Figure 5.25: Quadrant analysis for S00 (—), BS1810 (- -), BS3210 (-·-·-·-) and BS3215 (—·—).

the backswimmer geometry changes specially for BS1810 and BS3210 with a slight increase in the profile for BS3215.

Compared to the smooth channel flow, the outward event (Q1) decreases for $0 < y^{'+} < 3$. Afterwards, an increase in Q1 event is noticed for $3 < y^{'+} < 10$ compared to S00. The effect of the increase in the number of elements in the streamwise direction is less significant than that of the increase in the number of elements in the spanwise direction.

For ejection event (Q2) BS1810 has the highest increase in ejection event. For BS3210, Q2 event reduces compared to BS1810. The most significant reduction in Q2 event is noticed for the BS3215 for $y^{'+} < 3$. Although BS3215 has the lowest ejection event for $y^{'+} < 3$, the profile exhibits the most increase for $3 < y^{'+} < 10$. For $y^{'+} > 10$ all Q2 events are similar to S00.

For inward activity (Q3), compared to S00, BS3215 exhibits the least inward event followed by BS3210 and BS1810 for $y^{'+} < 3$. For $3 < y^{'+} < 10$ BS3215 has the highest Q3 event followed by BS3210 and BS1810. For $3 < y^{'+} < 10$, the increase in the number of elements in the streamwise direction is more significant than in the spanwise direction. For $y^{'+} > 10$, all backswimmer profiles are similar to each other where Q3 event is reduced compared to S00.

For Q4, all backswimmer geometries sweep activity decreases compared to S00 particularly BS3210. For $3 < y^{'+} < 10$, sweep event increases compared to S00. Q4 profile for BS1810 and BS3210 is similar and the increase in the number of texture elements in the streamwise direction is insignificant. The BS3215 case exhibits the highest sweep event for $y^{'+} < 3$ and $3 < y^{'+} < 10$. For $y^{'+} > 10$, all the cases have a similar profile.

5.8.1 Intense Quadrants

The intense quadrant events are presented in this section for all backswimmer cases compared to smooth channel case. The four quadrants are shown for $H = 0$ which represents the normal events, $H = 3$ and $H = 6$ represent stronger events where H defines the borders of the data across the four quadrants [73].

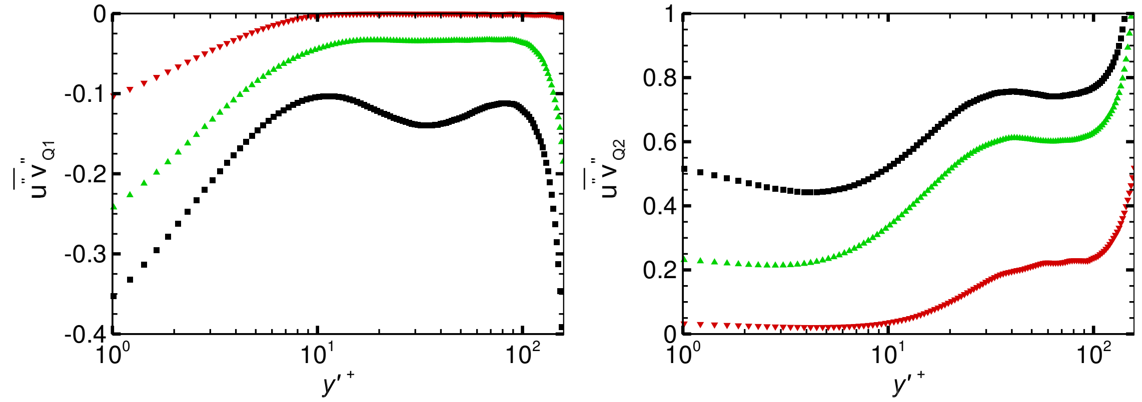

(a) Q1. (b) Q2.

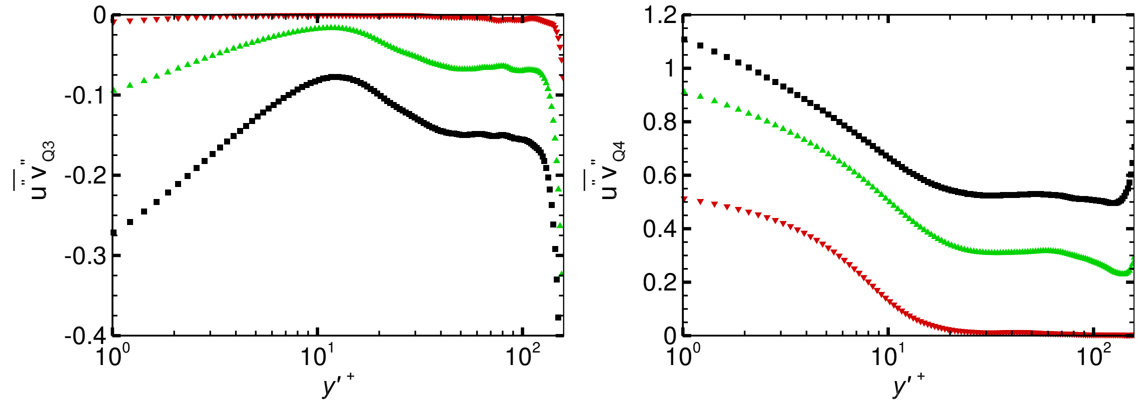

(c) Q3. (d) Q4.

Figure 5.26: Intense Quadrants for S00 case. $H = 0$ (■), $H = 3$ (▲), $H = 6$ (▼).

Variation of the intense quadrants profile for S00 is shown in Figure 5.26. As the value of H increases the quadrants event decreases, at $H = 6$ Q1, Q3 and Q4 profiles are close to zero for $y'^+ > 10$ whereas Q2 is the only event with a profile higher than zero. For $y'^+ < 10$, At $H = 6$ Q2, Q3 profiles are close to zero whereas Q1 and Q4 are the only events with a profile higher than zero. Variation of the intense quadrants profile for case BS1810 compared to S00 is shown in Figure 5.27. For Q1, at all values of H, the outward event decreases for $y'^+ < 3$ and increases for $3 < y'^+ < 10$. For $y'^+ > 10$, the profile is similar to S00. For $3 < y'^+ < 10$, as H increases, the outward event reduces and the profile is similar to S00 at $H = 6$. For Q2, compared to S00

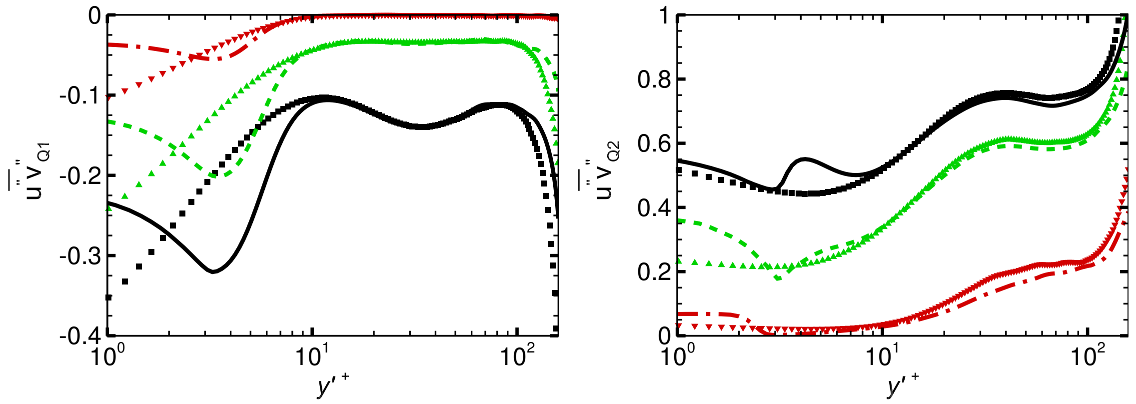

(a) Q1. (b) Q2.

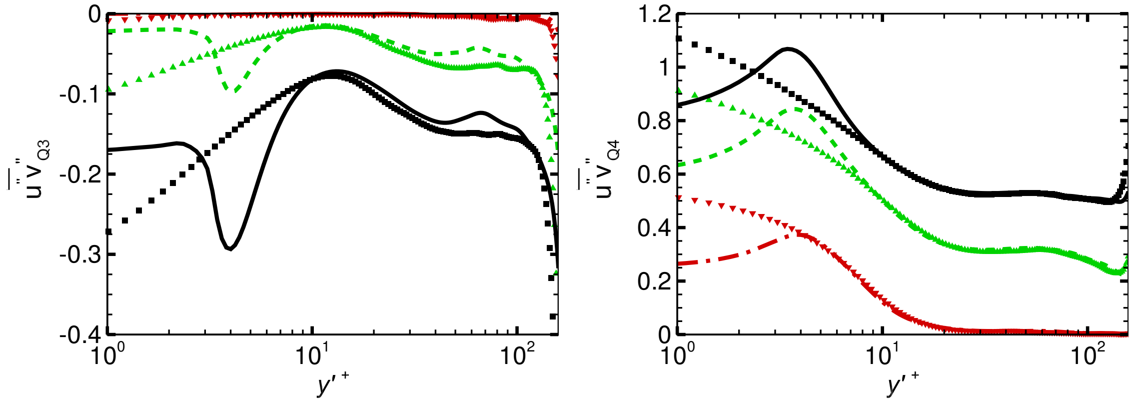

(c) Q3. (d) Q4.

Figure 5.27: Intense Quadrants for BS1810 case. $H = 0$ BS (—) , $H = 3$ BS (- -), $H = 6$ BS (-·-·-·) and $H = 0$ S (■), $H = 3$ S (▲), $H = 6$ S (▼).

at $H = 0$ ejection event decreases for $y^{'+} < 3$, increases for $3 < y^{'+} < 10$ and becomes similar to S00 for $y^{'+} > 10$. At $H = 3$, the profile increases for $y^{'+} < 3$ where the increase is more significant than at $H = 0$. Afterwards, the profile decreases for $3 < y^{'+} < 10$ and become similar to S00 for $y^{'+} > 10$. At $H = 6$, the profile is similar to S00 through out the whole channel.

For Q3, compared to S00 at all values of H inward event decreases for $y^{'+} < 3$, significantly increases for $3 < y^{'+} < 10$. For $y^{'+} > 10$ inward event decreases at $H = 0$ and $H = 3$. For $3 < y^{'+} < 10$ as H increases, the inward event reduces. The profile is similar to the S00 case at $H = 6$.

For Q4, a decrease in Q4 activity is noticed at all values of H for $y^{'+} < 3$. For $H = 0$ and $H = 3$ an increase in sweep activity is noticed for $3 < y^{'+} < 10$ beyond this point, the profile is similar to the S00 case along the whole channel for all values of H.

The effect of increasing the number of roughness elements in the streamwise direction BS3210 on the intense quadrants profile is shown in Figure 5.28. For outward (Q1) and inward (Q3) events the increase in the number of roughness elements in the streamwise direction is insignificant compared to the BS1810 described earlier at all values of H. For Q2, at $H = 3$ BS3210 ejection event exhibits more significant decrease for $3 < y^{'+} < 10$ compared to BS1810. For Q4, the profile is not significantly affected by the increase in the number of roughness elements in the streamwise direction.

The effect of increasing the number of roughness elements in the spanwise direction on the intense quadrants profiles is shown in Figure 5.29. For Q1, BS3215 outward activity increases compared to S00, BS1810 and BS3210 specially for $3 < y^{'+} < 10$ at $H = 0$ and $H = 3$. For $H = 6$, the increase in the number of elements in the spanwise direction is not significant for Q1 event.

For Q2, BS3215 ejection event decreases compared to all backswimmer cases for $y^{'+} < 3$. Also, at $H = 0$ a significant increase in ejection event is noticed when the number of spanwise elements increases for $3 < y^{'+} < 10$. As H increases Q2 profile is similar to BS1810 and BS3210. For Q3, BS3215 inward activity increases significantly compared to BS3210 and BS1810 for $y^{'+} < 3$. Also, Q3 event significantly increases for $3 < y^{'+} < 10$ compared to BS3210

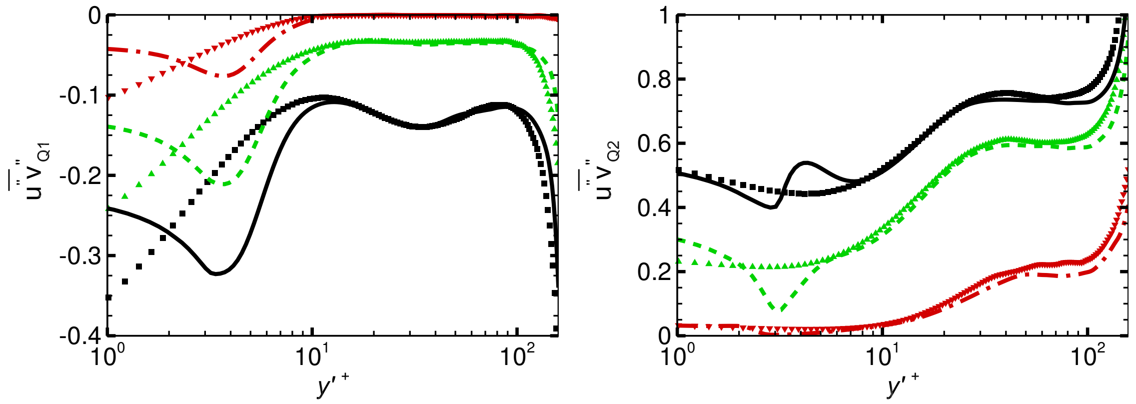

(a) Q1.

(b) Q2.

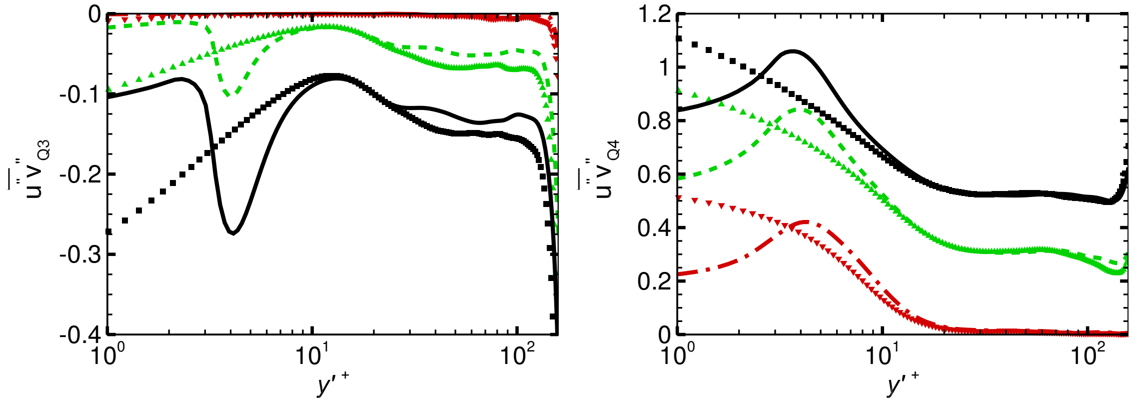

(c) Q3.

(d) Q4.

Figure 5.28: Intense Quadrants for BS3210 case. $H = 0$ BS (—) , $H = 3$ BS (--), $H = 6$ BS (-·-·-·-) and $H = 0$ S (■), $H = 3$ S (▲), $H = 6$ S (▼).

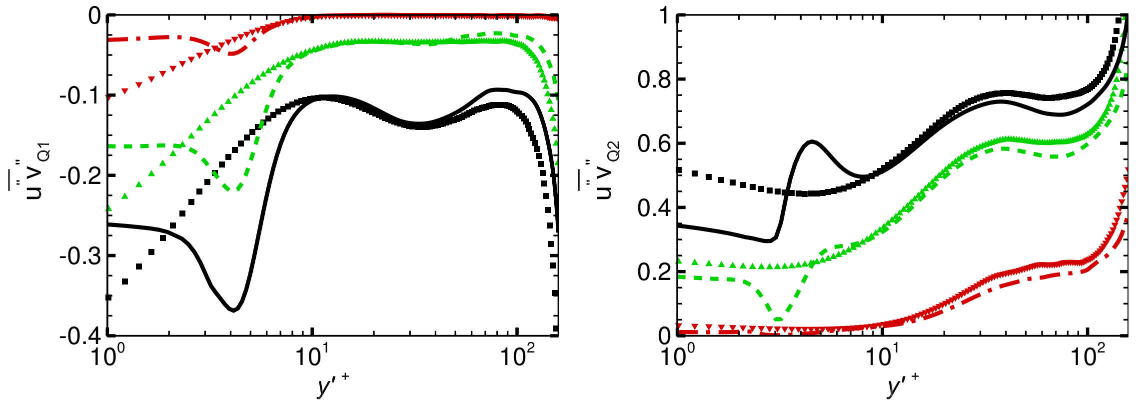

(a) Q1.

(b) Q2.

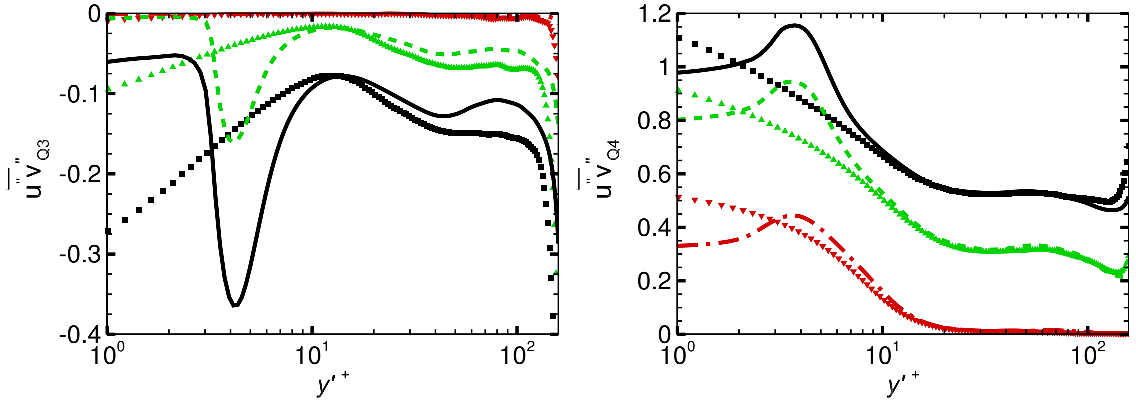

(c) Q3.

(d) Q4.

Figure 5.29: Intense Quadrants for BS3215 case. $H = 0$ BS (—) , $H = 3$ BS (- -), $H = 6$ BS (-·-·-·-) and $H = 0$ S (■), $H = 3$ S (▲), $H = 6$ S (▼).

and BS1810. This change is noticed at $H = 0$ and $H = 3$. For Q4, The effect of increasing the number of elements in the spanwise direction is not significant at all values of H for the whole channel.

5.9 Flow Visualisations

To understand the effect of using backswimmer geometry on the turbulent flow, the flow structure is visualised by means of fluctuating velocities and the second largest Eigen value of symmetric tensor λ_2 iso-surfaces by Jeong and Hussain [6]. It should be noted that all 3D iso-surface plots included in this section are instantaneous and captured at different time instants (each with $\Delta t^+ \approx 100$ apart) after the flow was fully developed. Also, all of the 3D plots present the changes in $u^{'+}$ and λ_2 from the channel wall until approximately $y^+ = 8$ which is just above the roughness crest.
From the BS1810 3D plots shown in Figure 5.30 at different instants the flow can be described as follows,

- The low-speed streaks are present around the roughness elements specially on the roughness crest and in the region separating the roughness elements in the streamwise direction.
- The high-speed streaks are present along the domain. The intensity of the high-speed streaks is significantly higher than the low-speed ones and their distribution is non-uniform along the channel.
- λ_2 streaks are present within the roughness elements and exhibit a sparse shape.

Figure 5.31 shows flow visualisation for BS3210 in which the number of elements in the streamwise direction is increased from 18 to 32. The following can be seen from the figure,

- The low-speed streaks around the roughness elements are elongated compared to BS1810. Also, the intensity of the streaks increases compared to BS1810.

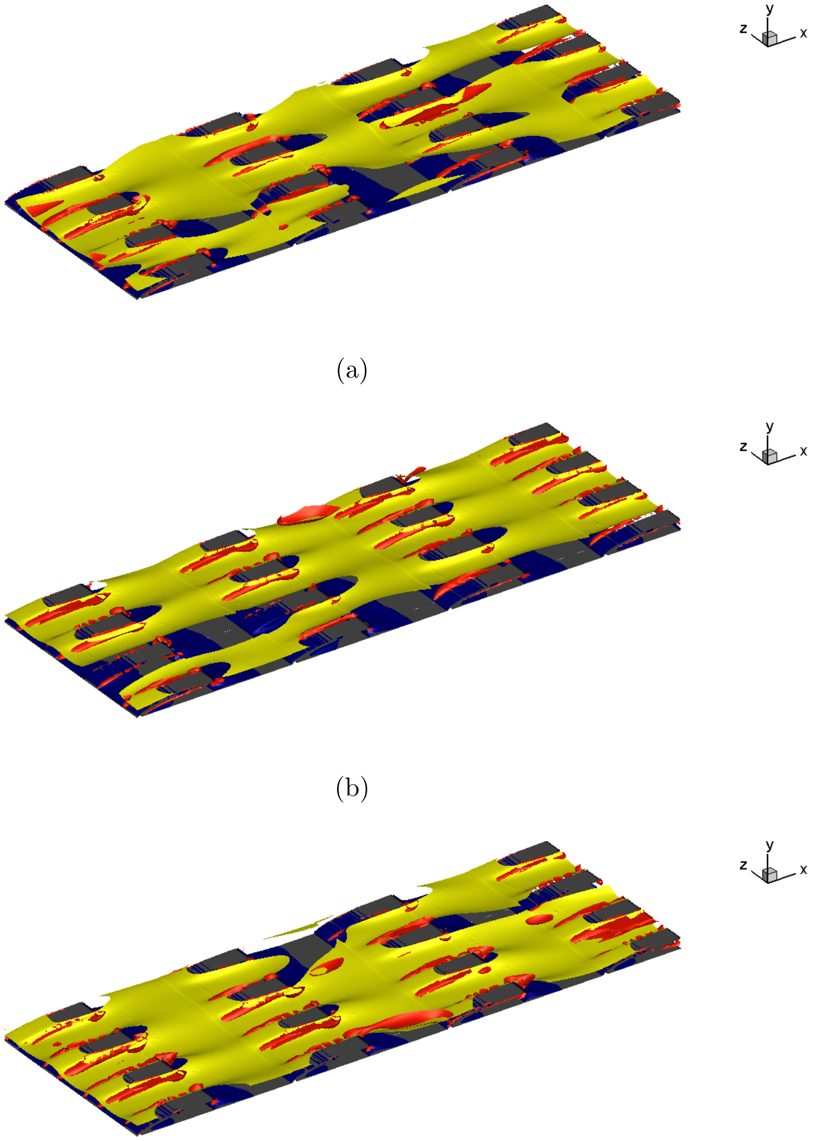

(a)

(b)

(c)

Figure 5.30: BS1810 iso-surface plots for low, high velocity streaks and λ_2 where blue $u'/u_\tau = -0.12$, yellow $u'/u_\tau = 2$ and red $\lambda_2/(u\tau/\delta) = -0.005$ for part of the computational domain in the streamwise and spanwise directions at three time instants (each with $\Delta t^+ \approx 100$).

- The high-speed streaks are located in the region separating the roughness elements in the spanwise direction only unlike BS1810 where the streaks were present along the channel.
- In terms of λ_2, Similar to BS1810 the streaks are present around the roughness elements only with sparse shapes. However, a slight decrease in the intensity of λ_2 elements is noticed around some elements compared to BS1810.

By keeping the same number of elements as BS3210 but increasing the number of elements in the spanwise direction to 15, the below behaviour can be seen from Figure 5.32 (BS3215),

- Although the low-speed streaks remains within the roughness elements region, as the number of elements in the spanwise direction increases a decrease in the streaks width is noticed for all the presented time instants.
- The high-speed streaks width significantly decreases compared to BS1810 and BS3210.
- λ_2 intensity is similar to BS3210 and slightly less than BS1810.

Figures 5.33 - 5.35 show the change in the instantaneous flow structure for the fluctuating velocity calculated using u'^+ for all backswimmer cases for the region within one roughness element by means of low-, high-speed streaks and λ_2 tensor. As the number of roughness elements increases in the streamwise (Figure 5.34) and spanwise (Figure 5.35) directions the width of the high-speed streaks decreases and the low-speed streaks width increases. As the number of roughness elements increases in the streamwise and spanwise directions, λ_2 intensity decreases specially within the roughness element.

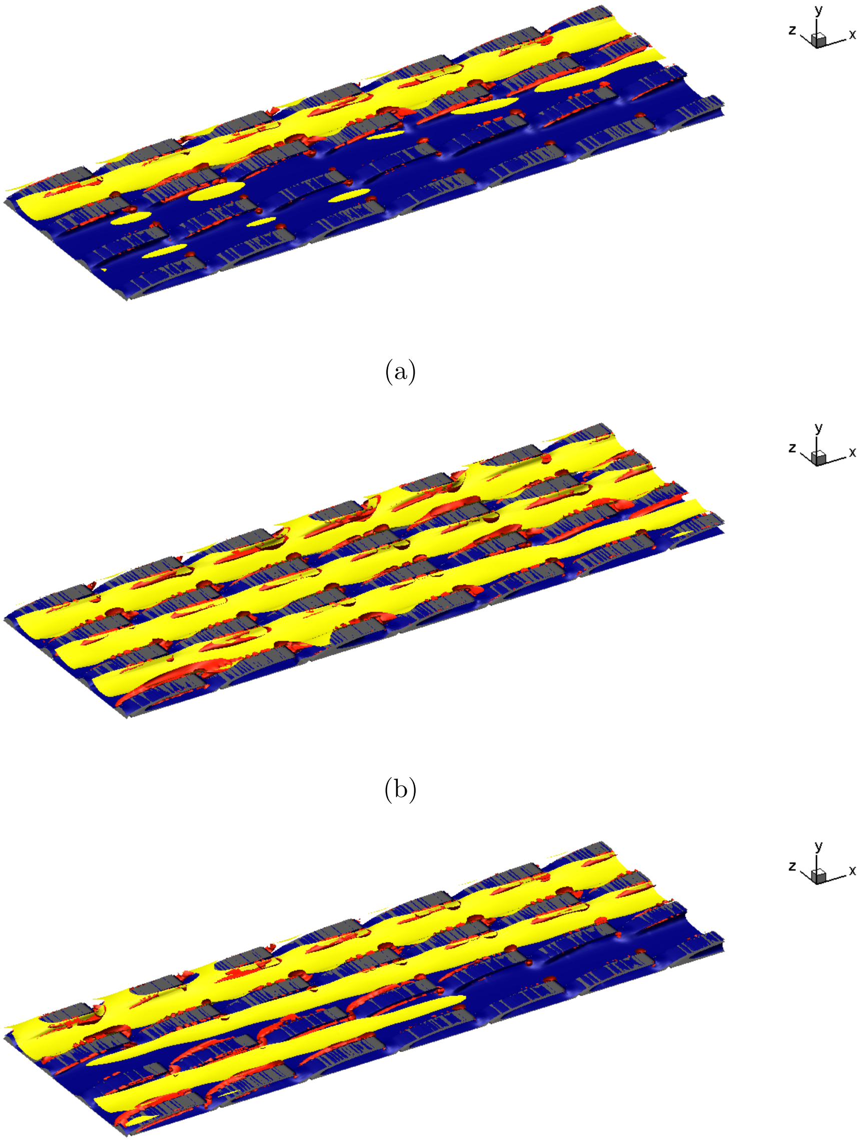

(a)

(b)

(c)

Figure 5.31: BS3210 iso-surface plots for low, high velocity streaks and λ_2 where blue $u'/u_\tau = -0.12$, yellow $u'/u_\tau = 2.0$ and red $\lambda_2/(u\tau/\delta) = -0.005$ for part of the computational domain in the streamwise and spanwise directions at three time instants (each with $\Delta t^+ \approx 100$).

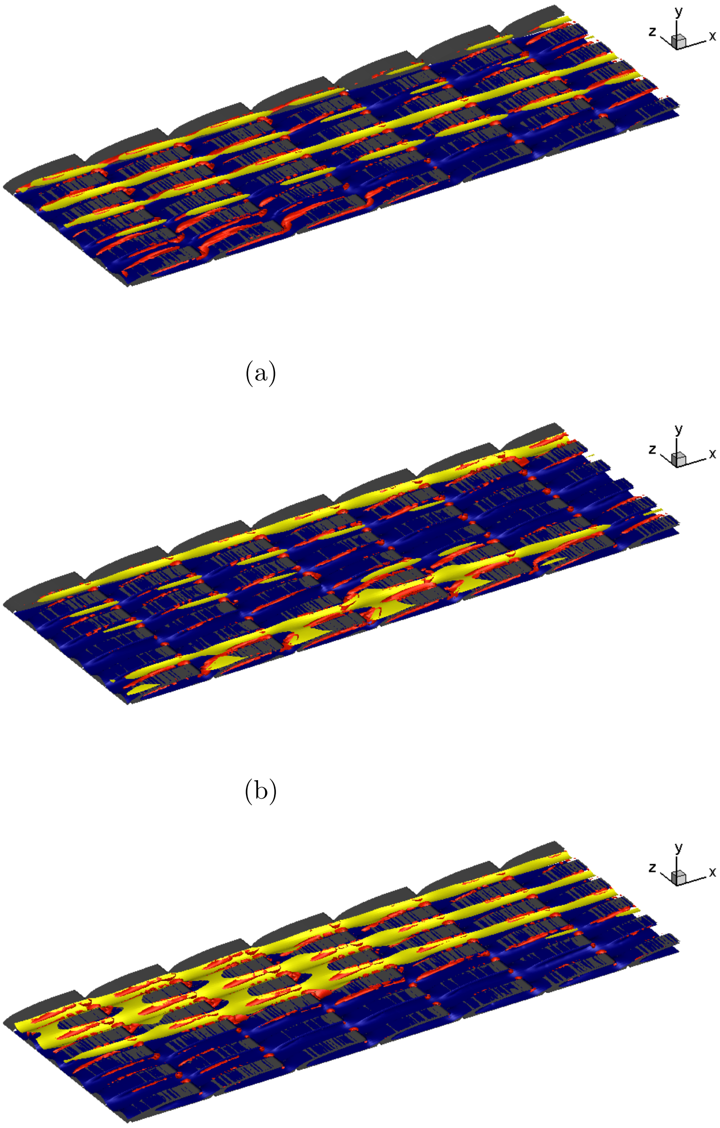

(a)

(b)

(c)

Figure 5.32: BS3215 iso-surface plots for low, high velocity streaks and λ_2 where blue $u'/u_\tau = -0.12$, yellow $u'/u_\tau = 2.0$ and red $\lambda_2/(u\tau/\delta) = -0.005$ for part of the computational domain in the streamwise and spanwise directions at three time instants (each with $\Delta t^+ \approx 100$).

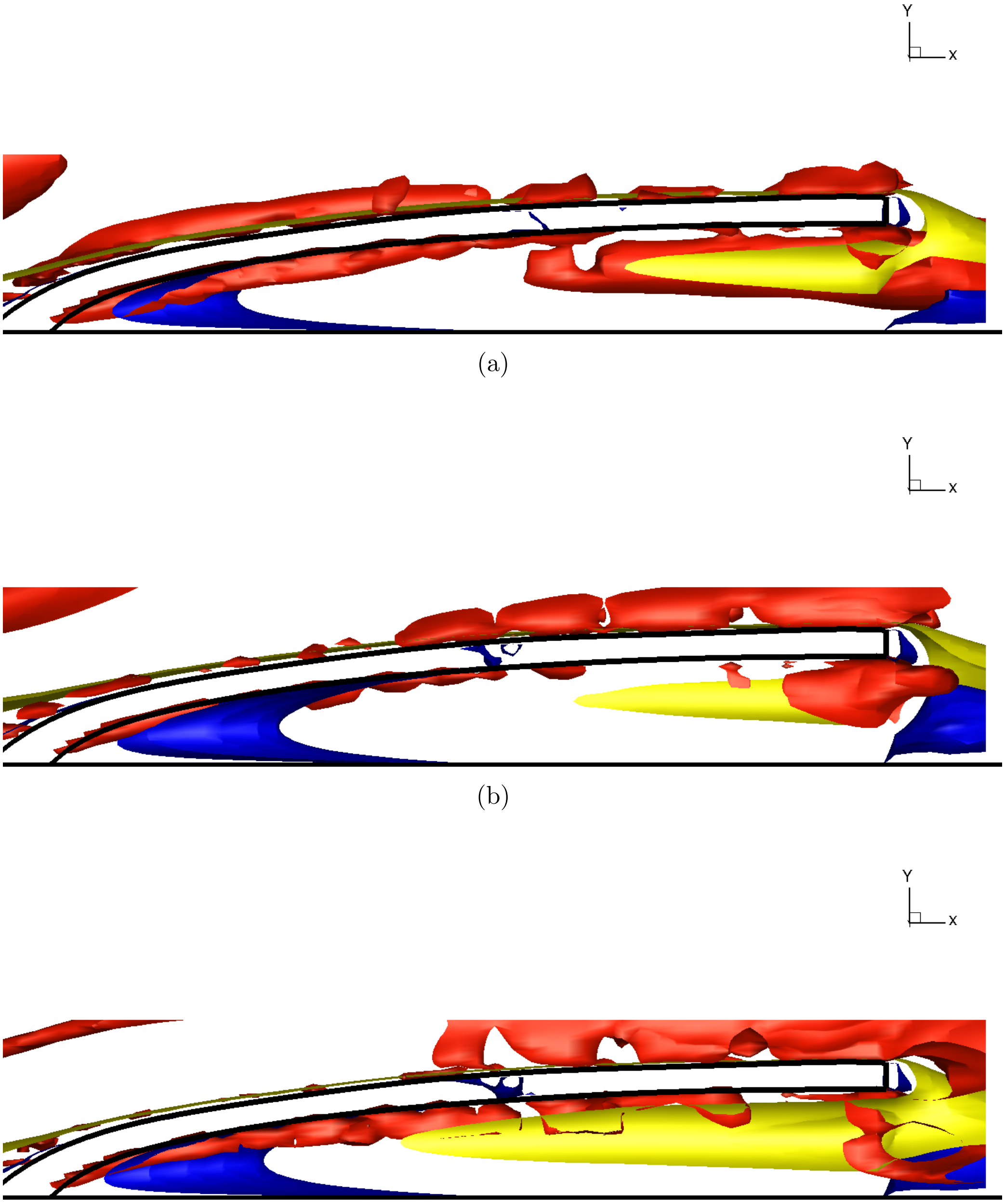

(a)

(b)

(c)

Figure 5.33: BS1810 iso-surface plots for low, high velocity streaks and λ_2 where blue $u'/u_\tau = -0.12$, yellow $u'/u_\tau = 0.5$ and red $\lambda_2/(u\tau/\delta) = -0.002$ for one roughness element at three time instants (each with $\Delta t^+ \approx 100$).

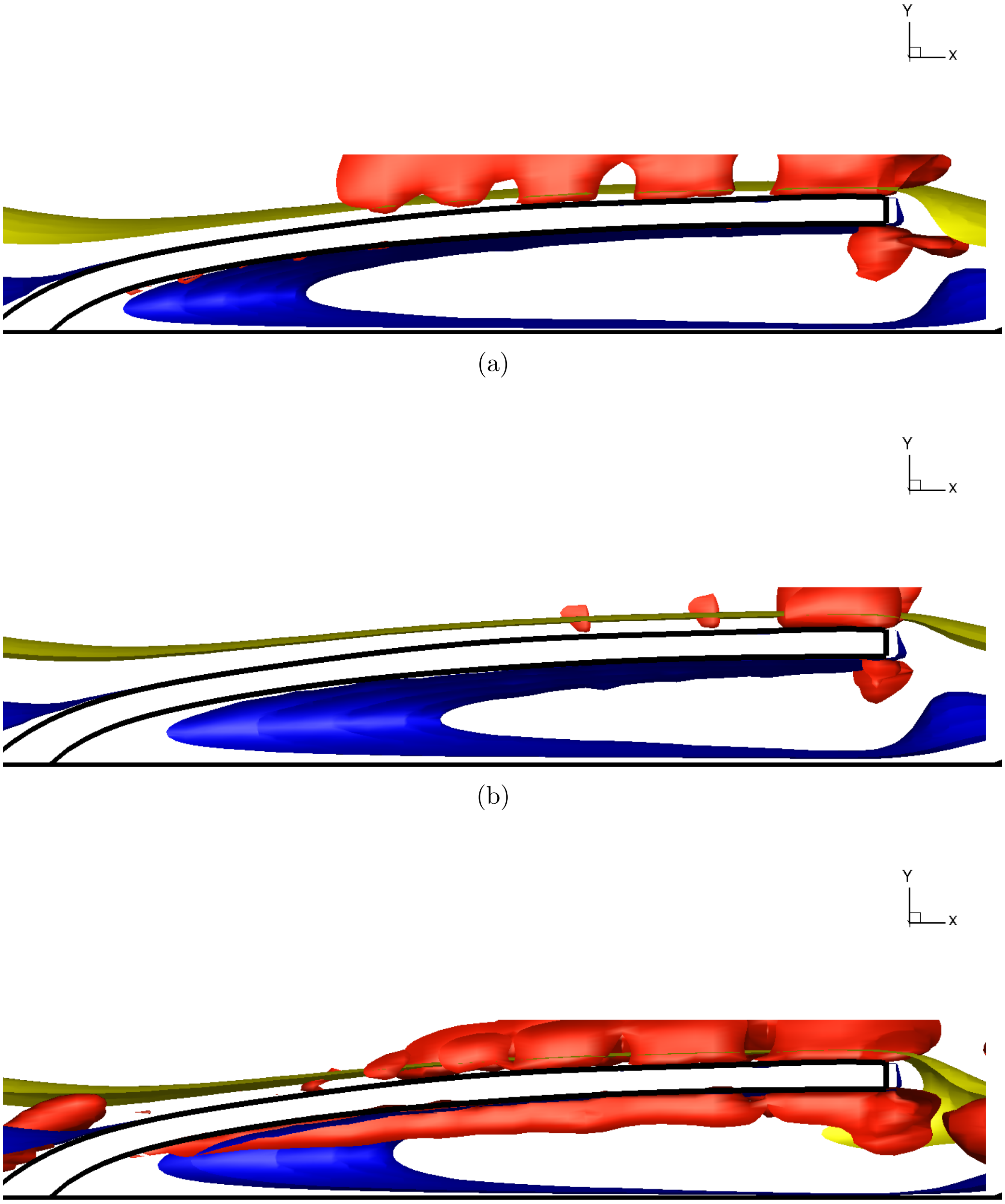

(a)

(b)

(c)

Figure 5.34: BS3210 iso-surface plots for low, high velocity streaks and λ_2 where blue $u'/u_\tau = -0.12$, yellow $u'/u_\tau = 0.5$ and red $\lambda_2/(u\tau/\delta) = -0.002$ for one roughness element at three time instants (each with $\Delta t^+ \approx 100$).

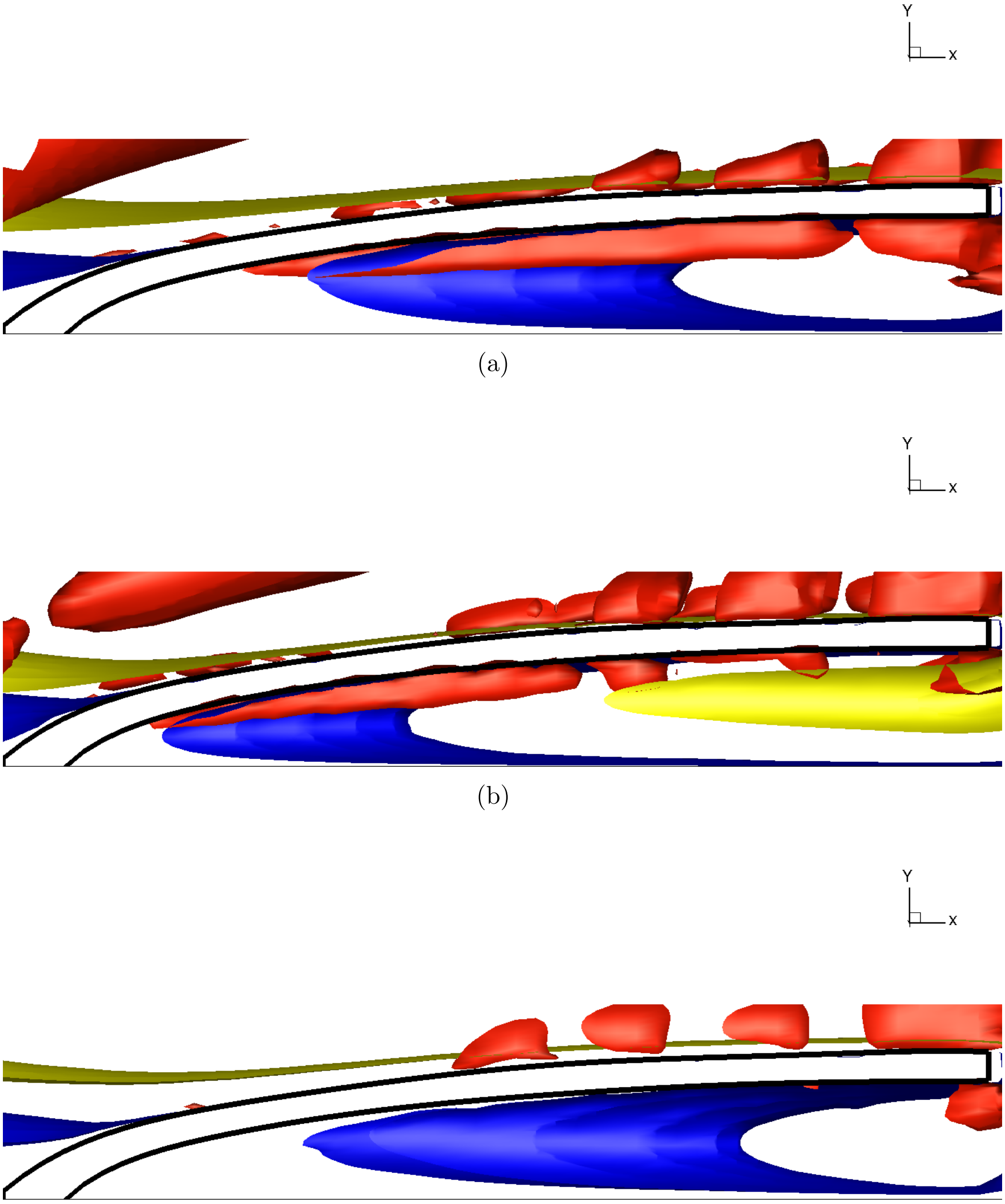

(a)

(b)

(c)

Figure 5.35: BS3215 iso-surface plots for low, high velocity streaks and λ_2 where blue $u'/u_\tau = -0.12$, yellow $u'/u_\tau = 0.12$ and red $\lambda_2/(u\tau/\delta) = -0.002$ for one roughness element at three time instants (each with $\Delta t^* \approx 100$).

Chapter 6

Backswimmer Turbulent Flow at Different Reynolds Numbers

This chapter is dedicated to presenting the backswimmer geometry simulations at different Reynolds numbers. The aim is to study the effect of the backswimmer textured surface for channel flows at Reynolds numbers $Re = 2800, 3500, 5500$ and 7400. All simulations are compared to smooth channel cases at all Reynolds numbers. The effect of textured surfaces at different Reynolds numbers is studied by discussing the variation of: spatially-averaged velocity, root-mean-square of fluctuating velocity, Reynolds shear stress, root-mean-square of fluctuating vorticity and quadrant analysis.
The flow structure for all backswimmer cases is presented and the effect of the change in Reynolds number on the flow topology is demonstrated by means of the change in the streamwise fluctuating velocity and the second largest Eigen value of the symmetric tensor λ_2 by Jeong and Hussain [6] for the computational domain and one roughness element.

6.1 Simulation Parameters

To study the effect of changing Reynolds number, four backswimmer test cases were simulated and compared to smooth channel flow cases. The simulation parameters for all the studied test cases in this chapter are shown in

Table 6.1. For these test cases, the width-to-height ratios in the streamwise and spanwise directions are $w_x/h = 0.0$, $w_z/h = 2.0$ which translates to 36 roughness elements in the streamwise and 10 elements in the spanwise directions. The notation of the presented cases is based on the Reynolds number for example; BS2800 denotes backswimmer case at $Re = 2800$. Similar to Chapter 5, both computational domain and mesh parameters are consistent with the minimal channel dimensions used in Chung et al. [70]. The minimal-span length and width were verified using streamwise and spanwise two point correlation for all test cases. For the instantaneous flow fields, time integral tests were applied and all the captured contour and iso-surface plots are extracted with $\Delta t^+ \approx= 100$ apart.

Table 6.1: Details of simulated test cases where S denotes smooth ($Re_\tau = Re_{\tau s}$) and BS denotes backswimmer ($Re_\tau = Re_{\tau r}$)
.

Case	Re	Re_τ	u_τ	τ	h^+	H_x^+	H_z^+	N_x	N_y	N_z	c_f	$DR\%$
S2800	2800	177.80	0.0508	0.00258	0.00	1280	267	1800	300	300	0.002621	N/A
S3500	3500	215.70	0.0616	0.00376	0.00	1533	324	1800	300	300	0.003806	N/A
S5500	5500	321.93	0.0919	0.00844	0.00	2318	483	1800	300	300	0.007691	N/A
S7400	7400	416.51	0.1190	0.01416	0.00	2998	625	1800	300	300	0.014042	N/A
BS2800	2800	178.70	0.0510	0.00260	5.40	1286	268	1800	300	300	0.002601	-0.780
BS3500	3500	221.20	0.0632	0.00388	6.00	1592	332	1800	300	300	0.003994	-2.290
BS5500	5500	349.00	0.0997	0.00994	10.5	2512	524	1800	300	300	0.009940	-17.67
BS7400	7400	471.10	0.1344	0.01806	14.1	3392	707	1800	300	300	0.018063	-27.55

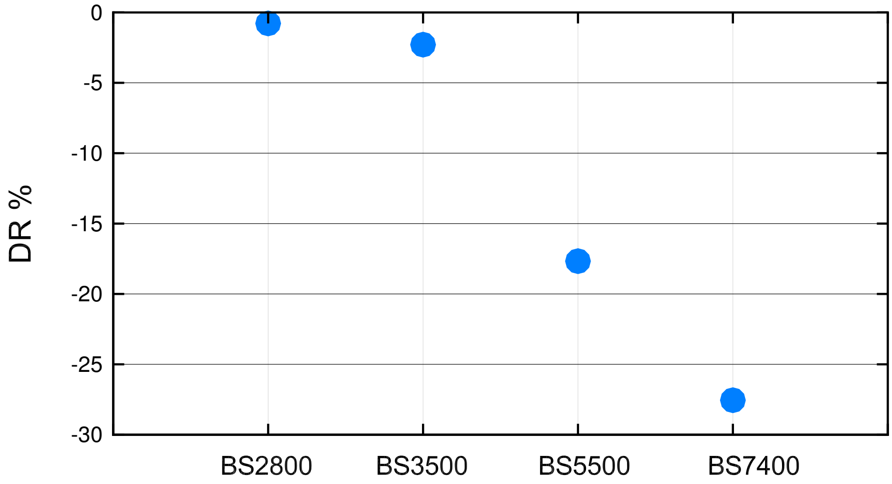

Figure 6.1: Drag reduction for BS2800, BS3500, BS5500 and BS7400 cases.

6.2 Drag Reduction

The drag reduction is calculated by means of total shear stress. The friction velocity, friction Reynolds number, total shear stress and drag reduction for all test cases is shown in Table 6.1. The drag reduction for all backswimmer cases is shown in Figure 6.1. Compared to smooth channel flow, the drag increase is directly proportional to the increase in Reynolds number. For BS2800, the backswimmer drag performance is very close to S2800. As Reynolds number increases, the value of negative DR increases which represents drag increase to reach a maximum of -27.67% for BS7400.

6.3 Roughness Function

The roughness function for textured surfaces is defined as follows [74],

$$\boldsymbol{\Delta U^{+} = \frac{1}{\kappa}\, ln\ k_s^{+} + A - 8.5} \tag{6.1}$$

where ΔU^{+} is the rough surface spatially-averaged velocity log-law intercept displacement, κ is the von-Karman constant, A is the smooth wall log-law

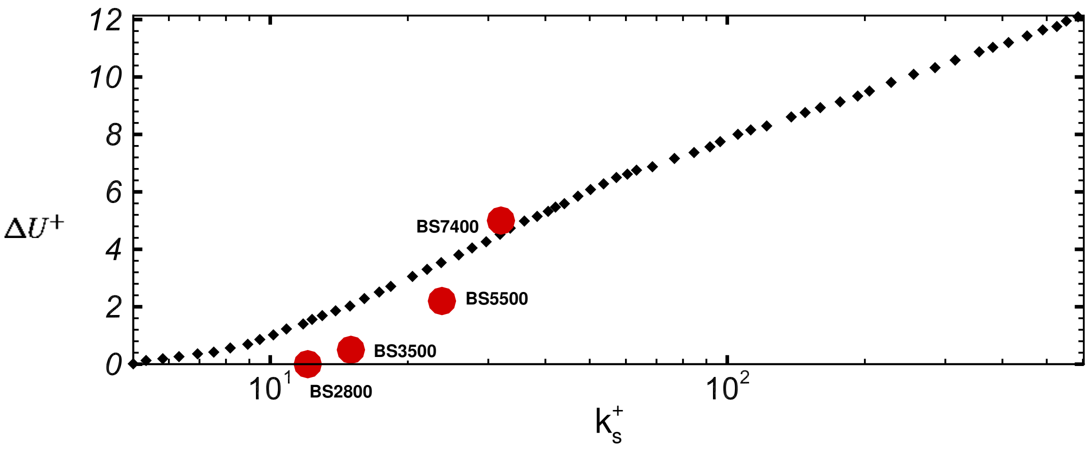

Figure 6.2: Roughness functions for backswimmer cases BS2800, BS3500, BS5500, BS7400 plotted against Nikuradze [23] sand grain data (♦).

intercept and k_s^+ is the equivalent to sand grain also known as the effective or equivalent roughness. The value of k_s is also used to define the shift in the origin of the geometry [15]. For the backswimmer geometry $k_s = 1.68h$ where h is the roughness height used by Krogstad et al. [74]. The values for all the roughness functions at all Reynolds numbers are shown in Figure 6.2. Krogstad et al. [74] suggested that the roughness local effect is up to 4 or 5 roughness heights for riblets. However, for biomimetic inspired surfaces there has not been enough data on the effect of roughness beyond the roughness height. It should be noted that ΔU^+ values shown in Figure 6.2 are not in the full rough regime, they are in the transitionally rough regime. To achieve a more accurate value for ΔU^+ higher Reynolds number simulations are required.

6.4 Spatially-Averaged Velocity

The spatially-averaged velocity profiles for the backswimmer cases compared to smooth channel cases are shown in Figure 6.3. For BS2800, the profile is similar to the S2800 specially in the log-law region. The BS3500 profile is similar to the S3500 and BS2800. The profile is not affected by the change in Reynolds number. For BS5500, a decrease in the profile compared to S5500,

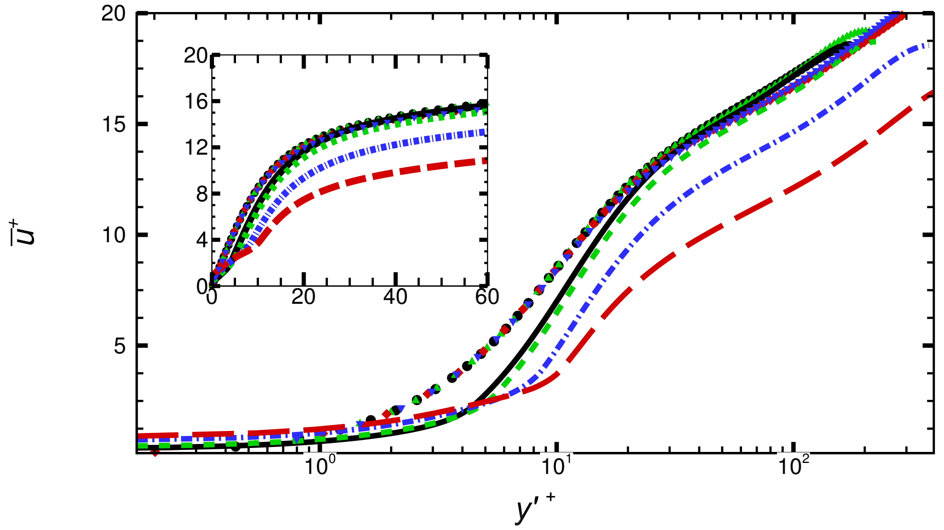

Figure 6.3: Spatially-averaged velocity profiles for BS2800 (—), BS3500 (- -), BS5500 (-·-·-·-) and BS7400 (— —) compared to S2800 (●), S3500 (▲), S5500 (▼), S7400 (♦).

BS2800 and BS3500 is noticed specially in the log-law region. The BS7400 case has the most downward displacement compared to every backswimmer case. Also, for smooth channel cases, the change in spatially-averaged velocity profile due to Reynolds number increase is not as significant as the backswimmer cases specially for BS5500 and BS7400.

6.4.1 Spatially-Averaged Velocity Logarithmic Distribution

The logarithmic distribution region for each backswimmer case is shown in Figure 6.4 and the equations are as follows,

BS2800

$$\overline{u}^+ = 1/\kappa \ln y'^+ + 5.39 \tag{6.2}$$

BS3500

$$\overline{u}^+ = 1/\kappa \ln y'^+ + 5.39 - 0.5 \tag{6.3}$$

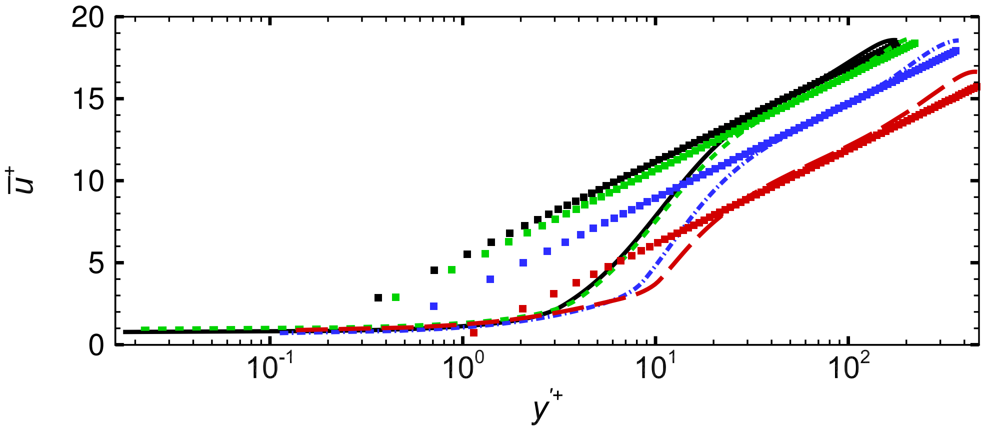

Figure 6.4: Spatially-averaged velocity logarithmic distribution for BS2800 (—), BS3500 (- -), BS5500 (-·-·-·-) and BS7400 (— —) with the spatially-averaged logarithmic distribution functions in symbols.

BS5500

$$\overline{u}^+ = 1/\kappa \ln y'^+ + 5.39 - 2.2 \tag{6.4}$$

BS7400

$$\overline{u}^+ = 1/\kappa \ln y'^+ + 5.39 - 5.0 \tag{6.5}$$

The value of B is directly proportional to Reynolds number. For BS2800 and BS3500 cases, the equations are similar to the smooth channel cases. An increase is noticed for BS5500 and BS7400 which has the highest B value. The ΔU^+ obtained from Figure 6.4 were used to calculate the effective roughness height in Figure 6.2.

6.5 R.M.S of Fluctuating Velocity

The change in the root-mean-square of streamwise fluctuating velocity at different Reynolds numbers for all backswimmer cases is shown in Figure 6.5. For BS2800, the profile is similar to S2800 along the channel. For BS3500, the increase in the Reynolds number does not affect the velocity profile significantly compared to S3500. For BS5500, the profile increases compared to S5500. Also, the peak of the profile is shifted back towards the channel wall compared to BS2800 and BS3500. These changes are also noticed for

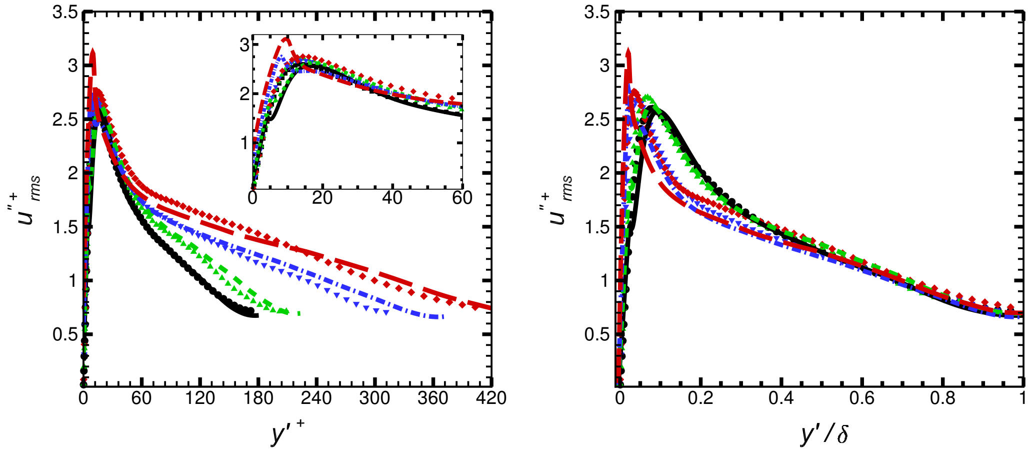

(a) (b)

Figure 6.5: Spatially-averaged r.m.s of streamwise fluctuating velocity for BS2800 (—), BS3500 (- -), BS5500 (-·-·-·-) and BS7400 (— —) compared to S2800 (●), S3500 (▲), S5500 (▼) and S7400 (♦). The distance from the wall in (a) wall coordinates: y'^{+} (b) global coordinates: y'/δ.

BS7400 as it has the highest profile. Plotted against y'/δ, for $y'/\delta < 0.4$ the change in the Reynolds number is more significant than for $y'/\delta > 0.4$ for all Reynolds numbers. For BS2800 and BS3500, the profile is similar to S2800 and S3500. For BS5500 and BS7400 the dispersive effect is noticed for $y'/\delta < 0.05$ which is 1.6 times the roughness height measured from the roughness base. The roughness effect is more significant for BS5500 and BS7400 compared to BS2800 and BS3500. Seddighi et al [25] observed a similar pattern for the pyramid geometry and the peak was significantly reduced when the data was phase-averaged instead of spatially-averaged at $Re = 7400$.

In the wall-normal direction, the backswimmer r.m.s of fluctuating velocity profiles compared to smooth channel flow at different Reynolds numbers are shown in Figure 6.6. For BS2800 the profile is similar to S2800. For BS3500, the profile slightly increases compared to S3500 in particular for $y' > 100$. For BS5500 and BS7400, it is noticed that the wall-normal velocity increases compared to S5500 and S7400. Plotted against y'/δ, the wall-normal velocity profiles are similar to the case were the profiles were plotted against y'^{+}.

The change in the r.m.s of fluctuating velocity in the spanwise direction is

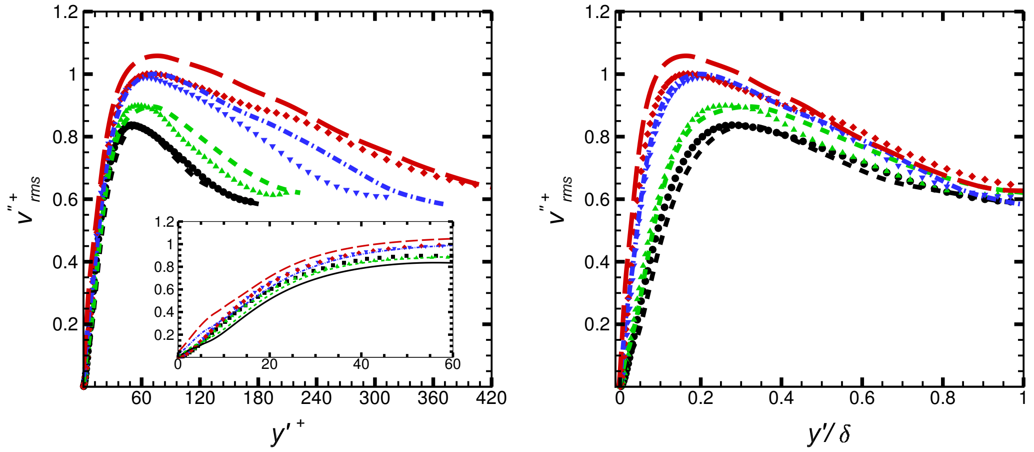

(a) (b)

Figure 6.6: Spatially-averaged r.m.s of wall-normal fluctuating velocity for BS2800 (—), BS3500 (- -), BS5500 (-·-·-·-) and BS7400 (— —) compared to S2800 (●), S3500 (▲), S5500 (▼) and S7400 (♦). The distance from the wall in (a) wall coordinates: y'^+ (b) global coordinates: y'/δ.

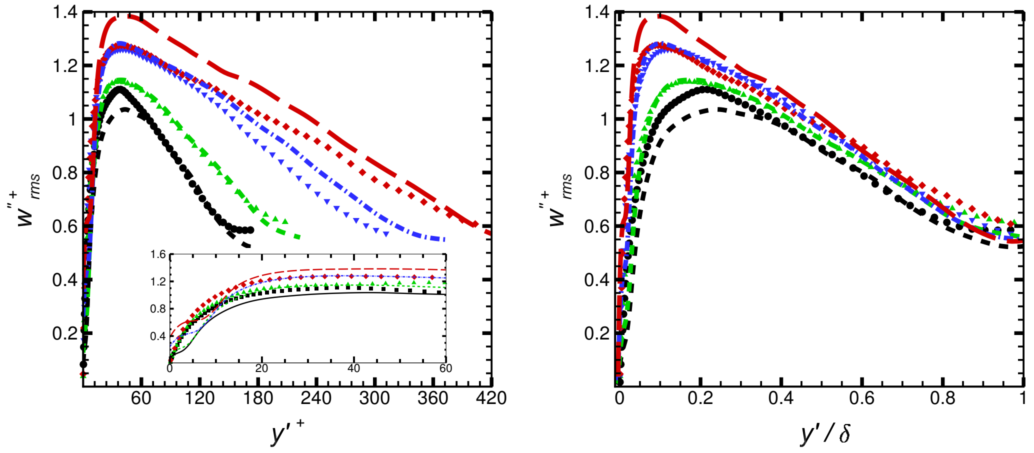

(a) (b)

Figure 6.7: Spatially-averaged r.m.s of spanwise fluctuating velocity for BS2800 (—), BS3500 (- -), BS5500 (-·-·-·-) and BS7400 (— —) compared to S2800 (●), S3500 (▲), S5500 (▼) and S7400 (♦). The distance from the wall in (a) wall coordinates: y'^+ (b) global coordinates: y'/δ.

shown in Figure 6.7. For BS2800 the profile slightly decreases compared to S2800 particularly by the profile peak. For BS3500, the profile does not change compared to S3500 but increases compared to BS2800. For the BS5500 and BS7400, the spanwise velocity profile increases compared to S5500 and S7400. Plotted against y'/δ, for BS2800 the profile decreases compared to S2800. For BS3500, the profile is similar to S3500. For BS5500 and BS7400, the profile increases compared to S5500 and S7400. Also the profile peak is shifted towards the roughness base as Reynolds number increases.

6.6 Reynolds Shear Stress

The change in the Reynolds shear stress profile for the backswimmer cases compared to smooth channel flow at different Reynolds numbers is shown in Figure 6.8. For BS2800, the Reynolds shear stress profile is similar to S2800. For BS3500, a slight increase in the Reynolds shear stress profile is noticed compared to S3500.

As the Reynolds number increases in BS5500, the increase in the Reynolds shear stress profile is more significant, this is also applicable for BS7400. For all backswimmer cases, the peak location of the Reynolds shear stress profile does not change either compared to the smooth cases or to each other. The increase in the Reynolds shear stress for all backswimmer cases is consistent with the previously obtained drag performance. Plotted against y'/δ, the location of the maximum Reynolds shear stress for the backswimmer cases is similar to smooth channel. As the Reynolds number increases, the peak of the profile is shifted backwards towards the channel wall.

6.7 R.M.S of Fluctuating Vorticity

The change in the r.m.s of streamwise fluctuating vorticity for the backswimmer cases compared to the smooth channel at different Reynolds numbers is shown in Figure 6.9. For all backswimmer cases, the effect of the textured

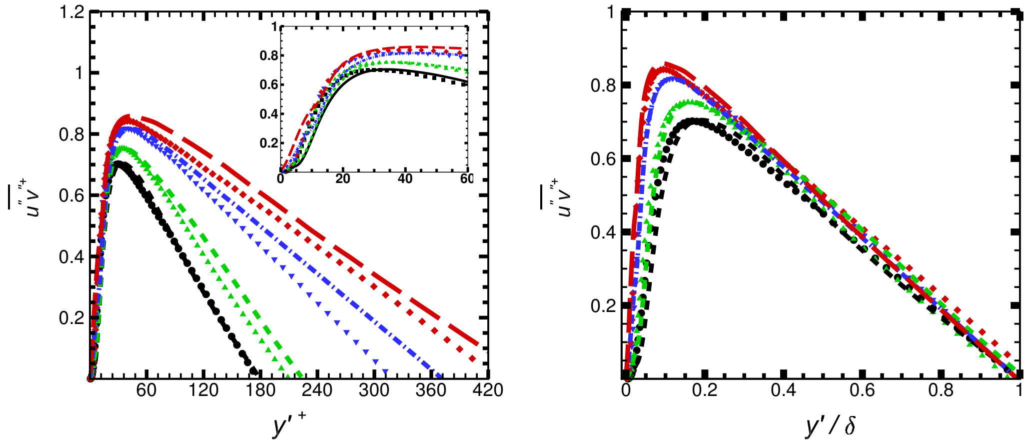

(a) (b)

Figure 6.8: Spatially-averaged Reynolds shear stress for BS2800 (—), BS3500 (- -), BS5500 (-·-·-·-) and BS7400 (— —) compared to S2800 (●), S3500 (▲), S5500 (▼) and S7400 (♦). The distance from the wall in (a) wall coordinates: y'^+ (b) global coordinates: y'/δ.

surface on the vorticity profile is noticed in the region $y'^+ < 10$. For BS2800, the vorticity peak location is shifted from $y'^+ = 0$ for S2800 to $y'^+ = 4$ which is below the roughness crest. Afterwards, a drop in the vorticity is noticed and the profile is similar to S2800. For BS3500, the profile exhibits the same behaviour both within the roughness crest and in the area beyond the roughness element. For BS3500, the increase in the Reynolds number does not affect the vorticity profile significantly compared to BS2800.

For BS5500, an increase in the profile is noticed compared to BS2800 and BS3500. Also, the peak of the profile is shifted from the roughness base to above roughness crest. This indicates that as Reynolds number increases, the location of the maximum vorticity is shifted from below the roughness crest to above the roughness crest. Beyond $y'^+ = 20$, BS5500 profile is higher than S5500 unlike smaller Reynolds number cases where similarity is observed between the smooth and backswimmer cases. As the Reynolds number increases to BS7400, the location of the vorticity peak is shifted further from the roughness base compared to BS5500, the vorticity profile increases as well. Beyond the $y'^+ = 20$ BS7400 has the highest profile com-

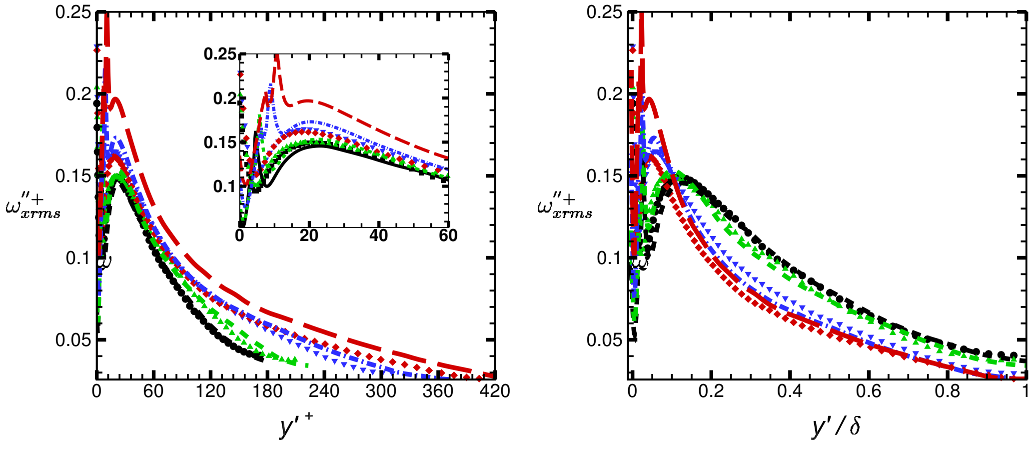

(a) (b)

Figure 6.9: Spatially-averaged r.m.s of streamwise fluctuating vorticity for BS2800 (—), BS3500 (- -), BS5500 (-·-·-·-) and BS7400 (— —) compared to S2800 (●), S3500 (▲), S5500 (▼) and S7400 (♦). The distance from the wall in (a) wall coordinates: $y^{'+}$ (b) global coordinates: $y^{'}/\delta$..

pared to BS2800, BS3500 and BS5500. Plotted against y'/δ, for $y'/\delta > 0.1$ the backswimmer profiles are very similar to the smooth channel profiles for all Reynolds numbers. For $y'/\delta < 0.1$ the vorticity profiles increase as Reynolds number increases.

For the r.m.s of wall-normal vorticity, the change in the vorticity profiles for the backswimmer cases compared to smooth channel is shown in Figure 6.10. For BS2800, an increase in the profile is noticed within the roughness element. Beyond the roughness crest, the vorticity profile decreases and it is similar to the smooth profile. For BS3500, similar behaviour is noticed compared to BS2800. As Reynolds number increases in BS5500 and BS7400, the magnitude of the maximum vorticity does not change significantly but the peak of the vorticity is shifted away from the roughness base as the Reynolds number increases. In the region $y^{'+} > 20$, the change in the Reynolds number becomes less significant on the change in the wall-normal vorticity. Plotted against y'/δ, for $y'/\delta > 0.1$ the backswimmer profiles are very similar to the smooth channel profiles at all Reynolds numbers. For $y'/\delta < 0.1$ the vorticity profiles are independent of the increase in the Reynolds numbers for the

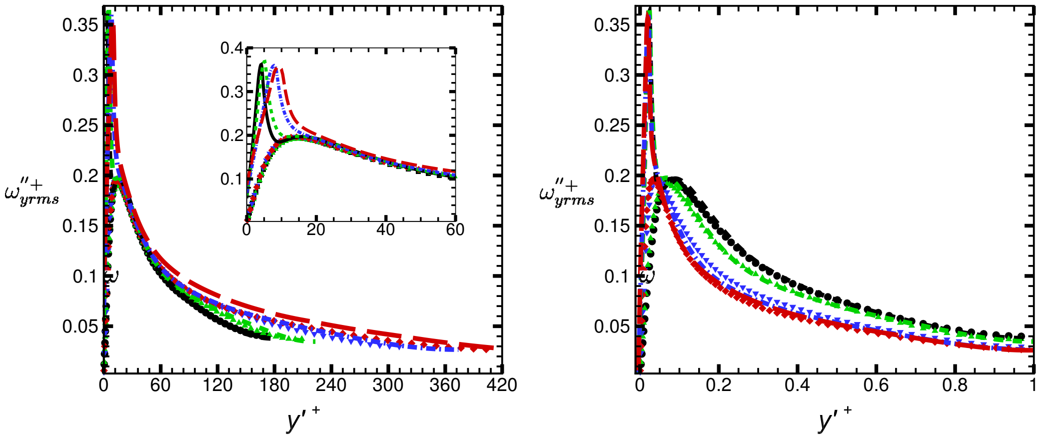

(a) (b)

Figure 6.10: Spatially-averaged r.m.s of wall-normal fluctuating vorticity for BS2800 (—), BS3500 (- -), BS5500 (-·-·-·-) and BS7400 (— —) compared to S2800 (●), S3500 (▲), S5500 (▼) and S7400 (♦). The distance from the wall in (a) wall coordinates: $y^{'+}$ (b) global coordinates: $y^{'}/\delta$.

backswimmer cases compared against each other.

The r.m.s of fluctuating vorticity in the spanwise direction is shown in Figure 6.11. Compared to the streamwise and the wall normal vorticity components the spanwise vorticity component has the highest profile within the roughness element. For $y^{'+} > 20$, all of the backswimmer cases exhibit similar profiles compared to each other and against their corresponding smooth cases. For $y^{'+} < 20$ BS2800 has the lowest profile, as Reynolds number increases the maximum vorticity increases and the location of the vorticity peak tends to move further from the roughness base. For all the backswimmer cases, the spanwise vorticity peak is higher than the smooth channel cases. Plotted against y'/δ, the change in spanwise vorticity profile is similar to the wall-normal component explained earlier.

6.8 Quadrant Analysis

The quadrant analysis for all backswimmer cases compared to smooth channel cases at different Reynolds numbers are presented in this section. The

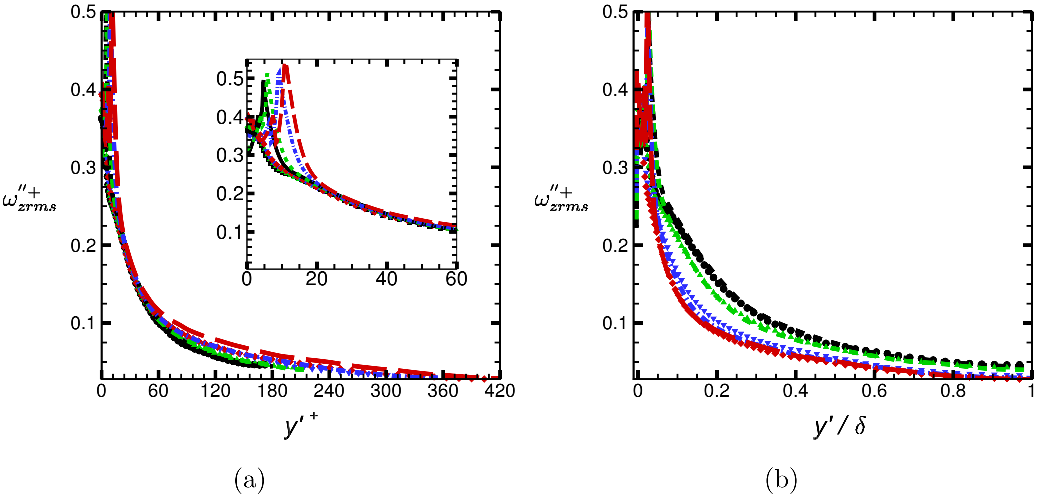

(a) (b)

Figure 6.11: Spatially-averaged r.m.s of spanwise fluctuating vorticity for BS2800 (—), BS3500 (- -), BS5500 (-·-·-·-) and BS7400 (— —) compared to S2800 (●), S3500 (▲), S5500 (▼) and S7400 (◆). The distance from the wall in (a) wall coordinates: y'^{+} (b) global coordinates: y'/δ.

four quadrants profile for every case is shown in Figure 6.12. For the case of the smooth channel flow the effect of increasing Reynolds numbers is as follows,

- The quadrant profiles are not significantly affected by the increase in the Reynolds number for all quadrants.
- The intersection point between Q2 and Q4 for the smooth channel cases is not significantly affected by the increase in Reynolds number.
- At all Reynolds numbers before the intersection point the dominance is for the sweep events and beyond that the dominance is for the ejection events.

For the backswimmer cases at different Reynolds numbers the change in the quadrant profiles is described as follows,

- Similar to smooth, Q4 sweep events are dominant before Q2/Q4 intersection point whereas beyond the intersection point Q2 events are dominant for all Reynolds numbers.

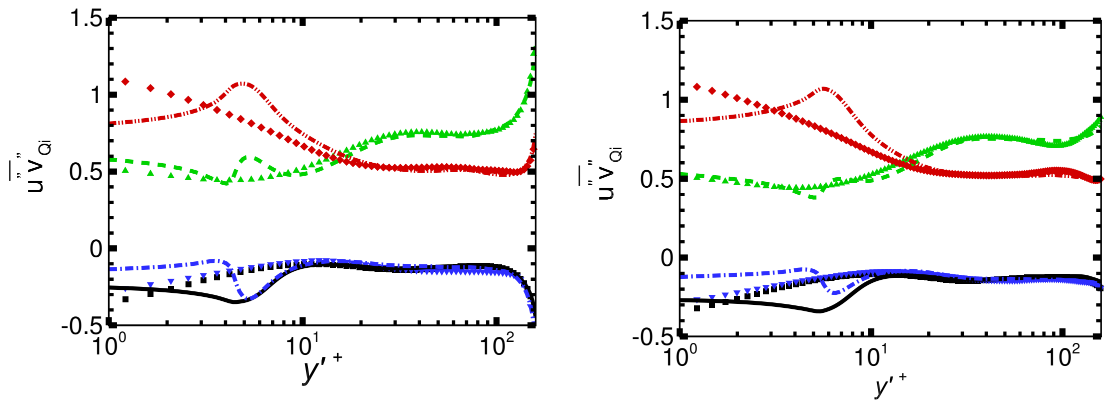

(a) $Re = 2800$ (b) $Re = 3500$

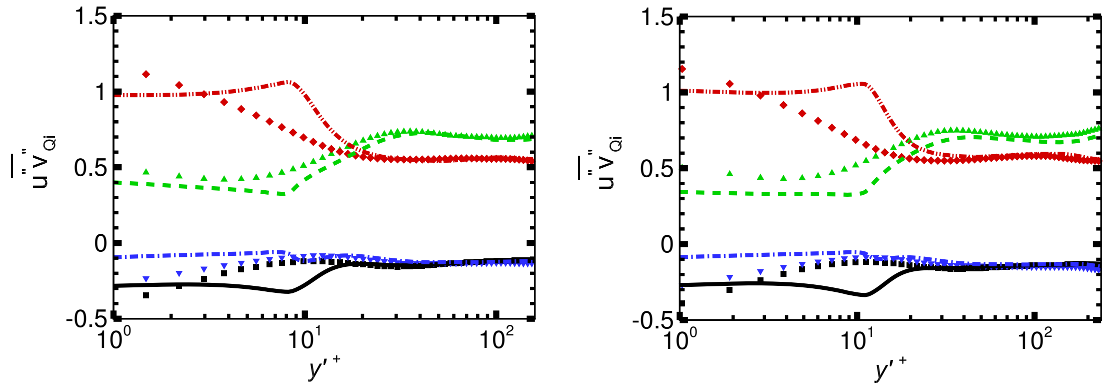

(c) $Re = 5500$ (d) $Re = 7400$

Figure 6.12: Quadrant analysis for smooth and backswimmer cases. Q1 BS(—), Q2 BS (- -), Q3 BS (-·-·-·) and Q4 BS (-··-··-) at all Reynolds numbers compared to Q1 S (■), Q2 S (▲), Q3 S (▼) and Q4 S (♦).

- Unlike smooth cases, as Reynolds number increases, Q2/Q4 intersection point is shifted away from the channel wall. For BS2800 and BS3500 the point is $y^{'+} \approx 12$. As Reynolds number increases for BS5500 and BS7400 the Q2/Q4 intersection point is $y^{'+} \approx 20$.

- At all Reynolds numbers, the effect of textured surface is more significant form the roughness base to the Q2/Q4 intersection point. Beyond this point, the effect of the textured surface is less significant and all quadrants exhibit a profile similar to smooth channel cases.

- For Q1, the increase in Reynolds number does not effect the outward activity significantly.

- For Q2, as Reynolds number increases, Q2 profile decreases. The decrease is for $y^{'+} < 12$ (BS2800 and BS3500) and for $y^{'+} < 20$ (BS5500 and BS7400).

- For Q3, the increase in the Reynolds number effect on inward event is more significant than Q1 particularly comparing cases BS2800 and BS3500. As Reynolds number increases in BS500 and BS7400 the change in Q3 event is less significant than for BS2800 and BS3500.

- For Q4, unlike Q2, as the Reynolds number increases the Q4 profile increases. Also, it is noticed that for the BS2800 and BS3500 cases the maximum profile occurs around $y^{'+} = 6$ and for BS5500 and BS7400 the maximum Q4 profile is shifted to $y^{'+} = 10$.

6.8.1 Intense Quadrants

The intensity of all quadrants at different Reynolds numbers compared to smooth channel at $H = 0$, $H = 3$ and $H = 6$ is shown in this section. For the smooth channel cases S2800, S3500, S5500 and S7400 the intense quadrants profile does not change significantly as Reynolds number increases. Overall, as H increases quadrant event decreases.

The increase of H effect on BS2800 is shown in Figure 6.13; compared to S2800, the outward interaction event (Q1) reduces for $y^{'+} < 2$, increases significantly for $2 < y^{+'} < 10$. For $50 < y^{+'} < 100$, BS2800 Q1 event slightly decreases. As H increases to $H = 3$ and $H = 6$, Q1 event reduces for $y^{'+} < 2$ and $2 < y^{+'} < 10$ compared to $H = 0$ but still exhibits the same behaviour compared to S2800. For $50 < y^{+'} < 100$, the profile is similar to S00.

For Q2, at $H = 0$, for $y^{'+} < 2$ the profile is similar to S2800, for $2 < y^{+'} < 10$ ejection event significantly increases. For $y^{'+} > 10$, the profile is similar to the S2800 case with minor discrepancies. At $H = 3$, for $y^{'+} < 2$, ejection events significantly increases compared to S2800 whereas for $2 < y^{+'} < 10$, ejection event reduces. For $y^{'+} > 10$ the profile is similar to S2800. At $H = 6$, for $y^{'+} < 10$ the behaviour is similar to S2800 case but for $20 < y^{+'} < 100$ Q2 event reduces compared to S00 and the discrepancy in the profile for this region is more significant than at $H = 0$ and $H = 3$.

The inward interaction event (Q3) significantly reduces for $y^{'+} < 2$ then significantly increases for $2 < y^{+'} < 10$. As H increases Q3 profiles decrease but exhibit the same profile compared to S2800. For $20 < y^{+'} < 100$ an increase in Q3 activity is noticed at $H = 0$ and $H = 3$ for BS2800 compared to S2800. At $H = 6$, both profiles are similar and very close to zero.

For Q4, at $H = 0$ compared to S2800, the sweep activity reduces for $y^{'+} < 5$, for $5 < y^{'+} < 15$ the sweep activity increases. For $y^{'+} > 15$, the profile is similar to S2800. As H increases sweep activity decreases however the behaviour does not significantly change compared to S2800. It is also noticed that at $H = 6$ for $y^{'+} < 5$ the sweep activity is the highest among all other quadrants.

The BS3500 change in intense quadrant analysis is shown in Figure 6.14. For Q1, BS3500 profiles at all H values is similar to B2800. For Q2 at $H = 0$, as Reynolds number increases for $y^{'+} < 2$ the profile reduces compared to BS2800 S3500 .For $2 < y^{+'} < 10$ Q2 event reduces compared to BS2800. At $H = 3$, for $y^{'+} < 2$ Q2 profile reduces compared to BS2800. For $2 < y^{+'} < 10$ the profile is similar to BS2800. At $H = 6$, the profile is similar to S3500 case.

Compared to BS2800, BS3500 inward interaction event (Q3) is not significantly changed for $y^{'+} < 2$. However, Q3 event, significantly increases for $2 < y^{+'} < 10$. For $y^{+'} > 10$, the profile is similar to S3500. At $H = 3$ both

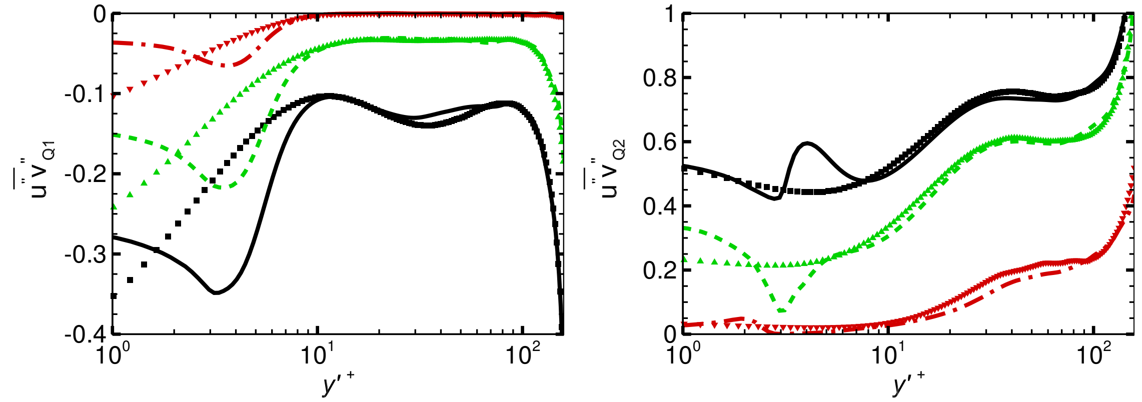

(a) Q1.

(b) Q2.

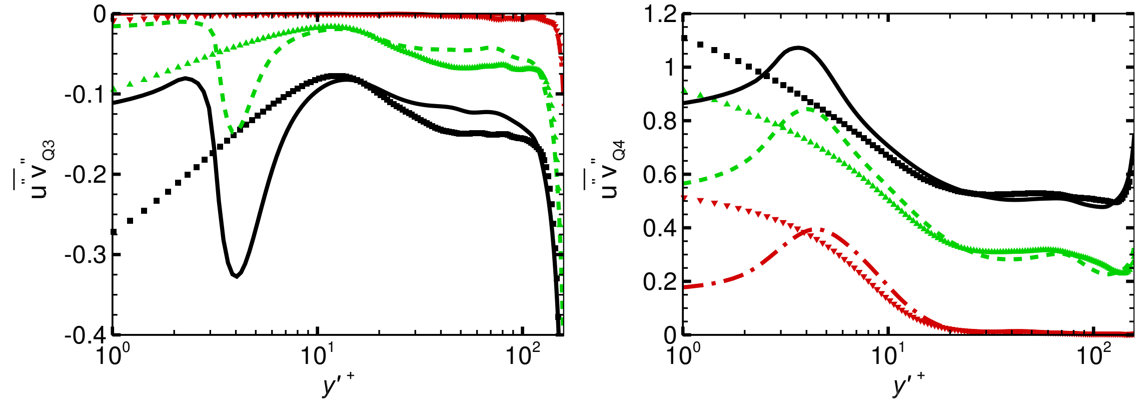

(c) Q3.

(d) Q4.

Figure 6.13: Intense Quadrants for smooth and backswimmer cases at $Re = 2800$. $H = 0$ BS (—) , $H = 3$ BS (- -), $H = 6$ BS (-·-·-·-) and $H = 0$ S (■), $H = 3$ S (▲), $H = 6$ S (▼) .

BS3500 and S3500 Q3 event reduces, however, their does not change significantly compared to each other. At $H = 6$ the profile is similar to S3500. For Q4, the sweep event exhibits a behaviour similar to the BS2800 for $y^{'+} < 5$, $5 < y^{'+} < 15$ and $y^{'+} > 15$ at all H.

As Reynolds number increases to $Re = 5500$ shown in Figure 6.15 for Q1, the increase in Reynolds number does not affect the profile compared to BS2800 and BS3500. For Q2, ejection event reduces for $1 < y^{+'} < 15$. For $y^{+'} > 15$, the flow is similar to S00. At $H = 3$ Q2 behaviour is similar to $H = 0$ apart from the event being reduced. Unlike BS2800 and BS3500, Q2 event does not exhibit any increase along the whole channel instead it is significantly reduces compared to S5500.

For Q3, at $H = 0$, for $y^{+'} < 8$ the inward interaction activity significantly decreases and for $8 < y^{+'} < 12$ Q3 event slightly increases. Afterwards, for $y^{+'} > 12$, Q3 profile slightly decreases compared to S5500. At $H = 3$, No significant increase is noticed along the BS5500 Q3 profile compared to S5500. Q3 event significantly decreases for $y^{+'} < 10$ while for $y^{+'} > 10$, the decrease is less significant and the profile is similar to the S5500 case. At $H = 6$ the profile is similar to BS2800 and BS3500 cases described earlier. For Q4, at $H = 0$, $H = 3$ and $H = 6$, for $y^{'+} < 5$, although sweep activity reduces compared to S5500, it increases when compared to Q4 profile for BS2800 and BS3500. for $5 < y^{'+} < 15$ the profile is similar to BS2800 and BS3500 and $y^{'+} > 15$ the profile similar to S5500 case.

The BS7400 change in intense quadrant analysis is shown in Figure 6.16. Q1 profile is similar to BS2800, BS3500 and BS5500. For Q2, significant decrease in ejection event is noticed along the channel compared against S7400. The reduction in ejection events is noticed at every H value including $H = 6$.

For Q3, at $H = 0$ BS7400 inward interaction event significantly increases for $y^{+'} < 10$. For $y^{+'} > 10$ the increase in Q3 event is as not as significant as for $y^{+'} < 10$ compared to S7400. At $H = 3$ an increase in Q3 event is noticed for $y^{+'} < 50$, afterwards, the profile is similar to S7400. At $H = 6$ the profile is similar to S7400 and is very close to zero.

For Q4, at $H = 0$, $H = 3$ and $H = 6$ BS7400 has the most sweep activity compared to all backswimmer cases for $y^{+'} < 10$. For $5 < y^{'+} < 30$ the

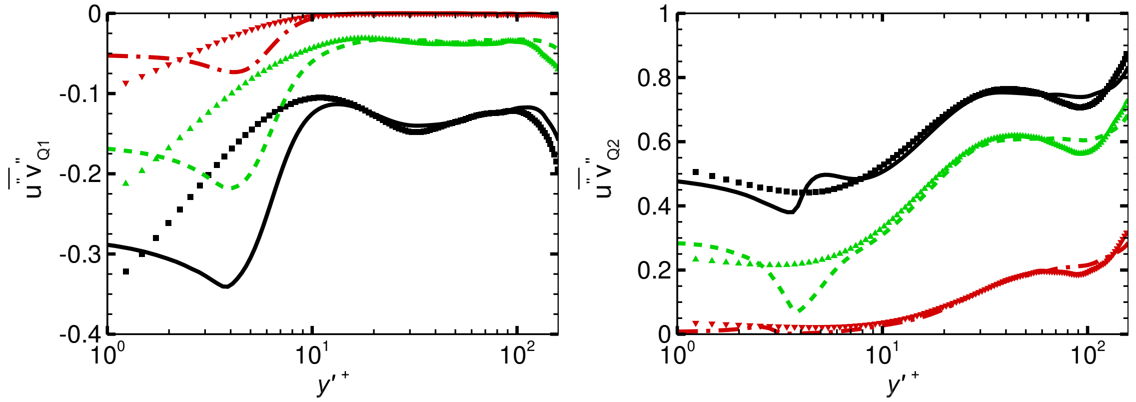

(a) Q1.

(b) Q2.

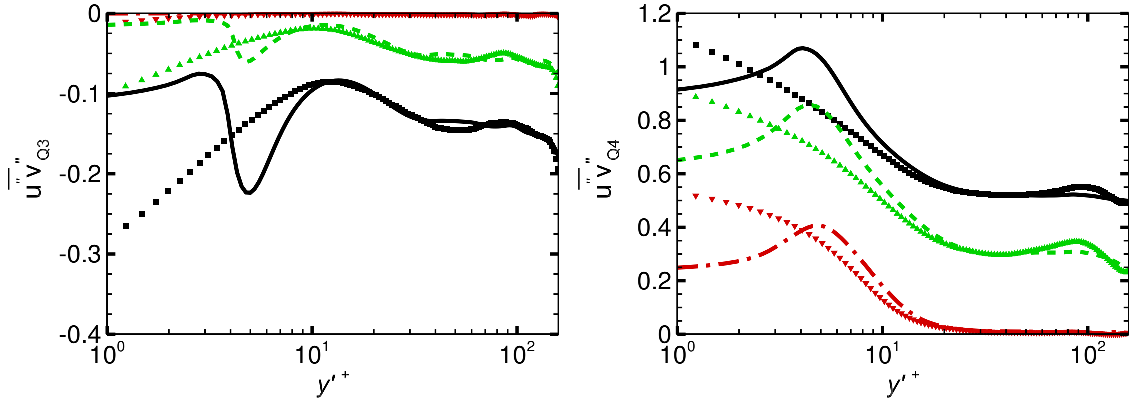

(c) Q3.

(d) Q4.

Figure 6.14: Intense Quadrants for smooth and backswimmer cases at $Re = 3500$. $H = 0$ BS (—) , $H = 3$ BS (- -), $H = 6$ BS (-·-·-·-) and $H = 0$ S (■), $H = 3$ S (▲), $H = 6$ S (▼).

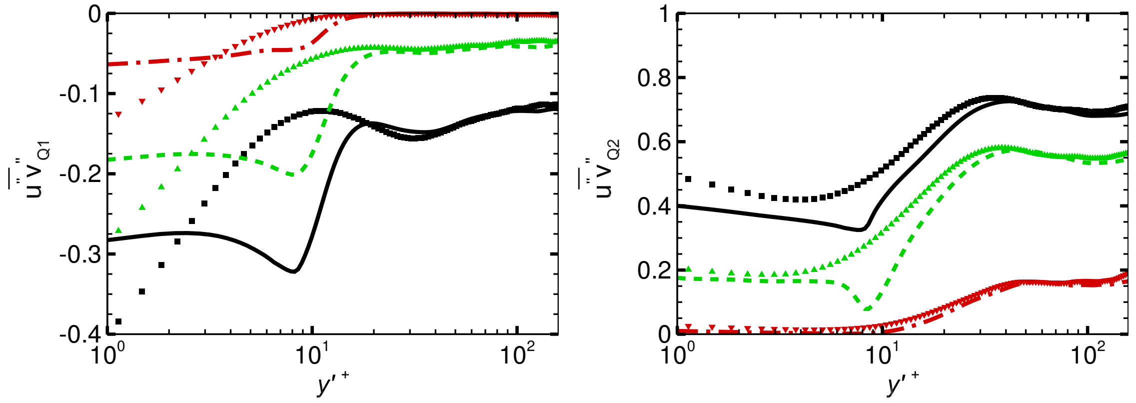

(a) Q1. (b) Q2.

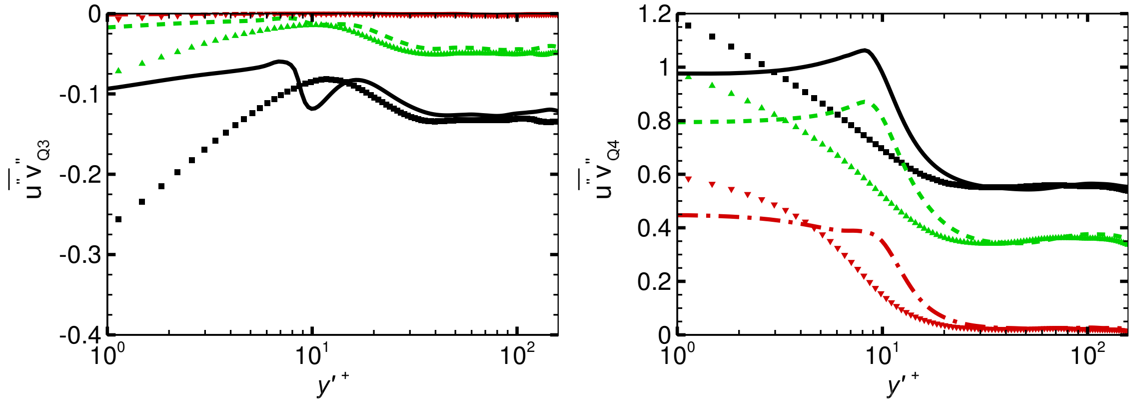

(c) Q3. (d) Q4.

Figure 6.15: Intense Quadrants for smooth and backswimmer cases at $Re = 5500$. $H = 0$ BS (—) , $H = 3$ BS (- -), $H = 6$ BS (-·-·-·-) and $H = 0$ S (■), $H = 3$ S (▲), $H = 6$ S (▼).

profile is similar to BS2800 and BS3500 and $y'^{+} > 30$ the profile similar to S7400 case. Although similarities are noticed for both Q2 and Q4 profiles at different Reynolds numbers further investigations are required to understand the change in Reynolds number effect on ejection and sweep events(See Figures 6.17 - 6.18).

In terms of drag performance, in previous literature (Jelly et al. [5], Viswanath [3] and Wallace. [73]), it was noticed that a drag reducing geometry exhibits a decrease in ejection and sweep events. For the case of backswimmer geometry, the change in ejection motion at $H = 0$ and $H = 6$ which represents the least and most intense motions, respectively, shown in Figure 6.17. As Reynolds number increases, for the backswimmer cases Q2 profile decreases at $H = 0$. For $H = 6$, the decrease in the profile is still there, however, the changes in the profile are less significant and the profile looks similar to smooth channel flows. This is not the case for the sweep profiles shown in Figure 6.18. The sweep activity significantly increases as Reynolds number increases. At $H = 6$ which represents the most intense Reynolds shear stress component compared to smooth channel flow, a significant increase in the profile is noticed. As Reynolds number increases, the maximum sweep location tends to shift away from the channel wall compared to the smaller Reynolds number cases B2800 and BS3500. In order to achieve an improvement in the drag performance, flow alterations are required to specifically decrease the sweep activity specially up to $y^{+'} = 20$.

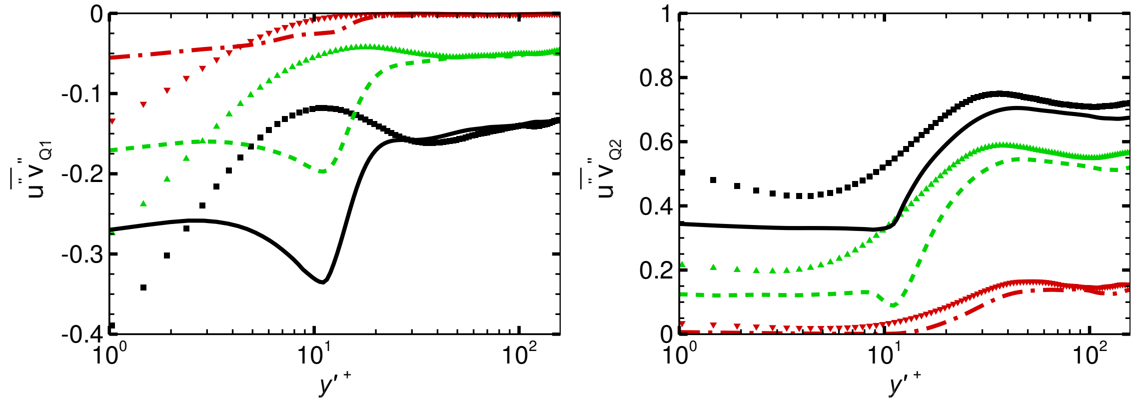

(a) Q1.

(b) Q2.

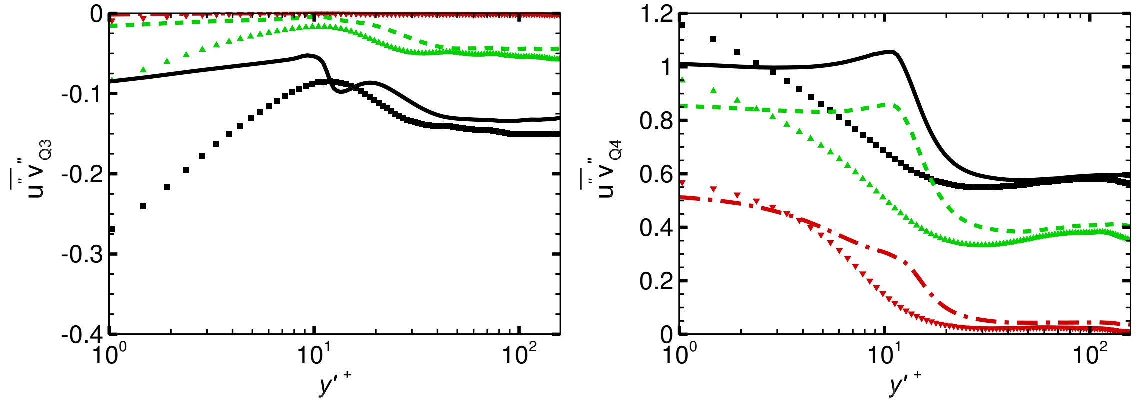

(c) Q3.

(d) Q4.

Figure 6.16: Intense Quadrants for smooth and backswimmer cases at $Re = 7400$. $H = 0$ BS (—) , $H = 3$ BS (- -), $H = 6$ BS (-·-·-·-) and $H = 0$ S (■), $H = 3$ S (▲), $H = 6$ S (▼).

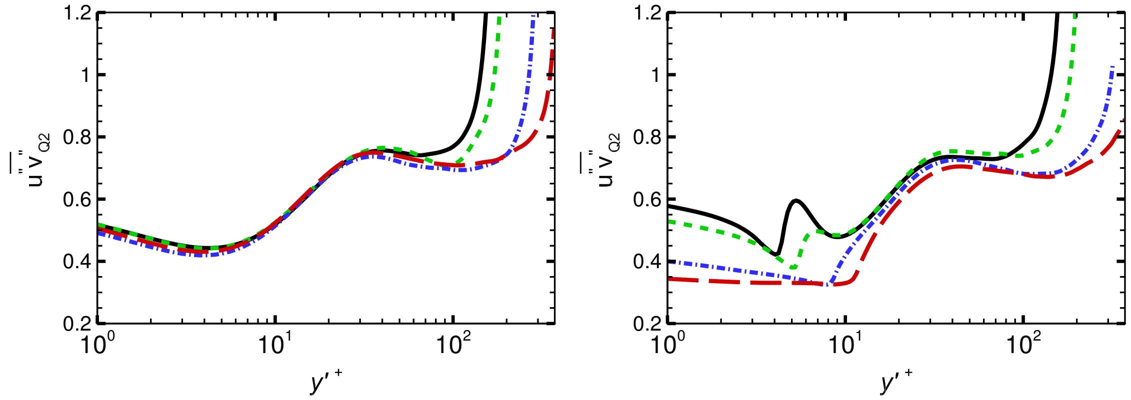

(a) Q2 $H = 0$ smooth

(b) Q2 $H = 0$ backswimmer

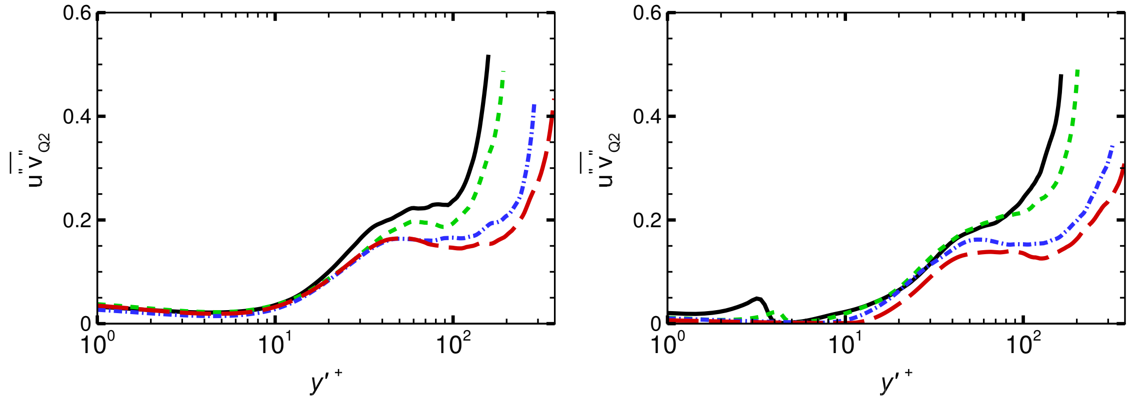

(c) Q2 $H = 6$ smooth

(d) Q2 $H = 6$ backswimmer

Figure 6.17: Q2 profiles at $H = 0$ and $H = 6$ where $Re = 2800$ (—) , $Re = 3500$ (- -), $Re = 5500$ (-·-·-) and $Re = 7400$ (— —).

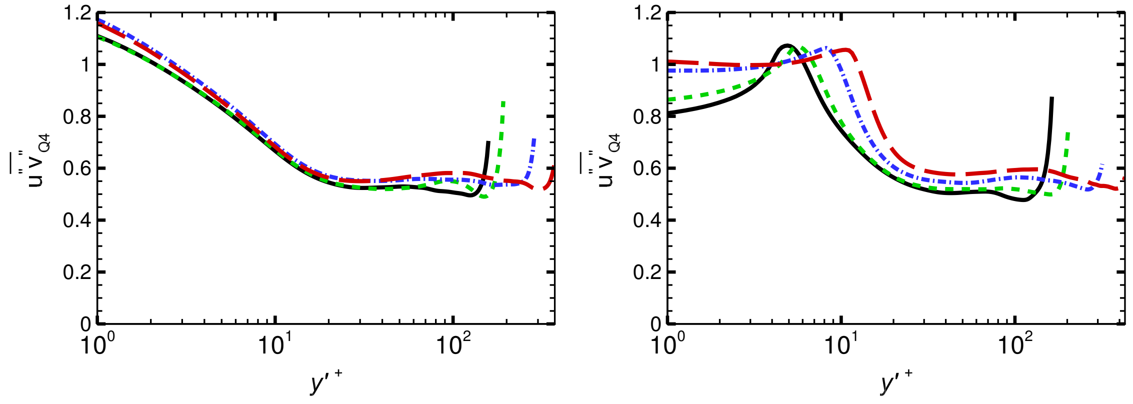

(a) Q4 $H = 0$ smooth

(b) Q4 $H = 0$ backswimmer

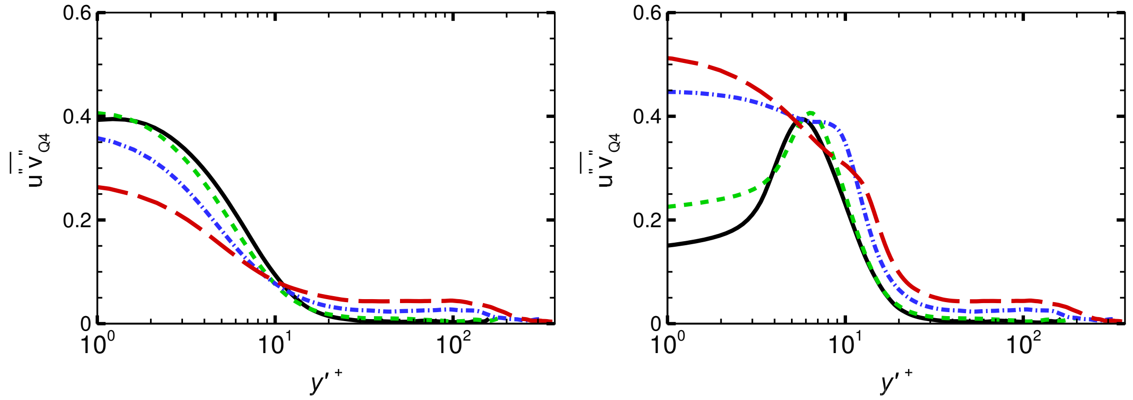

(c) Q4 $H = 6$ smooth

(d) Q4 $H = 6$ backswimmer

Figure 6.18: Q4 profiles at $H = 0$ and $H = 6$ where $Re = 2800$ (—) , $Re = 3500$ (- -), $Re = 5500$ (-·-·-·) and $Re = 7400$ (— —).

6.9 Flow Visualisations

To understand the effect of using backswimmer geometry on turbulent flow, the flow structure by means of fluctuating velocities and the second largest Eigen value of symmetric tensor λ_2 iso-surfaces by Jeong and Hussain [6] are used for all backswimmer cases at all Reynolds numbers. Similar to chapter 5, all 3D iso-surfaces in this section are instantaneous and captured at different time steps after the flow was fully developed (each with $\Delta t^+ \approx 100$ apart). Also, all of the 3D plots present the changes in u'^+ and λ_2 for $0 < y/\delta < 0.04$ which is from the channel wall until just above the roughness crest.
From BS2800 3D plots shown in Figure 6.19 at different instants the flow can be described as follows,

- The low-speed streaks are present around the roughness elements specially on the roughness crest and in the region separating the roughness elements in the streamwise direction.
- The high-speed streaks are present in the region separating the roughness elements in the spanwise direction.
- λ_2 streaks are present within the roughness elements and exhibit sparse shape.

From BS3500 3D plots shown in Figure 6.20 at different instants the flow can be described as follows,

- The low-speed streaks' width and intensity decreases as Reynolds number increases compared to BS2800.
- The high-speed streaks width increases whereas the distribution is not significantly affected compared to BS2800.
- λ_2 streaks are present within the roughness elements and exhibit sparse shape and increases compared to BS2800. For this case some λ_2 streaks are formulated above the roughness crest.

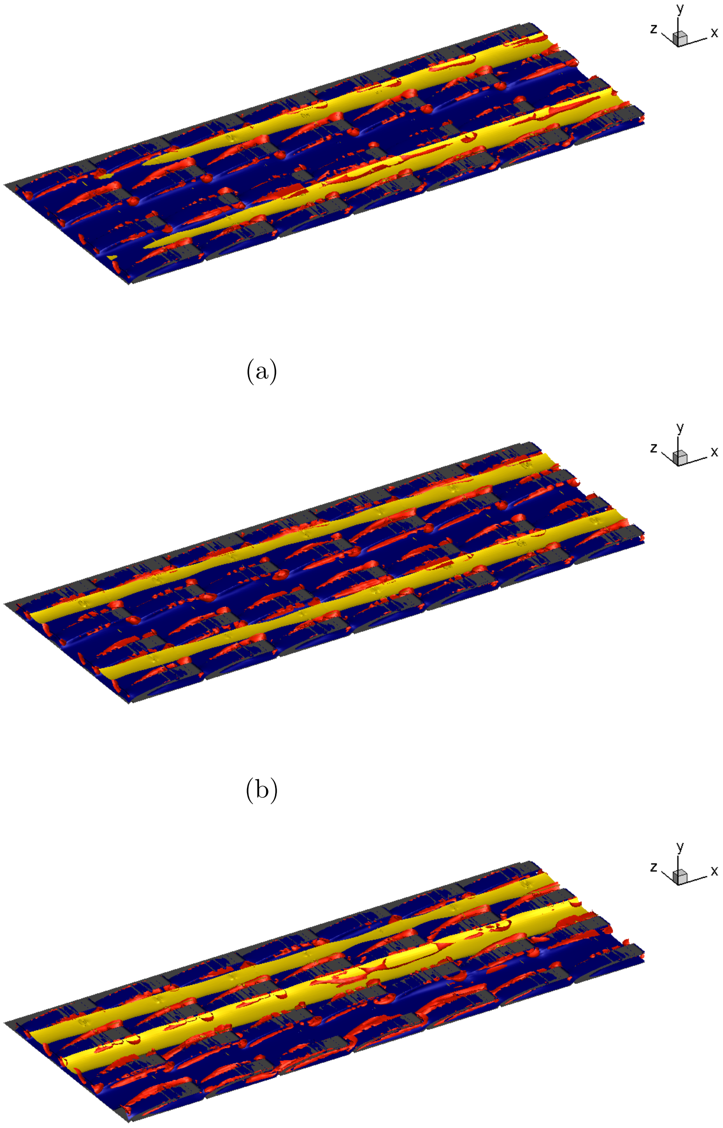

(a)

(b)

(c)

Figure 6.19: BS2800 iso-surface plots for low, high velocity streaks and λ_2 where blue $u'/u_\tau = -0.1$, yellow $u'/u_\tau = 3.0$ and red $\lambda_2/(u\tau/\delta) = -0.002$ for part of the computational domain in the streamwise and spanwise directions at three time instants (each with $\Delta t^+ \approx 100$).

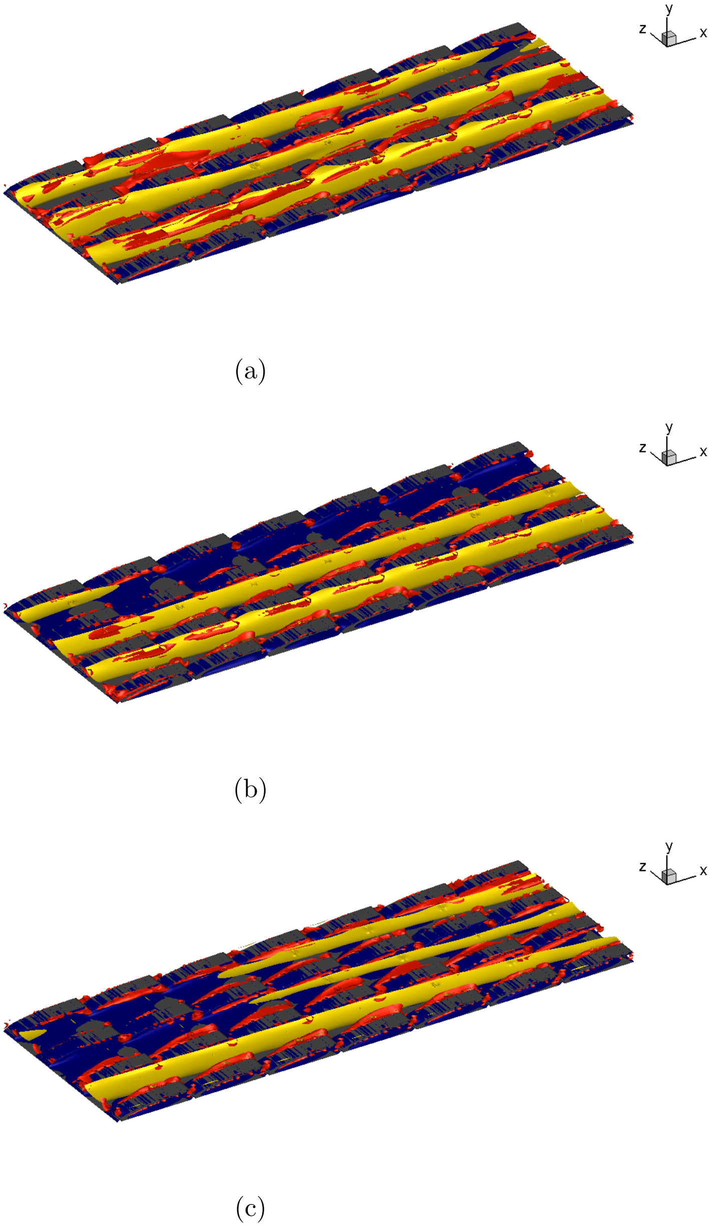

Figure 6.20: BS3500 iso-surface plots for low, high velocity streaks and λ_2 where blue $u'/u_\tau = -0.1$, yellow $u'/u_\tau = 3.0$ and red $\lambda_2/(u\tau/\delta) = -0.002$ for part of the computational domain in the streamwise and spanwise directions at three time instants (each with $\Delta t^+ \approx 100$).

From BS5500 3D plots shown in Figure 6.21 at different instants the flow can be described as follows,

- The low-speed streaks' width and distribution significantly decreases compared to BS2800 and BS3500 and only present within the roughness element
- The high-speed streaks' increases compared to the low-speed streaks and all the previous cases.
- λ_2 streaks' intensity increases in the region below the roughness crest and the region above the roughness crest compared to BS3500 and BS2800 cases.

From BS7400 3D plots shown in Figure 6.19 at different instants the flow can be described as follows,

- The low-speed streaks width and distribution have the least width and intensity compared to all the previous cases.
- The high-speed streaks are the most intense and the widest compared to all the cases.
- λ_2 streaks' has the most intensity compared against all the previous cases, and the highest intensity is noticed above the roughness crest compared to within the roughness crest.

The flow structure around one roughness element using phase-averaging is shown in Figures 6.23, 6.24, 6.25 and 6.26 at all Reynolds numbers. For BS2800 Figure 6.23, below the roughness elements, low and high fluctuating velocity streaks u'^{+} are present. As Reynolds number increases for BS3500 Figure 6.24, the width and intensity of the low-speed streaks decreases. As Reynolds number increases for BS5500 Figure 6.25 , the high-speed streaks, width and distribution increases, within the roughness element and at the roughness crest. In terms of λ_2, as Reynolds number increases, the intensity of the elements significantly increases. For BS7400 Figure 6.26, a significant increase in λ_2 is noticed specially within the roughness elements.

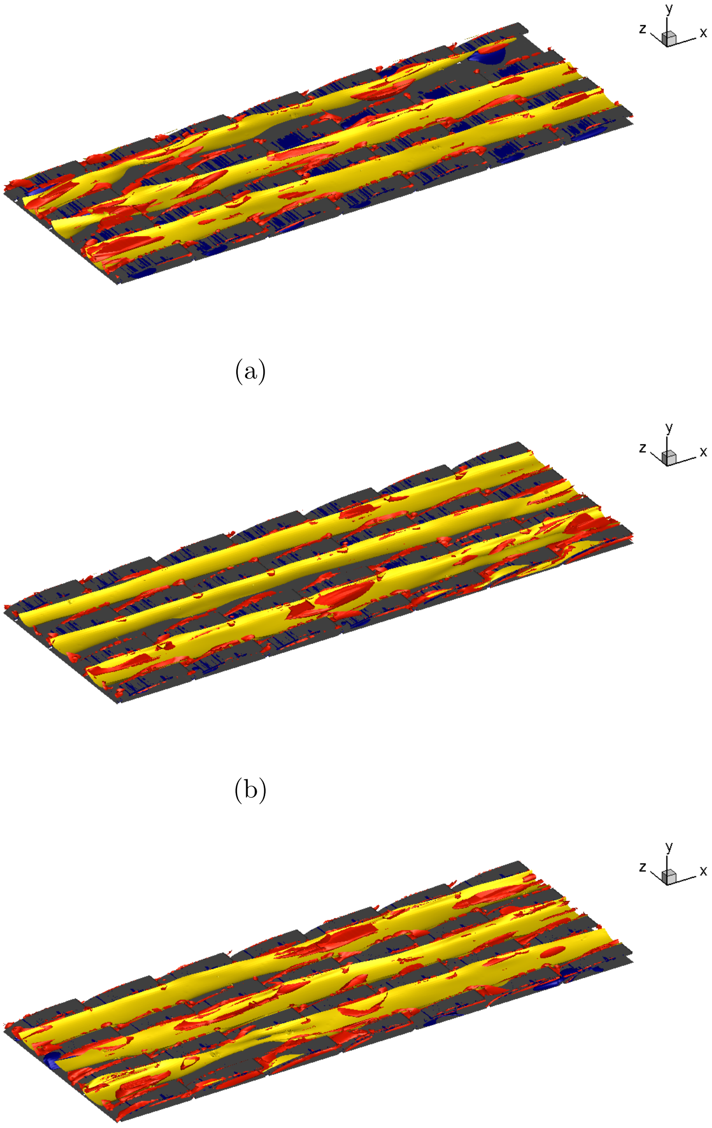

(a)

(b)

(c)

Figure 6.21: BS5500 iso-surface plots for low, high velocity streaks and λ_2 where blue $u'/u_\tau = -0.1$, yellow $u'/u_\tau = 3.0$ and red $\lambda_2/(u\tau/\delta) = -0.002$ for part of the computational domain in the streamwise and spanwise directions at three time instants (each with $\Delta t^+ \approx 100$).

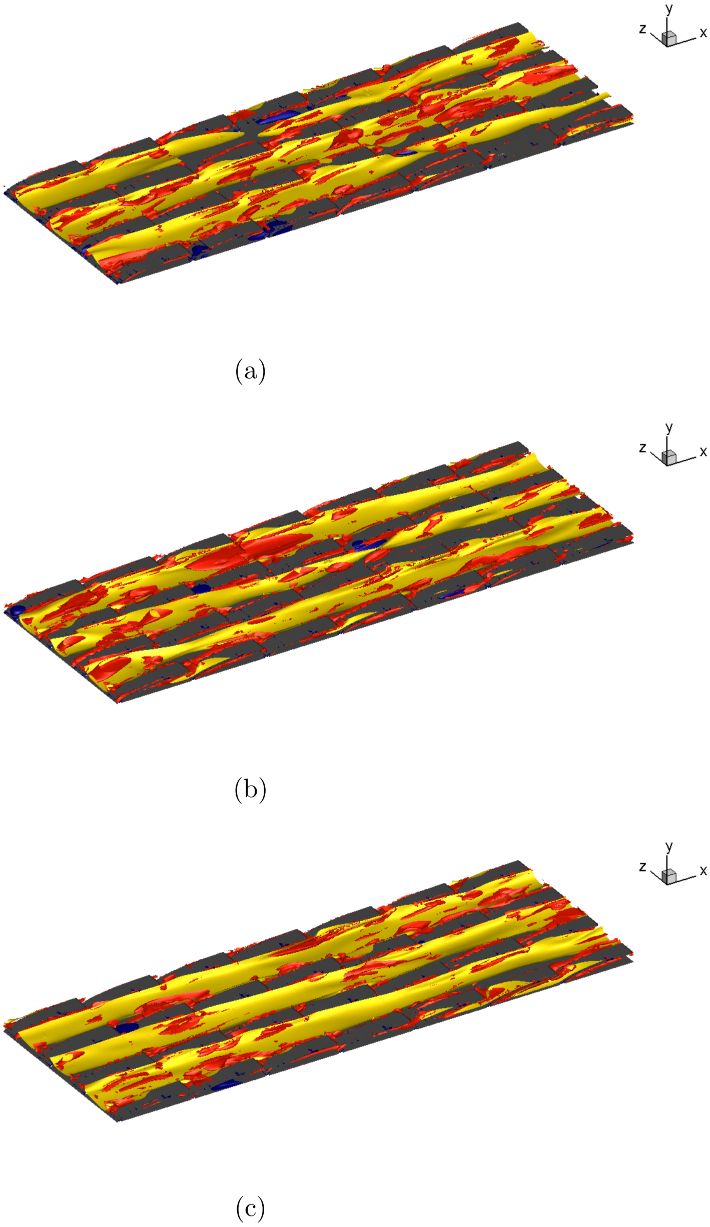

(a)

(b)

(c)

Figure 6.22: BS7400 iso-surface plots for low, high velocity streaks and λ_2 where blue $u'/u_\tau = -0.1$, yellow $u'/u_\tau = 3.0$ and red $\lambda_2/(u\tau/\delta) = -0.002$ for part of the computational domain in the streamwise and spanwise directions at three time instants (each with $\Delta t^+ \approx 100$).

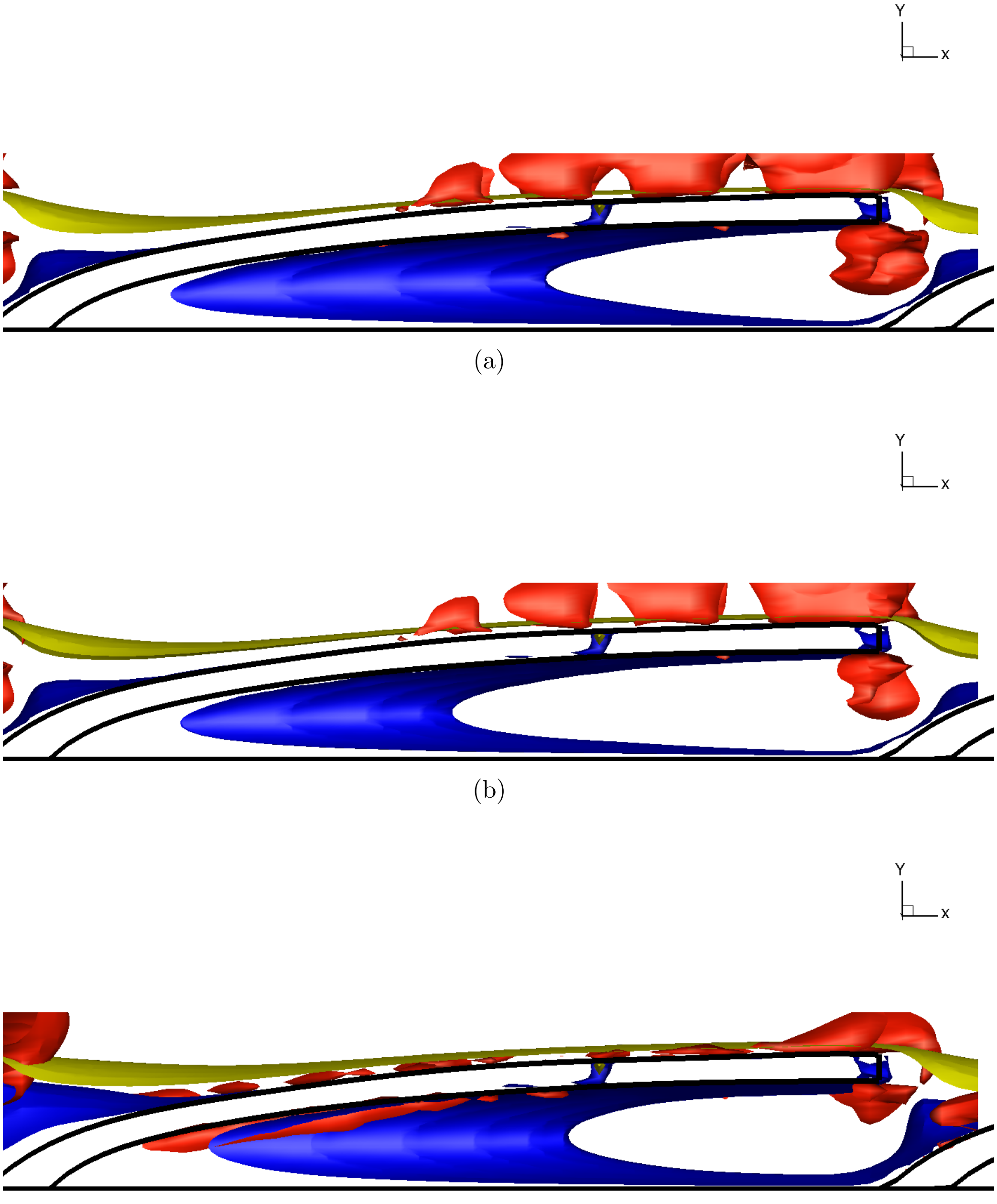

(a)

(b)

(c)

Figure 6.23: BS2800 iso-surface plots for low, high velocity streaks and λ_2 where blue $u'/u_\tau = -0.12$, yellow $u'/u_\tau = 0.5$ and red $\lambda_2/(u\tau/\delta) = -0.002$ for one roughness element at three time instants (each with $\Delta t^+ \approx 100$).

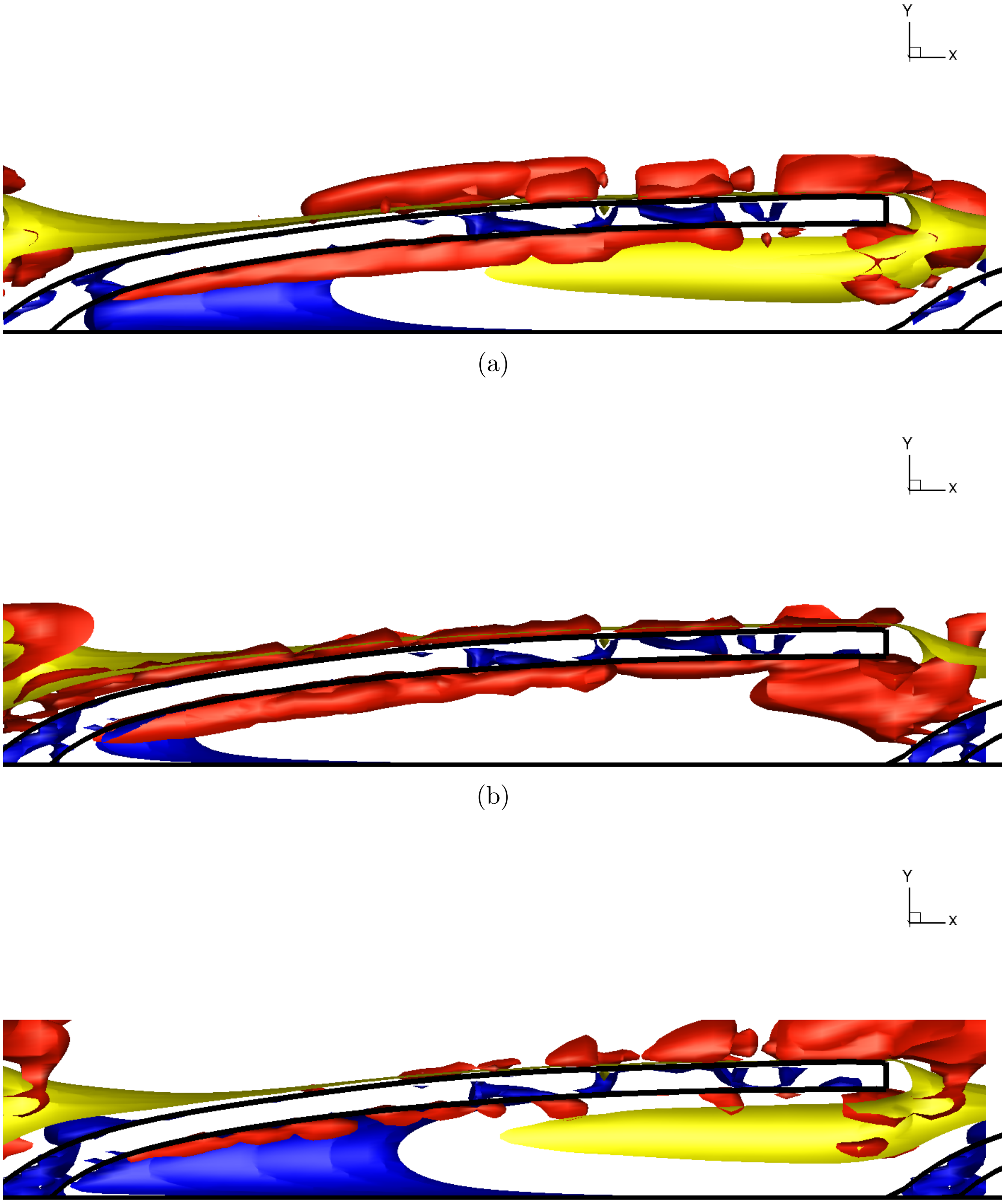

(a)

(b)

(c)

Figure 6.24: BS3500 iso-surface plots for low, high velocity streaks and λ_2 where blue $u'/u_\tau = -0.12$, yellow $u'/u_\tau = 0.5$ and red $\lambda_2/(u\tau/\delta) = -0.002$ for one roughness element at three time instants (each with $\Delta t^+ \approx 100$).

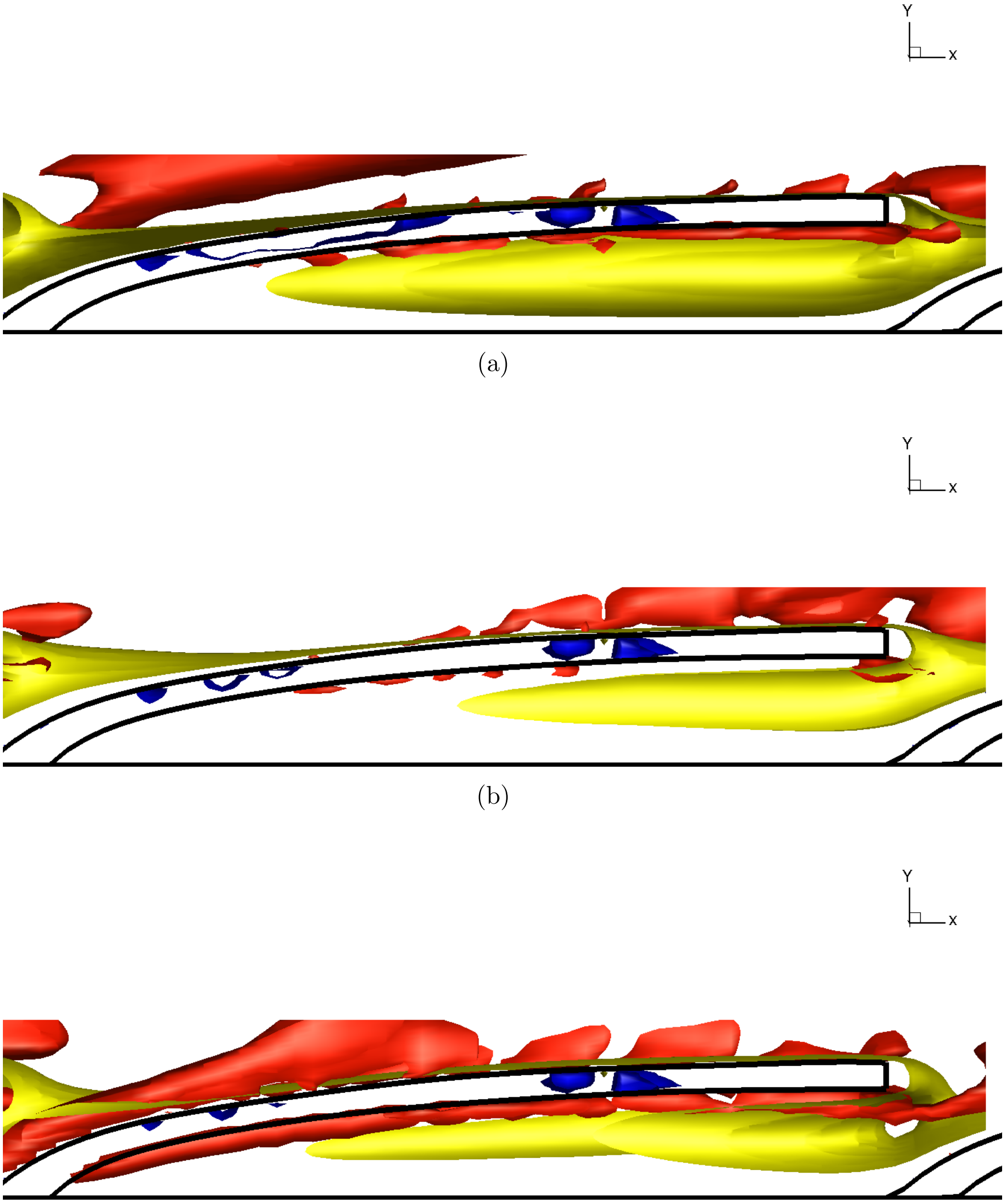

(a)

(b)

(c)

Figure 6.25: BS5500 iso-surface plots for low, high velocity streaks and λ_2 where blue $u'/u_\tau = -0.12$, yellow $u'/u_\tau = 0.5$ and red $\lambda_2/(u\tau/\delta) = -0.002$ for one roughness element at three time instants (each with $\Delta t^+ \approx 100$).

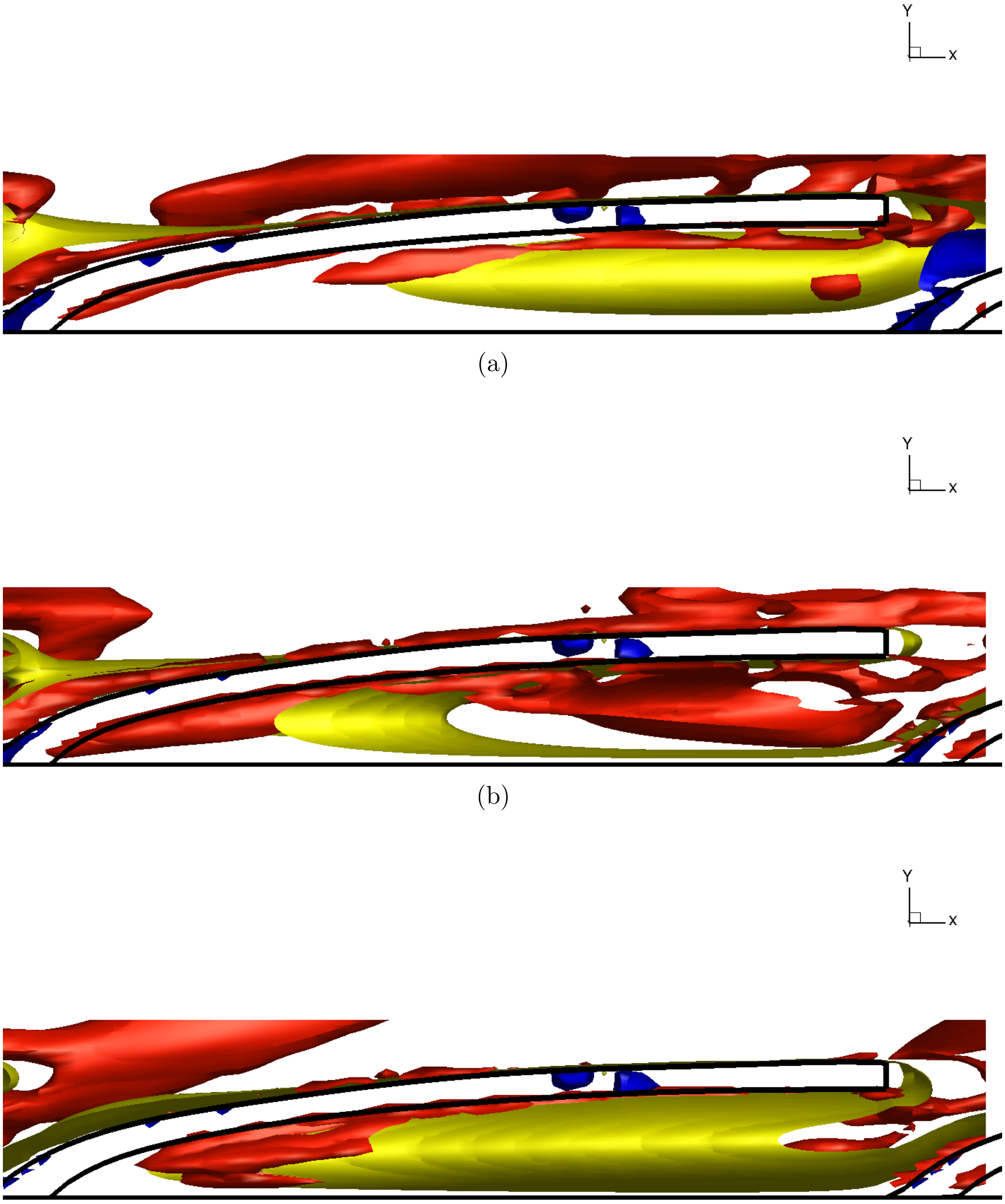

(a)

(b)

(c)

Figure 6.26: BS7400 iso-surface plots for low, high velocity streaks and λ_2 where blue $u'/u_\tau = -0.12$, yellow $u'/u_\tau = 0.5$ and red $\lambda_2/(u\tau/\delta) = -0.002$ for one roughness element at three time instants (each with $\Delta t^+ \approx 100$).

Chapter 7

Conclusions and Future Work

7.1 Conclusions

The main purpose of the present research was to understand the behaviour of turbulent flow and drag performance over a backswimmer-inspired textured surface. Numerical simulations have been undertaken using an in-house Direct Numerical Simulations code, CHAPSim. The research was mainly looking at addressing two major questions: (i) Whether or not the backswimmer geometry is a drag reducing texture? (ii) What is the flow behaviour and turbulent structure particularly around the textured elements?

The DNS code has been adopted for (i) including a hybrid MPI/OMP parallelization resulting in a better performance for the solver, (ii) treating the new texture geometry by writing associated subroutines. Two aspects have been focused on for the study: (i) effect of the geometrical change of the texture element, (ii) effect of varying Reynolds number, where the geometry parameters remain unchanged.

In terms of the geometry shape, the most distinctive difference between the backswimmer geometry and the previously examined geometric riblets and posts was the presence of the region below the roughness crest where the velocity and pressure components were not forced to be zero.

The Backswimmer geometry implementation was done using the Immersed Boundary Method to the in-house DNS CFD code CHAPSim. To ensure accurate representation of the geometry and the non-zero velocity region below it, a large number of points specially in the streamwise and wall-normal directions was required. One challenge for implementing the backswimmer geometry was to accurately replicate the geometry while avoid using extra fine meshes specially for low Reynolds number simulations. Using the minimal channel approach by Chung et al. [70], significantly reduced computational time and cost for all the simulated test cases.

In addition to the geometry shape, the 1D decomposition for the in-house CFD code made the tasks more challenging as the number of the simulation cores was constrained by the number of mesh points in the wall-normal direction while the finer mesh was required in the streamwise direction.

7.1.1 Effect of Geometrical Change on the Backswimmer Cases.

To understand the effect of geometrical changes on the backswimmer cases three test cases with the same Reynolds bulk ($Re = 2800$) and roughness height ($h/\delta = 0.03$), but different width-to-height ratios have been studied. In the streamwise direction the width-to-height ratios were 0.0 and 0.125 and in the spanwise direction were 2.0 and 1.0.

The drag reduction is inversely proportional to the streamwise width-to-height ratio. In other words, as the number of roughness elements increases in the streamwise direction (i.e. decrease w_x/h) the backswimmer drag performance tends to improve. Moreover, the following can be concluded as w_x/h decreases:

- Spatially-averaged velocity profile increases and the value of ΔU^+ decreases
- A decrease in the spatially averaged r.m.s of streamwise fluctuating velocity specially for $y'^+ < 40$ compared to smooth channel case
- Presence of low-speed regions in the area separating roughness elements in the streamwise direction

- Insignificant change in ejection and sweep events
- The width of the high- and low- speed streaks decreases
- Slight decrease in the intensity of λ_2 streaks specially at the roughness crest

The drag performance is directly proportional to the spanwise width-to-height ratio. In other words, as the number of roughness elements increased in the spanwise direction the DR (negative value) increased which yields to drag increase. Moreover, the following can be concluded as w_z/h decreases compared to the cases where w_x/h decreased:

- Increase in the r.m.s of streamwise velocity profile, wall-normal, spanwise fluctuating velocity profiles and Reynolds shear stress
- Decrease of low-speed regions within the roughness elements and between the roughness elements
- An increase in the Reynolds shear stress profile
- Significant decrease in ejection and sweep events for $y^{'+} < 3$ then increase for $3 < y^{'+} < 10$

The root-mean-square of fluctuating vorticity profiles were not significantly affected by varying the texture geometry parameters. In all directions within the roughness height, the profiles exhibited a significant increase compared to smooth channel flow and afterwards decreased to match the smooth case profiles.

7.1.2 Effect of Changing the Reynolds Number on the Backswimmer Geometry Textured Surfaces

In order to investigate the effect of changing Reynolds numbers on backswimmer textured surface, simulations were conducted at $Re = 2800, 3500, 5500$ and 7400. The width-to-height ratio in the streamwise direction was set to zero and in the spanwise direction equal to 2. For different Reynolds numbers, the flow over the backswimmer texture surface can be divided into two groups: (i) smaller Reynolds numbers which include BS2800 and BS3500 cases and (ii) higher Reynolds numbers which include BS5500 and BS7400 cases.

For the smaller Reynolds numbers, in terms of the drag reduction, no drag reduction was obtained from these cases and the resulting total shear stress value was almost similar to the corresponding smooth channel flow with a maximum drag reduction below -3%.

In terms of turbulence statistics the low Reynolds number cases' behaviour is summarised as follows,

- The roughness function was in the transitional roughness regime and the effective roughness was at $k_s = 1.68h$ of the roughness height.
- The change in the spatially averaged velocity profiles, fluctuating velocity profiles, fluctuating vorticity profiles, Reynolds shear stress profiles and quadrant analysis were independent of the change in Reynolds numbers and exhibited a profile similar to their corresponding smooth channel profile which is consistent with the Moser et al. [16] findings.

For the higher Reynolds numbers, it was noticed that the drag increased by 28% compared to smooth channel flow

In terms of turbulence statistics, the high Reynolds number cases' behaviour is summarised as follows,

- The geometry origin for all Reynolds number cases is 0.025
- For the spatially averaged velocity profile the log-law intercept region downwards displacement significantly increased compared to smooth channel flow case
- A significant increase in the wall-normal and spanwise fluctuating velocity components was noticed
- Not much difference was seen for the r.m.s of the streamwise fluctuating velocity

- An increase in the vorticity profiles was noticed in this case compared to smooth channel flow specially in the streamwise direction. It was also noticed that the maximum vorticity location was shifted away from the roughness base compared to the lower Reynolds number cases.
- As Reynolds number increases, the ejection events decrease and sweep events increase for all backswimmer cases.

As Reynolds number increases, the width and the intensity of the low-speed streaks decreases. The intensity and width of the high-speed streaks significantly increase. In terms of λ_2, the intensity of the elements significantly increases as Reynolds number increases specially beyond the roughness crest for the higher Reynolds numbers.

7.2 Future Work

As mentioned earlier, this work presented a novel numerical implementation for the Backswimmer geometry. That being said, there is still a high potential of development and a large number of questions to be investigated and addressed. The future work suggestions include the following,

(i) The implementation of 2D decomposition instead of the currently used 1D to improve the code scalability and linking the number of cores used to the number of mesh cells in the streamwise direction.

(ii) Parallelize the modernized postprocess CHAPSim serial version to optimize the code performance over multiple processors and specially while generating 3D contour and iso-surface plots.

(iii) Run cases for Reynolds numbers higher than $Re = 7400$ once points (i) and (ii) are addressed to calculate the effective roughness height in the fully rough regime.

(iv) Validate the obtained results against physical experiment by running wind tunnel experiments on backswimmer textured surfaces.

(v) Study the effect of changing the backswimmer geometry specially the width-to-height ratios at higher Reynolds numbers.

(vi) Extend the phase averaging to the current statistics and generate more higher-order statistics (e.g. budget terms, pressure distribution and spectral energy) to further investigate the detailed flow structure associated with the use of the backswimmer geometry.

(vii) Replicate backswimmer geometry presence in nature in terms of the elements alignment to be non-uniform in the streamwise and spanwise directions.

References

[1] J. D. Anderson. *Fundamentals of Aerodynamics*. McGraw-Hill, 2011.

[2] S. Zhang, M. Ochiai, Y. Sunami, and H. Hashimoto. Influence of microstructres on aerodynamic characteristics for dragonfly wing in gliding flight. *Journal of Bionic Engineering*, 16:432 – 431, 2019.

[3] P.R. Viswanath. Aircraft drag reudction using riblets. *Progress in Aerospace Sciences*, 39:571 – 600, 2002.

[4] Huub M Toussaint, Martin Truijens, Meint-Jan Elzinga, Ad Van de Ven, Henk de Best, Bart Snabel, and Gert de Groot. Swimming: Effect of a fast-skin body suit on drag during front crawl swimming. *Sports Biomechanics*, 1(1):1 – 10, 2002.

[5] T. O. Jelly, S. Y. Jung, and T. A. Zaki. Turbulence and skin friction modification in channel flow with streamwise-aligned superhydrophobic surface texture. *Physics of Fluids*, 26, 095102, 2014.

[6] J. Jeong and F. Hussain. On the identification of vortex. *Journal of Fluid Mechanics*, 285, 1995.

[7] M. B. Martell, J. B. Perot, and J. P. Rothstein. Direct numerical simulations of turbulent flows over superhydrophobic surfaces. *Journal of Fluid Mechanics*, 620:31 – 41, 2009.

[8] I. Arenas, E. Garcia, M. K. Fu, P. Orlandi, M. Hutmark, and S. Leonardi. Comparison between superhydrophobic, liquid infused and

rough surfaces: A DNS study. *Journal of Fluid Mechanics*, 869:500 – 525, 2019.

[9] D. Sassun, O. Flores, and P. Orlandi. Analysis and comparison between rough channel and pipe flows. *Journal of Physics: Conference Series*, 708, 2016.

[10] M. Itoh, S. Tamano, R. Iguchi, K. Yokota, N. Akino, R. Hino, and S. Kubo. Turbulent drag reduction by the seal fur surface. *Physics of Fluids*, 18:065102, 2006.

[11] G. DIEZ, M. Soto, and J. M. Blanco. Biological characterization of the skin of shortfin mako shark isurus oxyrinchus and preliminary study of the hydrodynamic behaviour through computational fluid dynamics. *Journal of Fish Biology*, 87:123 – 137, 2015.

[12] P. Ditsche-Kuru, E. S. Scneider, J. .E. Melskotte, M. Brede, A. Leder, and W. Barthlott. Superhydrophobic surfaces of the water bug notoncena glauca: A model for friction reduction and air retention. *Beilstein Journal of Nanotechnology*, 2:137–144, 2011.

[13] A. Boomsma and F. Sotiropoulos. Direct numerical simulation of sharkskin denticles in turbulent channel flow. *Physics of Fluids*, 28(3):035106, 2016.

[14] H. O. G. Benschop and W. P. Breugem. Drag reduction by herrinbone riblet texture in direct numerical simulations of turbulent channel flow. *Journal of Turbulence*, 18:717–759, 2017.

[15] J. Jimenez. Turbulent flows over rough walls. *Annual review fluid Mechanics*, 36:173 – 196, 2004.

[16] D. Moser, J. Kim, and N. N. Mansour. Direct numerical simulation of turbulent channel flow up to Re_τ=590. *Physics of Fluids*, 11 4:1 – 21, 1999.

[17] S. He and M. Seddighi. Turbulence in transient channel flow. *Journal of Fluid Mechanics*, 715:60 – 102, 2013.

[18] M. Seddighi. Study of turbulence and wall shear stress in unsteady flow over smooth and rough wall surfaces. *PhD Thesis, University of Aberdeen*, 2011.

[19] L. Nling and S. Laizet. 2DCOMP and FFT-A highly scalable 2D decomposition library and FFT. *Cray User Group Proceedings, Scotland*, pages 1–13, 2010.

[20] J. Kim, P. Moin, and R. Moser. Turbulence statistics in fully developed channel flow at low reynolds number. *Journal of Fluid Mechanics*, 177, 1987.

[21] S. Leonardi and P. Orlandi. A numerical method for turbulent flows over complex geometries. *ER COFTAC bulletin*, 62:41 – 46, 2004.

[22] M. Mail, A. Klien, H. Bleckmann, A. Schmitz, T. Scherer, P. T. Ruhr, G. Lorvic, R. Frohlingsdorf, S. N. Gorb, and W. Barthlott. A new bioinspired method for pressure and flow sensing based on the underwater air-retaining surface of the backswimmer notoncena. *Beilstein Journal of nano-technology*, 9:3039 – 3047, 2018.

[23] Johann Nikuradse. *Strömungsgesetze in rauhen Rohren.* VDI-Verlag, 1933.

[24] D. M. Bushnell and Moore K. J. Drag reduction in nature. *Annual Reviews Fluid Mechanics*, 23, 1991.

[25] M. Seddighi, S. He, D. Pokrajac, T. O'. Donoghue, and A. E. Vardy. Turbulence in a transient channel flow with a wall of pyramind roughness. *Journal of Fluid Mechanics*, 781:226 – 260, 2015.

[26] S.H. Park and I. Lee. Optimization of drag reduction effect on air lubrication for a tanker model. *International Journal of Naval Architecture and Ocean Engineering*, 2017.

[27] H.A. Abdulbar, H. D. Mahammed, and Hassan Z. B. Y. Bio-inspired passive drag reduction techniques: A review. *ChemBioEng Reviews*, 3:185 – 203, 2015.

[28] J. Davenport, R. N. Huges, M. Shorten, and P. S. Larsen. Drag reduction by air release promotes fast ascent in jumping emperor penguins - a novel hypothesis. *Marine Ecology Progress Series*, 430:171 – 182, 2011.

[29] D. Neumann and A. Kureck. Composite structure of silken threads and a proteinaceous hydrogel which form the diving bell wall of the water spider agyroneta aquatica. *Springer Plus*, 2(1):223, 2013.

[30] H. Hertel. Structure form and movement. *Newyork: Reinhold*, 1963.

[31] R. N. Meroney. Charactiristics of wind an turbulence in and above model forest. *Journal of Applied Meteorology*, 7(5):780–788, 1968.

[32] B. G. Newman, S. B. Savage, and D. Schouella. Model tests on a wing section of the aeschna dragonfly. *In scale effects animal locomotion*, 1977.

[33] J. Magnuson. Locomotion by scombird fishes: hydrodynamics, morphology and behaviour. *Fish Physiol*, 7:239 – 310, 1978.

[34] V. Stenzel, Y. Wilke, and W. Hage. Drag reducing paints for the reduction of fuel consumption in aviation and shipping. *Progress in organic coatings*, 70:224 – 229, 2011.

[35] J. Sun and B. Bhushan. Nanomanufacturing of bioinspired surfaces. *Tribology International*, 129:67 – 74, 2019.

[36] K. B. Golovin, J. W. Gose, M. Perlin, S. L. Ceccio, and A. Tuteja. Bioinspired surfaces for turbulent drag reduction. *Phil.Trans.R.Soc.A*, 374:20160189, 2016.

[37] J. P. Rothstein. Slip of superhydrophobic surfaces. *Annual Reviews Fluid Mechanics*, 42:89 – 109, 2010.

[38] M. B. Martell, J. P. Rothstein, and J. B. Perot. An analysis of superhydrophobic turbulent drag reduction mechanisms using direct numerical simulation. *Physics of Fluids*, 22.6, 2010.

[39] S. Watanabe, H. Mamori, and K. Fukagata. Drag reducing performance of obliquely aligned superhydrophobic surface in turbulent channel flow. *The Japan Society of Fluid Mechanics*, 49,025501, 2017.

[40] K. Alame and K. Mahesh. Wall-bounded flow over realistically rough superhydrophobic surface. *Journal of Fluid Mechanics*, 873:977 – 1019, 2019.

[41] D. Goldstein, R. Hander, and L. Sirovich. Direct numerical simulation of turbulent flow over a modelled riblet covered surface. *Journal of Fluid Mechanics*, 302:333 – 376, 1995.

[42] E. Lepore, M. Giorcelli, C. Saggese, A. Tagliaferro, and N. Pungo. Mimicking water striders' legs superhydrophobicity and buoyancy with cabbage leaves and nanotube carpets. *J. Mater. Res*, 28:976 – 983, 2013.

[43] S. Srinvasan, S. S. Chhatre, J. O. Guardado, K. C. Park, A. R. Parker M. F. Rubner, and G. H. Cohen. Quantification of feather structure, wettability and resistance to liquid penetration. *J. R. Soc. Interface*, 11:20140287, 2014.

[44] H. Chen, F. Rao, X. Shang, D. Zhang, and I. Hagiwara. Biomimetic drag reduction study on herringbone riblets of bird feather. *Journal of physics: Conference Series*, 10:341 – 349, 2013.

[45] H. Chen, F. Rao, X. Shang, D. Zhang, and I. Hagiwara. Flow over bio-inspired 3D herringbone wall riblets. *Experiments in fluids*, 55:1698, 2014.

[46] M. D. Ibrahim, S. N. Amran, Y. S. Yunos, M. R. Rahman, M. Z. Mohtar, I. K. Wong, and A. Zulkharnian. The study of drag reduction on ships inspired by simplified shark skin imitation. *Applied Bionics and Biomechanics*, 10.1155, 2018.

[47] P. Orlandi, S. Leonardi, and R. Antonia. Turbulent channel flow with either transverse or longitudinal roughness elements on one wall. *Journal of Fluid Mechanics*, 561:279 – 305, 2006.

[48] S. Leonardi, P. Orlandi, L. Djenidi, and R. A. Antonia. Structure of turbulent channel flow with square bars on one wall. *International journal of heat and fluid flow*, 3:384 – 392, 2004.

[49] D. Modesti, S. Endrikat, R. G. Mayoral, N. Hutchins, and D. Chung. Contribution of dispersive stress to skin friction drag in turbulent flow over riblets. *11th International symposium of turbulence and shear stress phenomena (TSFP11), Southampton, UK*, 2019.

[50] S. A. Orzag and P. A. Patterson. Numerical simulation of three dimensional homogenous isotropic turbulence. *Physical Review Letters*, 82(2), 1972.

[51] F. Alcantara-Avila, S. Hoyas, and M. J. Perez-Quiles. DNS of thermal channel flow up to $Re_\tau = 2000$ for medium to low prandtl numbers. *International journal of heat and mass transfer*, 127, 2018.

[52] Y. Yamamoto and Y. Tsuji. Numerical evidence of logarithmic regions in channel flow at $Re_\tau = 8000$. *Physical Review Fluids*, 3(1), 2018.

[53] J. W. Deardorff. Numerical study of three-dimensional turbulent channel flow at large reynolds numbers. *Journal of Fluid Mechanics*, 41(pt 2), 1970.

[54] V. Spalart. Strategies for turbulence modelling and simulations. *International Journal of heat and fluid flow*, 21:252 – 263, 2000.

[55] Kajishma. www-fluid.mech.eng.osaka-u.ac.jp/ kajishma. 1997.

[56] A. Mathur. Study of accelerating and decelerating turbulent flows in a channel. *PhD thesis*, 2016.

[57] S. He, K. He, and M. Seddighi. Laminarisation of flow at low reynolds number due to streamwise body force. *Journal of Fluid mechanics*, 809:31 – 71, 2016.

[58] J. D. Anderson. Computational fluids dynamics the basics with applications. *Mcgraw - Hill International*, 1995.

[59] P. Moin and K. Mahesh. Direct numerical simulations: A tool in turbulence research. *Annual Review of Fluid Mechanics*, 30:78:539 – 578, 1998.

[60] D. A. Mallon et al. Performance evaluation of MPI, UPC and OpenMP on multicore architectures. *European Parallel Virtual Machine/Message Passing Interface Users' Group Meeting. Springer Berlin Heidelberg.*, 2009.

[61] J. Hoeflinger, P. Alavilli, T. Jackson, and b. Kuhn. Producing scalable performance with openmp experiments with two cfd applications,. *Parallel Computing*, 27:391–413, 2000.

[62] R. Rabenseifner. Hybrid parallel programming on HPC platforms. *Fifth European Workshop on OMP, EWOMP, Germany*, pages 22 – 26, 2003.

[63] F. Bassi, A. Colombo, A. Crivellini, and M. Franciolini. Hybrid OpenMP/MPI parallelization of high order discontinuous glaerkin CFD/CDA solver. *VII European Congress on Computational Methods in Applied Sciences, Greece*, pages 1 – 21, 2016.

[64] Numerical Algorithms Group. Fortran modernization course. *University of Southampton*, 2017.

[65] H. Kreplin and H. Eckelmann. Behaviour of the three fluctuating velocity componenets in the wall region of a turbulent channel flow. *Physics of Fluids*, 22:12 – 33, 1979.

[66] T. J. Hanratty, L. G. Chorn, and D. T. Hatziavramidis. Turbulent fluctuations in the viscous wall region for newtonian and drag reducing fluids. *Physics of Fluids*, 20:1 – 12, 1977.

[67] W. W. Willmarth and S. S. Lu. Structure of the reynolds shear stress near the wall. *Journal of Fluid Mechanics*, 55:65, 1972.

[68] E. A. Faldun, R. Verzicco, P. Orlandi, and J. MOHD-YUSOF. Combined immersed boundary finite difference methods for three dimensional complex flow simulations. *Journal of computational physics*, 161 (1), 2000.

[69] W. Barthlott, M. Mail, and C. Neinhuis. Superhydrophobic hierarchically structured surfaces in biology: evolution structural principles and biomimetic applications. *Phil.Trans.R.Soc.A*, 374:20160191, 2016.

[70] D. Chung, M. MacDonald, L. Chan, N. Hutchins, and A. Ooi. A fast and direct method for characterizing hydraulic roughness. *TSFP-9*, pages 327 – 352, 2005.

[71] W.P. Breugem, B. J. BOERSMA, and R. E. Uittenbogaard. The influence of wall permeability on turbulent channel flow. *Journal of Fluid Mechanics*, 562, 2006.

[72] H. S. Shafi and R. A. Antonia. Small scale characteristics of a turbulent boundary layer over a rough wall. *Journal of Fluid Mechanics*, 342:263 – 293, 1997.

[73] J. M.Wallace. Quadrant analysis in turbulence research: History and evolution. *Annual Reviews*, 48, 2016.

[74] P. A. Krogstad, H. I. Anderson, O. M. Bakken, and A. Ashrafian. An experimental and numerical study of channel flow with rough walls. *Journal of fluid mechanics*, 530:327 – 352, 2005.

List of Publications

M.Seddighi, D.R. Allanson and **K.Takrouri**, "Study on Use of a Combination of Ipython Notebook and an Industry-Standard Package in Educating a Computationally Related Course", Computer Applications in Engineering Education, 2020

K.Takrouri and M.Seddighi, "A DNS Study on Drag/Increase of a Backswimmer Textured Surface in Channel Flows", UK Turbulence Consortium (UKTC) Annual Meeting, September 2019.

K.Takrouri and M.Seddighi, "Turbulent Drag Reduction Using Backswimmer Textured Surfaces ", European Drag Reduction and Flow Control meeting, Bad Herrenalb, Germany March 2019.

K.Takrouri and M.Seddighi, "Turbulent Drag Reduction Using Backswimmer Textured Surfaces for Channel Flow", UK Turbulence Consortium (UKTC) Annual Meeting, September 2018.

M. Seddighi and **K.Takrouri**, "Study of Drag Reduction Using Unsteady Pulsating Flow", UK Turbulence Consortium (UKTC) Annual Meeting, September 2017.

Appendix A: F90 Backswimmer Implementation Source Code.

```
SUBROUTINE GEOTR2BS(X,Z,Y1,Y2) ! Wall Normal Direction

 use mpi_info
 use mesh_info
 use init_info
 use ROUGHNESS_init
IMPLICIT NONE

REAL(WP),INTENT(INOUT) :: y1,y2
REAL(WP),INTENT(IN) :: X,Z
INTEGER(4) :: NX1,NX3,NN1,NN3
REAL(WP)      :: YLIMIT2
REAL(WP)      :: XB1,ZB1,x3_clamp,XB2,ZB2,Xmid1,Xmid2,XL,XU,ymid1
REAL(WP)      :: YCREST1, YCREST2
REAL(WP)      :: X1_CLAMP, Z1_CLAMP
REAL(WP)      :: CX1,CX2,CX_MID,X_MID1,X_MID2
REAL(WP)      :: DXC_Upper,DXC_Lower,DRC_Upper,DRC_Lower
REAL(WP)      :: C0U, C1U, C2U, C3U, C4U, C5U
REAL(WP)      :: C6U, C7U, C8U, C9U, C10U
REAL(WP)      :: C0L, C1L, C2L, C3L, C4L, C5L
REAL(WP)      :: C6L, C7L, C8L, C9L, C10L
```

```
ycrest1 = -1.D0
ycrest2 = 1.D0
Y1 = 0.D0
Y2 = 0.D0
nn1 = x / clambd1
nn3 = z / clambd3
xb1 = nn1 * clambd1
zb1 = nn3 * clambd3
x1_clamp = x - xb1
x3_clamp = z - zb1
xb2 = bh1 + nn1 * clambd1
zb2 = bh3 + nn3 * clambd3
Xmid1 = 0.07D0 * BH1
ymid1 = 0.8D0 * BHC
Xmid2 = 1.D0 * BH1

C10L = 93.48759027D0
C9L = -382.539018D0
C8L = 511.0157526D0
C7L = 0.D0
C6L = -743.1775956D0
C5L = 924.4431969D0
C4L = -566.3213164D0
C3L = 200.8254252D0
C2L = -43.64128849D0
C1L = 6.896833888D0
C0L = 0.01048772D0

C10U = 0.D0
C9U = 0.D0
C8U = 0.D0
C7U = 0.D0
C6U = -26.05983336D0
```

```
C5U = 87.61258073D0
C4U = −115.65064929D0
C3U = 76.43966534D0
C2U = −27.56126837D0
C1U = 6.199489684D0
C0U = 0.007735913D0

If(z.GE.zb1.and.z.LT.zb2) THEN
IF(x.GE.xb1.and.x.LT.xb2) THEN
IF(x1_clamp.le.Xmid1) then
DRC_Lower = 0.D0
XU = x1_clamp / BH1
DRC_Upper = C6U * XU**6 + C5U * XU**5 + C4U * XU**4 + C3U * XU**3 &
+ C2U * XU**2 + C1U * XU     + C0U
ELSEIF(x1_clamp.gT.Xmid1.and.x1_clamp.le.Xmid2) THEN
XL =    (x1_clamp−xmid1) / (xmid2 − xmid1)
XU =    x1_clamp / BH1
DRC_Lower = C10L * XL**10 + C9L * XL**9 + C8L * XL**8 + &
C7L * XL**7  + C6L * XL**6 + C5L * XL**5 +  &
C4L * XL**4  + C3L * XL**3 + C2L * XL**2 +  &
C1L * XL + C0L
DRC_Upper = C6U * XU**6 + C5U * XU**5 + C4U * XU**4 + C3U * XU**3 &
+ C2U * XU**2 + C1U * XU     + C0U
ENDIF
y1 = YND_0(1) + DRC_Lower * ymid1
y2 = YND_0(1) + DRC_upper * bhc
ELSE
y1=YND_0(1)
y2=y1
endif
ELSE
y1=YND_0(1)
y2=y1
```

```
ENDIF
RETURN
END



SUBROUTINE GEOTR3BS(Z1,Z2,Y,X,Z) ! Spanwise direction
use mpi_info
use mesh_info
use init_info
IMPLICIT NONE
REAL(WP),INTENT(INOUT) :: Z1,Z2
REAL(WP),INTENT(IN) :: X,Y,Z
INTEGER(4) :: NX1,NX3,NN1,NN3
REAL(WP)   :: YLIMIT2,Y1,Y2
REAL(WP)   :: XB1,ZB1,x3_clamp,XB2,ZB2,Xmid1,Xmid2,XL,XU,YMID1,YL,YU,y
REAL(WP)   :: X1_CLAMP, Z1_CLAMP,X2_CLAMP
REAL(WP)   :: CX1,CX2,CX_MID,X_MID1,X_MID22,X_MID2
REAL(WP)   :: DXC_Upper,DXC_Lower,DRC_Upper,DRC_Lower
REAL(WP)   :: C0U, C1U, C2U, C3U, C4U, C5U
REAL(WP)   :: C6U, C7U, C8U, C9U, C10U
REAL(WP)   :: C0L, C1L, C2L, C3L, C4L, C5L
REAL(WP)   :: C6L, C7L, C8L, C9L, C10L

ycrest1 = -1.D0
ycrest2 = 1.D0
Y1 = 0.D0
Y2 = 0.D0
nn1 = x / clambd1
nn3 = z / clambd3
xb1 = nn1 * clambd1
zb1 = nn3 * clambd3
```

```
x1_clamp = x - xb1
x3_clamp = z - zb1
xb2 = bh1 + nn1 * clambd1
zb2 = bh3 + nn3 * clambd3
Xmid1 = 0.07D0 * BH1
ymid1 = 0.8D0 * BHC
Xmid2 = 1.D0 * BH1

C10L = 93.48759027D0
C9L = -382.539018D0
C8L = 511.0157526D0
C7L = 0.D0
C6L = -743.1775956D0
C5L = 924.4431969D0
C4L = -566.3213164D0
C3L = 200.8254252D0
C2L = -43.64128849D0
C1L = 6.896833888D0
C0L = 0.01048772D0

C10U = 0.D0
C9U = 0.D0
C8U = 0.D0
C7U = 0.D0
C6U = -26.05983336D0
C5U = 87.61258073D0
C4U = -115.65064929D0
C3U = 76.43966534D0
C2U = -27.56126837D0
C1U = 6.199489684D0
C0U = 0.007735913D0
```

```
IF(x.GE.xb1.and.x.LE.xb2) THEN
IF(x1_clamp.le.Xmid1) THEN
DRC_Lower = 0.D0
XU = x1_clamp / BH1
DRC_Upper = C6U * XU**6 + C5U * XU**5 + C4U * XU**4 + C3U * XU**3 &
+ C2U * XU**2 + C1U * XU + C0U
ELSEIF(x1_clamp.GT.Xmid1.and.x1_clamp.LE.Xmid2) THEN
XL =    (x1_clamp-xmid1) / (xmid2 - xmid1)
XU =    x1_clamp / BH1
DRC_Lower = C10L * XL**10 + C9L * XL**9 + C8L * XL**8 + &
C7L * XL**7  + C6L * XL**6 + C5L * XL**5 + &
C4L * XL**4  + C3L * XL**3 + C2L * XL**2 + &
C1L * XL + C0L

DRC_Upper = C6U * XU**6 + C5U * XU**5 + C4U * XU**4 + C3U * XU**3 &
+ C2U * XU**2 + C1U * XU     + C0U
ENDIF

y1 = YND_0(1) + DRC_Lower * ymid1
y2 = YND_0(1) + DRC_upper * bhc

IF(Y.GE.Y1.AND.Y.LE.Y2) THEN
Z1=ZB1
Z2=ZB2
ELSE
Z1=1000.D0
Z2=1000.D0
ENDIF

ELSE
Z1=1000.D0
Z2=1000.D0
ENDIF
```

```
RETURN
END


SUBROUTINE GEOTR1BS(x1,x2,y,z,x) ! Streamwise Direction
use mpi_info
use mesh_info
use init_info
use ROUGHNESS_init
IMPLICIT NONE
REAL(WP),INTENT(INOUT) :: X1,X2
REAL(WP),INTENT(IN) :: Y,Z,X
INTEGER(4) :: NX1,NX3,NN1,NN3
REAL(WP)   :: YLIMIT2,Y1,Y2
REAL(WP)   :: XB1,ZB1,x3_clamp,XB2,ZB2,Xmid1,Xmid2,XL,YMID1,YL,YU,ycre
REAL(WP)   :: YCREST,Y_START
REAL(WP)   :: X1_CLAMP, Z1_CLAMP,Y1_CLAMP
REAL(WP)   :: CX1,CX2,CX_MID,ZB_MID
REAL(WP)   :: X_MID1,X_MID2,Y_MID1,Y_MID2
REAL(WP)   :: DYC_Upper,DYC_Lower,DRC_Upper,DRC_Lower
REAL(WP)   :: C0U, C1U, C2U, C3U, C4U, C5U
REAL(WP)   :: C6U, C7U, C8U, C9U, C10U
REAL(WP)   :: C0L, C1L, C2L, C3L, C4L, C5L
REAL(WP)   :: C6L, C7L, C8L, C9L, C10L

ycrest1 = −1.D0
ycrest2 = 1.D0
Y1 = 0.D0
Y2 = 0.D0
nn1 = x / clambd1
nn3 = z / clambd3
xb1 = nn1 ∗ clambd1
zb1 = nn3 ∗ clambd3
```

```
x1_clamp = x - xb1
x3_clamp = z - zb1
xb2 = bh1 + nn1 * clambd1
zb2 = bh3 + nn3 * clambd3
Xmid1 = 0.07D0 * BH1
ymid1 = 0.8D0 * BHC
Xmid2 = 1.D0 * BH1

C10L = 785.0297462D0
C9L = -2006.78245D0
C8L = 0.D0
C7L = 5331.124547D0
C6L = -7900.720636D0
C5L = 5495.140674D0
C4L = -2101.996643D0
C3L = 444.8357152D0
C2L = -47.96767554D0
C1L = 2.319440257D0
C0L = -0.025094084D0

C10U = 0.D0
C9U = 0.D0
C8U = 0.D0
C7U = 0.D0
C6U = 38.72248959D0
C5U = -104.6252568D0
C4U = 106.4720246D0
C3U = -49.78145072D0
C2U = 10.91548084D0
C1U = -0.748247651D0
C0U = 0.013447435D0

If(z.GE.zb1.and.z.LE.zb2) THEN
```

```
IF(y.EQ.YND_0(1)) THEN
x1 = xb1
x2 = xb1 + Xmid1

ELSEif(y.GT.YND_0(1).and.y.LE.ycrest1) THEN
IF(y.LT.YND_0(1)+Ymid1) THEN
YL =    ( y - YND_0(1)  ) / YMID1
YU =    ( Y - YND_0(1)  ) / BHC
DRC_Lower = C10L * YL**10 + C9L * YL**9 + C8L * YL**8 + &
C7L * YL**7  + C6L * YL**6 + C5L * YL**5 + &
C4L * YL**4  + C3L * YL**3 + C2L * YL**2 + &
C1L * YL + C0L

DRC_Upper = C6U * YU**6 + C5U * YU**5 + C4U * YU**4 + C3U * YU**3
&
+ C2U * YU**2 + C1U * YU + C0U

ELSEIF(y.GE.YND_0(1)+Ymid1) THEN
DRC_Lower = 1.D0 !(Xmid2 - Xmid1) / BH1
YU =    ( Y - YND_0(1)  ) / BHC
DRC_Upper = C6U * YU**6 + C5U * YU**5 + C4U * YU**4 + C3U * YU**3 &
+ C2U * YU**2 + C1U * YU + C0U
ENDIF
x2 = xb1 + DRC_Lower  * (XMID2 - XMID1) + XMID1      !bh1 + Xmid1
x1 = xb1 + DRC_upper * bh1
ELSE
x1=1000.D0
x2=1000.D0
ENDIF
ELSE
x1=1000.D0
x2=1000.D0
ENDIF
```

```
RETURN
END
```